Search for Randall-Sundrum Gravitons in 1.2 fb^{-1} of Run II High Mass Diphoton Data at CDF

Sara-Madge Wynne

April 2007

University of Liverpool

Department of Physics

Thesis submitted in accordance with the requirements of the University of Liverpool for the degree of Doctor of Philosophy

Abstract

A search for Randall-Sundrum gravitons decaying to two photons is performed using 1.2 fb^{-1} of data from $p\bar{p}$ collisions at $\sqrt{s} = 1.96$ TeV, recorded by the Collider Detector at Fermilab between February 2002 and February 2006. The diphoton mass spectrum is found to be in agreement with Standard Model expectations, with no significant excess of events being observed. Upper limits are set on the experimental cross-section times branching ratio ($\sigma \cdot BR(G \rightarrow \gamma\gamma)$) at the 95% confidence level, for the Randall-Sundrum model, as a function of graviton mass. The exclusion region in the parameter space of graviton mass and coupling parameter $k/\overline{M}_{Pl}$ is then derived, with lower mass limits of 230 GeV/c^2 and 850 GeV/c^2 obtained for $k/\overline{M}_{Pl} = 0.01$ and 0.1, respectively.

This analysis was blessed by the CDF collaboration on 20th July 2006.

Acknowledgments

I am extremely grateful to Ray Culbertson, Beate Heinemann and Tracey Berry for all their guidance and advice, as well as their patience and understanding. I am especially grateful to Sam Harper for all his help, endless patience and moral support. Many thanks also to Mike Houlden for all his invaluable feedback while trying to put this thesis together, and for making everything run as smoothly as possible. Many thanks to Barry King for answering my endless questions and for such a great introduction to Chicago. Thanks also to the Photon, VEP and Exotics groups at CDF for all their help and suggestions, and to the whole CDF group at Liverpool. I would especially like to acknowledge Paul Booth, without whose inspiration and leadership the group would not have been possible.

Special thanks go to my parents, Michael and Katy, for their love and support, and to some great friends who have helped me through the tougher times.

I also thank all the members of Fermilab, including the technical staff who have built, maintained and run both the Tevatron and CDF detector, and gratefully acknowledge funding from the Particle Physics and Astronomy Research Council, without whom this thesis would not have been possible.

Author's Contribution

In October 2004, whilst undertaking the diphoton analysis at CDF, I was also involved in the replacement of the Central Preshower (CPR) and Central Crack (CCR) detectors, with an integrated detector based on scintillator (CPR2). The CPR plays an important role in resolving single photons from meson decays, which cannot be achieved by the shower maximum detector alone, due to the small angular separation. The CPR uses photon conversion rates, which are energy independent, and can be used at any energy range. It is also important in improving the jet resolution, through incorporating tracking information in the jet reconstruction algorithm. The CPR2 scintillator counters are read out by wavelength shifting fibers and have better segmentation, which improve jet energy resolution by correcting for energy loss in the dead material in front of it and adding its information in jet algorithms incorporating charged tracking. The scintillator also has a better signal response resolution compared to the old gas detectors, which is of crucial importance to electron and photon identification and energy resolution improvements.
From January 2006 to April 2006, I was involved in CDF operations, responsible for data taking and data quality.
Apart from where stated otherwise, all results presented in this analysis are the work of the author.

Presentations

Search for Randall Sundrum Gravitons in High MassDiphotons at CDF. Presented at the University of Liverpool Annual High Energy Physics Meeting, December 2005.
Search for Extra Dimensions. Presented at the Institute of Physics Particle Physics 2006, Warwick, April 2006.

Extra Dimensions at CDF. Poster presented at the the Hadron Collider Physics Symposium, Duke University, Durham, North Carolina, May 2006.

Contents

1 Introduction **1**

1.1 The Standard Model 3

1.1.1 The Fermions 3

1.1.2 The Gauge Bosons 4

1.1.3 Quantum Electrodynamics (QED) 5

1.1.4 Quantum Chromodynamics (QCD) 9

1.1.5 Parton Distribution Functions 11

1.2 Limitations of the Standard Model 12

1.2.1 The Hierarchy Problem 13

1.2.2 Extra Dimensions 15

1.2.3 Collider Phenomenology 18

2 The Fermilab Accelerator and CDF Detector **25**

2.1 The Tevatron Accelerator Chain 25

2.1.1 Proton Production 26

2.1.2 The Main Injector 27

2.1.3 The Tevatron 28

2.1.4 Performance Parameters 29

2.2 Collider Detector at Fermilab 30

2.2.1 Geometrical Coordinate System 32

2.2.2 Tracking System 33

2.2.3 Calorimeters 41
2.2.4 Muon System 45
2.2.5 Luminosity 46
2.2.6 Trigger Systems and Data Acquisition 47
2.2.7 Data Processing 49
2.3 Detector Simulation 50

3 Data Sample and Event Selection **52**
3.1 Triggers 52
3.1.1 Photon Trigger 53
3.1.2 Electron Trigger 55
3.2 Event Reconstruction 57
3.2.1 Calorimeter Clustering 58
3.2.2 Event Vertex Reconstruction 61
3.2.3 Detector Calibration 62
3.3 Additional Energy Corrections 64
3.4 Event Selection 66
3.4.1 Global Event Selection 67
3.4.2 Photon Identification and Event Selection 69
3.4.3 Electron Identification and Event Selection 76

4 Signal Acceptance **80**
4.1 Acceptance for $G \to \gamma\gamma$ events 81
4.2 Systematic Uncertainties 84
4.2.1 Energy Scale 84
4.2.2 Parton Distribution Functions 86
4.2.3 Initial and Final State Radiation 88

5 Efficiency **91**
5.1 Single Photon Identification Efficiency 92

5.1.1 χ^2 Efficiency . . . 92
5.2 $G \to \gamma\gamma$ Efficiency . . . 98
5.2.1 $G \to \gamma\gamma$ Correction Factors . . . 98
5.3 Trigger Efficiency . . . 104
5.4 Scaled Single Photon Efficiencies . . . 105
5.5 Total Scaled $G \to \gamma\gamma$ Efficiencies . . . 107
5.6 Low Energy Behaviour Data/ Monte Carlo Comparison . . . 107
5.7 Z Vertex Efficiency . . . 110
5.8 Photon Conversions . . . 113

6 *'A Priori'* Display Background 114
6.1 Standard Model Background . . . 115
6.2 QCD Background . . . 118
6.3 Background from e^+e^- Production . . . 123
6.4 Background Systematic Uncertainties . . . 125
6.5 Total *'A Priori'* Display Background . . . 128

7 RS Graviton Cross-Section Limits 134
7.1 Binned Likelihood Method . . . 134
7.1.1 Likelihood Without Systematic Errors . . . 135
7.1.2 Likelihood Incorporating Systematic Errors . . . 137
7.2 Background . . . 139
7.3 Theoretical Cross-Section . . . 143
7.3.1 K-Factor . . . 143
7.4 Limits . . . 143
7.4.1 Cross-Section Limits without Systematic Errors . . . 144
7.4.2 Cross-Section Limits with Systematic Errors . . . 144
7.4.3 Lower Mass Limits and 2-Dimensional Exclusion Domain 146

8 Summary 150

A Plug Electron Rejection and Plug Tracking Efficiencies 153

A.1 Electron Rejection Factors 153

A.2 Phoenix and Silicon Standalone Tracking Efficiencies 155

B Efficiency Calculation for Central-Central Lepton Events 157

C Combined Diphoton and Dielectron Limits on Randall-Sundrum Graviton Production 159

List of Figures

1.1 Radiative corrections to the Higgs boson mass from gauge bosons, the Higgs boson and fermion loops. 14

1.2 Graviton branching fractions for the Randall-Sundrum model [22]. 18

1.3 Feynman diagrams for virtual graviton exchange in the diphoton channel 19

1.4 A 700 GeV/c^2 KK graviton, decaying to the dilepton channel, for $k/\overline{M}_{Pl}$ = 1.0, 0.5, 0.1, 0.05, and 0.01, from top to bottom. Below, a 1500 GeV/c^2 KK graviton, and its subsequent tower states [24]. 20

1.5 Comparison of Z boson peaks and widths for central-central and central-plug events. 22

1.6 Excluded RS graviton mass region, as a function of $k/\overline{M}_{Pl}$. The dotted line shows the experimental limit using 246 pb^{-1} and 275 pb^{-1} of data, for the dimuon and diEM channels respectively, using the D0 detector. The area below the dashed line is excluded by the precision electroweak data and the dark shaded area in the right hand corner corresponds to $\Lambda_\pi > 10$ TeV [26]. . 23

1.7 Excluded RS graviton mass region, as a function of $k/\overline{M}_{Pl}$, for the combined dilepton and diphoton channels at CDF using 200 pb^{-1} and 345 pb^{-1} of data, respectively [27]. 24

2.1 Schematic of the Fermilab accelerator complex. 26

2.2 Longitudinal view of half of the CDF Run II detector. 31
2.3 Current total integrated luminosity recorded at CDF for Run II. 32
2.4 CDF coordinate system. 33
2.5 Longitudinal view of the CDF tracking system, representing one quadrant. 34
2.6 $r-\phi$ and $r-z$ perspectives of the silicon detector, showing all subcomponents. The port cards, located around the periphery of the barrel ends, decode the data and convert it from electrical to optical signals via optical interface modules. 35
2.7 Endview of innermost three layers showing L00 along with first two layers of the SVX II region. 36
2.8 On the left, view of the three barrels of the SVX silicon detector. On the right, end view of one barrel showing the 12 wedges with the 5 layers. 37
2.9 On the left, the $r-z$ view of the silicon detector layout and on the right a schematic view of the ISL, both showing the additional silicon layer for matching SVX and COT tracks and two layers providing tracking coverage out to $|\eta| < 2$. 37
2.10 Schematic of the four axial (even) and four stereo (odd) superlayers. 39
2.11 Schematic of a wedge of the central calorimeter, illustrating the towers pointing back to the interaction point. 42
2.12 Schematic of one quadrant of the plug calorimeter. 45
2.13 Muon system coverage in η and ϕ. 46
2.14 Dataflow diagram of the CDF three-level trigger system. 50

3.1 $Z \rightarrow ee$ invariant mass distribution, plotted in bins of 1 GeV/c^2, for central-central and central-plug dielectron candidates, with energy scale factors applied to data and Monte Carlo. The data are fitted to a Gaussian distribution in the range 86 GeV/c^2 < M_{ee} < 98 GeV/c^2. 67
3.2 Invariant mass distribution for central-central (top) and central-plug (bottom) events after all selection criteria are applied, with bin widths comparable to the mass resolution. 74
3.3 Invariant mass distribution after all selection criteria are applied, for central and plug channels combined, with bin widths comparable to the mass resolution. 75

4.1 Signal acceptance for the $G \rightarrow \gamma\gamma$ decay channel, measured using simulation, showing statistical errors only. 83
4.2 Angular distributions in graviton production and decay. Line (c) shows $gg \rightarrow G \rightarrow \gamma\gamma$ and line (a) $q\bar{q} \rightarrow G \rightarrow \gamma\gamma$. 84
4.3 Difference between the mass spectra in $Z \rightarrow ee$ data and Monte Carlo, in the range 82 GeV/c^2 < M_{ee} < 98 GeV/c^2, for the differing subdetector regions, for CC and CP events. 85

5.1 (N-1) efficiencies for central photon identification selection cuts as a function of E_T, for $E_T > 50$ GeV. 93
5.2 (N-1) efficiencies for plug photon identification selection cuts as a function of E_T, for $E_T > 50$ GeV. 94
5.3 Central χ^2 (N-1) efficiency as a function of E_T. 95
5.4 (N-1) efficiencies for $\chi^2 < 20$ and $\chi^2 < 50$ using jet data samples. 97
5.5 Central χ^2 efficiency for the looser $\chi^2 < 50$ for $E_T > 50$ GeV. . . 97
5.6 DIPHOTON_12 and DIPHOTON_18 trigger efficiencies, given as a function of mass. 106

5.7 Scaled efficiency for a single photon to pass the selection criteria, shown for central photons on the left plot and plug photons on the right. 107
5.8 Total scaled efficiency (acceptance * efficiency) for the $G \to \gamma\gamma$ decay channel, measured using simulation, showing statistical errors only. 108
5.9 (N-1) efficiencies for central photon identification selection cuts as a function of E_T. 111
5.10 (N-1) efficiencies for plug photon identification selection cuts as a function of E_T. 112

6.1 The leading order contribution to diphoton production, given by the Born level process $q\bar{q} \to \gamma\gamma$. 115
6.2 NLO calculations contribute $\mathcal{O}(\alpha_s)$ corrections, arising from the subprocesses $q\bar{q} \to \gamma\gamma g$, gq (or $\bar{q}$) $\to \gamma\gamma q$ (or $\bar{q}$) and corresponding virtual corrections. 115
6.3 The 'Bremsstrahlung contribution', originating from the collinear fragmentation of a hard parton. 116
6.4 Examples of the $\mathcal{O}(\alpha_s)$ corrections to the gq (or g$\bar{q}$) initiated contributions, involving one photon from fragmentation, which are required to give a consistent treatment of NLO diphoton production. 116
6.5 The corrections to the gq (or g$\bar{q}$) initiated contributions which yield, in their turn, the leading order contribution of the double fragmentation mechanism. 117
6.6 The NLO contributions from the double fragmentation contribution, where both photons result from the collinear fragmentation of a hard parton, which must be included for a full NLO calculation. 117

6.7 Total mass-dependent diphoton identification efficiency, measured in *PYTHIA*. A linear fit is shown (dark line), with its uncertainty (pale lines). 119
6.8 Invariant mass distribution for Standard Model diphoton production. Note that the central-plug distribution is taken from the sum of the three η regions. 120
6.9 Normalized invariant mass distribution for Standard Model diphoton production for the the three central-plug η regions. 121
6.10 Invariant mass distribution of sideband events. The central-plug distribution is taken from the sum of the three η channels. . . . 124
6.11 Invariant mass distribution of sideband events for the three central-plug η channels. 125
6.12 Invariant mass distribution for Standard Model diphoton events predicted by *DIPHOX* using $M = M_f = Q/2$ and $M = M_f = Q * 2$. 126
6.13 The variations of the central-central sideband mass distributions as compared to the standard sideband distribution (denoted by the thick black line). 129
6.14 The variations of the central-plug sideband mass distributions as compared to the standard sideband distribution (denoted by the thick black line). 130
6.15 The ratio of each sideband variation to the standard sideband as a function of diphoton mass. Due to low statistics at above100 GeV/c^2, only events below this invariant mass are used to obtain the systematic uncertainty, which is taken as 20% as the ratio of the sideband variations predominantly lie between ± 0.2. 131

6.16 The central-central and central-plug signal region mass distributions with the *a priori* background overlayed. This background is not used in setting limits. The blue line is the *DIPHOX* true diphoton events, and the red line is the fake photons as predicted from the the sidebands. 132

6.17 The low mass central-central and central-plug signal region mass distributions with the *a priori* background overlayed. This background is not used in setting limits. The blue line is the *DIPHOX* true diphoton events, and the red line is the fake photons as predicted from the sidebands. 133

7.1 The central-central and central-plug signal region mass distributions with the background fit overlayed. 140

7.2 The central-central and central-plug signal region mass distributions with the integral of the background from the limit fit overlayed. 141

7.3 The central-central and central-plug invariant mass distributions, showing the background fit with 5 signal events inserted at 600 GeV/c^2. The excess remains clearly visible above the background. 142

7.4 The 95% CL upper limit for $\sigma \cdot BR(G \rightarrow \gamma\gamma)$, as a function of graviton mass, for data in the central-central channel, shown on the left, and the central-plug, shown on the right, together with the expected limits from the pseudo-experiments. No systematic errors are included. 144

7.5 The 95% CL upper limit for $\sigma \cdot BR(G \rightarrow \gamma\gamma)$, as a function of graviton mass, for data in the central-central and central-plug channels combined, together with the expected limits from the pseudo-experiments. No systematic errors are included. 145

7.6 The 95% CL upper limit for $\sigma \cdot BR(G \to \gamma\gamma)$, as a function of graviton mass, for data in the central-central channel, shown on the left, and the central-plug, shown on the right. Full systematic errors are applied. The limit without systematics is also shown for comparison. 146

7.7 The 95% CL upper limit for $\sigma \cdot BR(G \to \gamma\gamma)$, as a function of graviton mass, for the central-central and central-plug channels combined. Full systematic errors are applied. The limit without systematics is also shown for comparison. 147

7.8 95% CL upper limit on the production cross-section times branching fraction of an RS graviton decaying to two photons ($\sigma \cdot BR(G \to \gamma\gamma)$), as a function of graviton mass, with full systematic errors applied. The predicted ($\sigma \cdot BR$) curves for $k/\overline{M}_{Pl} =$ 0.01, 0.025, 0.05, 0.07 and 0.1 are also shown. 148

7.9 95% CL exclusion domain in the plane of $k/\overline{M}_{Pl}$ versus graviton mass, for an integrated luminosity of 1155 pb^{-1} for central-central decays and 1070 pb^{-1} for central-plug decays. 149

8.1 95% CL upper limit on the production cross-section times branching fraction of an RS graviton decaying to two photons ($\sigma \cdot BR(G \to \gamma\gamma)$), as a function of graviton mass, with full systematic errors applied. The predicted ($\sigma \cdot BR$) curves for $k/\overline{M}_{Pl} =$ 0.01, 0.025, 0.05, 0.07 and 0.1 are also shown. 152

8.2 95% CL exclusion domain in the plane of $k/\overline{M}_{Pl}$ versus graviton mass, for an integrated luminosity of 1.2 fb^{-1}. 152

A.1 Diphoton invariant mass 155

A.2 Phoenix plug tracking efficiency as a function of η, where $1.2 < |\eta| < 2.8$ 156

A.3 Standalone plug tracking efficiency as a function of η, where $1.2 < |\eta| < 2.8$ 156

C.1 The 95% C.L. limits on RS graviton production for the dielectron, diphoton and combined limits, with the $k/\overline{M}_{Pl}$ model lines overlayed. 160

C.2 95% CL exclusion domain in the plane of $k/\overline{M}_{Pl}$ versus graviton mass, for the combined dielectron and diphoton channels. 161

List of Tables

1.1 Properties of the leptons, showing the charge (e), mass (MeV/c^2) and the corresponding anti-particle [1]. 4

1.2 Properties of the quarks showing the charge (e), current mass (MeV/c^2) and anti-particle [2]. 5

1.3 The elementary gauge bosons of the Standard Model. The graviton is included here for completion [2]. 6

2.1 Summary of data taking periods at CDF. 31

2.2 Design parameters of the tracking systems. 38

2.3 COT design parameters. 41

2.4 Properties of Run II calorimeters. 45

3.1 DIPHOTON_12 and DIPHOTON_18 trigger requirements. . . . 55

3.2 ULTRA_PHOTON_50 and SUPER_PHOTON_70 trigger requirements. 56

3.3 ELECTRON_CENTRAL_18 trigger requirements. 57

3.4 Offline track reconstruction. 61

3.5 Scale factors as applied to data. 66

3.6 Scale factors as applied to Monte Carlo. 66

3.7 Integrated luminosity ($\mathcal{L}$) for central and plug photon and electron data samples, showing the L3 trigger paths used. 68

3.8 Central photon candidate selection criteria. 73

3.9 Plug photon candidate selection criteria. 73
3.10 Central electron candidate selection criteria. 78
3.11 Plug electron candidate selection criteria. 79

4.1 Signal acceptance for the $G \rightarrow \gamma\gamma$ decay channel, measured using simulation, showing statistical errors only. 82
4.2 Angular distributions in graviton production for the diphoton decay mode. θ^* is the polar angle of the outgoing particle in the graviton rest frame. 83
4.3 Fractional variation in acceptance in central-central events, resulting from a 1% fluctuation in the E_T threshold. 86
4.4 Fractional variation in acceptance in central-plug events, resulting from a 1% fluctuation in the E_T threshold. 87
4.5 Acceptance as a function of graviton mass for CTEQ5L and different MRST parton distribution functions, showing statistical errors. 89
4.6 Difference in acceptance caused by changing the parton distribution function, as a function of graviton mass. 89
4.7 Difference in acceptance as a function of graviton mass, showing systematic errors, due to differences in the initial and final state radiation. 90

5.1 Additional photon selection cuts applied to jet data for cosmic ray and halo event removal [57]. 95
5.2 (N-1) efficiencies for $\chi^2 < 20$ and $\chi^2 < 50$ using jet data samples. 96
5.3 Loose selection cuts for the probe electron in the central calorimeter. 100
5.4 Loose selection cuts for the probe electron in the plug calorimeter. 100

5.5 Cumulative efficiencies for central electron selection cuts for data and simulation, showing statistical errors, for the first dataset. 102
5.6 Cumulative efficiencies for central electron selection cuts for data and simulation, showing statistical errors, for the second dataset. 103
5.7 Cumulative efficiencies for plug electron selection cuts for data and simulation, showing statistical errors, for the first dataset. . 103
5.8 Cumulative efficiencies for plug electron selection cuts for data and simulation, showing statistical errors, for the second dataset. 104
5.9 Total central and plug electron efficiencies and correction factors for first dataset, with statistical and systematic errors. 104
5.10 Total central and plug electron efficiencies and correction factors for second dataset, with statistical and systematic errors. 105
5.11 Total efficiency (acceptance * efficiency) for the $G \rightarrow \gamma\gamma$ decay channel, measured using simulation, showing statistical errors only. 109

6.1 Loose event selection for photons reconstructed in the CEM calorimeter. 122
6.2 Loose event selection for photons reconstructed in the PEM calorimeter. 122
6.3 Fractional variation in *DIPHOX* prediction for central-central events using $M = M_f = Q/2$ and $M = M_f = Q * 2$. 127

7.1 The 95% CL lower limits on the mass on the RS graviton for $0.01 < k/\overline{M}_{Pl} < 0.1$. 149

A.1 Plug electron rejection factors calculated using simulated $Z \rightarrow ee$ events. 154

A.2 Plug electron rejection factors calculated in data. 154

Chapter 1

Introduction

As far back as the 6th century BC, the idea of all matter being composed of elementary particles was studied by the ancient Greek philosophers. In the 19th century, John Dalton, while studying the relationships of reactants and products in chemical reactions, concluded that each element of nature was composed of a single, unique type of fundamental particle, which he named 'atom', after the Greek 'atomos', meaning indivisible. Near the end of the century, physicists discovered that atoms were in fact conglomerates of even smaller particles. By the mid-1930s, Rutherford had shown that atoms have nuclei, quantum theory had explained atomic spectra and electron orbitals, and nuclear isotopes were no longer a mystery after the discovery of the neutron. The understanding of the building blocks of all matter appeared to be almost complete. The cyclotron was also developed in the 1930s, making it possible to probe matter with a high-energy particle beam. By the late 1960s, the new high-energy accelerators were producing hundreds of new 'elementary' particles. Theoretical breakthroughs then led to the development of a common gauge theory approach to three of the forces of nature, supported in the 1970s by discoveries of weak neutral currents and evidence for the physical reality of quarks; the fundamental constituents of the multitude of previously discovered

particles. With ever increasing energies, experiments are now able to probe ever smaller distances with the aim of identifying finer structure within matter, with the Tevatron collider at the Fermi National Accelerator Laboratory using the highest energies currently available.

Through a combination of theory and experiment, all the phenomena of particle physics so far observed, in terms of the properties and interactions of a small number of elementary particles (treated as point particles without internal structure or excited states), attempt to be explained by the Standard Model (SM). There are two classes of elementary particles; fermions and bosons. Fermions have half integer intrinsic spin and make up all known matter in the universe (the quarks and leptons). Each fermion has its corresponding anti-particle, having the same mass and spin but opposite sign of all internal quantum numbers. Interactions between these particles are mediated through the second set of elementary particles, bosons, which carry integer spin. These fundamental interactions are described by four forces: electromagnetic, weak, strong and gravitational. The Standard Model is a theory which describes the first three of these forces, with quantum field theory providing the mathematical framework, treating each particle in terms of a mathematical field.
There are reasons to believe, as discussed in Section 1.2, that the Standard Model is not complete, but is an effective theory: a low-energy approximation of a more complete, and as yet unknown, theory. This new theory would be expected to explain the phenomena described in the SM, removing its many arbitrary parameters and resolving currently unanswerable questions, as well as having associated new phenomena.
In the following sections, the elementary particles and forces are introduced, as described by the SM, together with some of the questions that, as yet, remain unsolved. Section 1.2.1 describes the Hierarchy problem in greater detail

and introduces the Beyond-the-Standard Model (BSM) extension of extra dimensions as a solution. In this thesis, I consider the Randall-Sundrum (RS) warped extra dimension model, performing an experimental search for this scenario, through RS graviton decay in the diphoton channel, described in detail in Section 1.2.3.

1.1 The Standard Model

1.1.1 The Fermions

Leptons

The leptons, fermions that do not experience the strong force, are divided into three generations, each represented by a pair of particles originating from a weak $SU(2)$ doublet. This has one charged particle with mass and a massless neutral particle, the neutrino, in each generation. All charged leptons have a single unit of negative charge (positive for their anti-particles), and carry a quantum number associated with the generation, e.g. the electron has $L_e = 1$ and the positron $L_e = -1$. Until recently, this was believed to be conserved in all interactions. Evidence from experiment now suggests, however, that there can be mixing in the neutrino sector. This is discussed in more detail in Section 1.1.3. The properties of the leptons are summarised below in Table 1.1.

Quarks

Quarks, which interact through all four of the fundamental forces, are divided into six 'flavours', representing quantum numbers that are conserved under the strong, but not weak, interactions. This flavour changing in weak interactions also dictates the extent of CP violation, (the product of charge conjugation

	Particle	Charge (e)	Mass (MeV/c^2)	Anti-particle
1st generation	e^-	-1	0.510998901 $\pm$ 0.000000044	e^+
	ν_e	0	< 0.003	$\bar{\nu_e}$
2nd generation	μ^-	-1	105.6583692 $\pm$ 0.0000094	μ^+
	ν_μ	0	< 0.19	$\bar{\nu_\mu}$
3rd generation	τ^-	-1	1776.99 $\pm$ 0.29	τ^+
	ν_τ	0	< 18.2	$\bar{\nu_\tau}$

Table 1.1: Properties of the leptons, showing the charge (e), mass (MeV/c^2) and the corresponding anti-particle [1].

and parity), that is allowed in the SM. Quarks are always found in bound states (hadrons), composed of two quarks (mesons) or three quarks (baryons). The exception to this is the top quark which may, in high-energy collisions, decay prior to hadronisation due to its large mass. This allows for direct mass measurement of the top quark only, with large errors on the masses of the other flavours. There exists a second internal quantum number, 'colour', which allows for the existence of baryons containing three quarks of the same flavour with parallel spins, forbidden by the Pauli exclusion principle. Colour is a gauged $SU(3)$ symmetry, therefore quarks come in three colors (red, green, and blue). The properties of the quarks are given in Table 1.2.

1.1.2 The Gauge Bosons

The interactions of elementary particles occur through exchange of gauge bosons, with the coupling displaying a gauge symmetry. These are the propagators of the fundamental forces in the SM. There are three types of gauge boson, each corresponding to one of the three SM interactions, with the photon transmitting the electromagnetic force, the W and Z bosons mediating

	Particle	Charge (e)	Mass (MeV/c^2)	Anti-particle
1st generation	u	+ 2/3	1.5 - 3.0	$\bar{u}$
	d	- 1/3	3 - 7	$\bar{d}$
2nd generation	c	+ 2/3	1250 $\pm$ 90	$\bar{c}$
	s	- 1/3	95 $\pm$ 25	$\bar{s}$
3rd generation	t	+ 2/3	174200 $\pm$ 3300	$\bar{t}$
	b	- 1/3	4200 $\pm$ 70	$\bar{b}$

Table 1.2: Properties of the quarks showing the charge (e), current mass (MeV/c^2) and anti-particle [2].

the weak force and the gluons propagating the strong force. The gauge bosons represent the quanta of the gauge fields, therefore there are as many bosons as generators of the field. Interactions by means of exchange of photons are described by Quantum Electrodymanics and have the gauge group $U(1)$. The W and Z bosons correspond to the three generators of $SU(2)$ of the weak interaction and Quantum Chromodynamics, the theory of the strong interaction, has 8 generators from the $SU(3)$ group, corresponding to the eight gluons. The gravitational force may also be carried by a boson but, due to the lack of a consistent quantum theory of gravitation and of any experimental evidence, it is not possible to say whether this would be a gauge boson. Gauge invariance in General Relativity does, however, have a similar role; the physical laws are invariant under arbitrary coordinate transformations [3]. The properties of the gauge bosons are summarised in Table 1.3.

1.1.3 Quantum Electrodynamics (QED)

QED describes the interaction of fermions through the exchange of photons, the magnitude of which can be calculated using perturbation theory, and can

Gauge Boson	Force	Spin	Mass (GeV/c^2)	Charge (e)	Range (fm)
Photon (γ)	Electromagnetic	1	0	0	∞
$W^{\pm}$	Charged Weak	1	80.403 ± 0.029	± 1	$\approx 10^{-3}$
Z	Neutral Weak	1	91.1876 ± 0.0021	0	$\approx 10^{-3}$
Gluon (g)	Strong	1	0	0	$<\approx 1$
Graviton (G)	Gravity	2	0	0	∞

Table 1.3: The elementary gauge bosons of the Standard Model. The graviton is included here for completion [2].

predict the probability of a particular, experimentally verifiable, outcome. Predictions of QED agree with experiment with an accuracy of $\sim 10^{-12}$ [4], making it the most accurate theory constructed to date. The Lagrangian for a free Dirac field Φ for a fermion, having mass m, is given by:

$$\mathcal{L}_{free} = \bar{\Phi}(x)(i\partial\!\!\!/ - m)\Phi(x) \tag{1.1}$$

where $\partial\!\!\!/ \equiv \gamma^{\mu}\partial_{\mu}$ and γ^{μ} are the Dirac matrices. This Lagrangian is invariant under under global phase transformations $U(1)$, and the requirement of local gauge invariance results in the introduction of a vector field A_{μ}, identified with the photon. The total Lagrangian, shown in Equation 1.2, is obtained through the addition of a kinetic term to account for the propagation of the vector field, which is also gauge invariant.

$$\mathcal{L}_{QED} = \bar{\Phi}(x)(i\not{\mathcal{D}} - m)\Phi(x) - \frac{1}{4}F_{\mu\nu}(x)F^{\mu\nu}(x) \tag{1.2}$$

For a particle of charge eQ the covariant derivative $\mathcal{D} = \partial_{\mu} + ieQA_{\mu}$ and the field strength tensor $F_{\mu\nu} = \partial_{\mu}A_{\nu} - \partial_{\nu}A_{\mu}$, where μ and ν run over the four spacetime coordinates. To preserve invariance under local gauge transformations, a mass term involving the gauge field is not permissible, consistent with experimental observation.

The electrodynamic and weak interactions are unified in electroweak theory [5]. Despite appearing as two distinct forces at low energy, they are two aspects of the same force. Above the unification energy, ($\sim 10^3$ GeV), they merge into the single electroweak force. The weak group symmetry, $SU(2)_L$, where L signifies that the weak bosons couple only to left-handed fermions, must be preserved when constructing the isospin triplet of weak currents. It is therefore necessary to modify the $U(1)$ electromagnetic group generator to account for right-handed interactions. The electric charge $U(1)$ group generator is replaced with the hypercharge Y, defined as

$$Q = T_3 + \frac{Y}{2} \tag{1.3}$$

where T_3 is the third component of the weak isospin of the the particle. The theory requires weak isospin and hypercharge to be conserved, with the Lagrangian inavriant under the local gauge transformation $SU(2)_L \otimes U(1)_Y$. The non-zero masses of the weak gauge bosons require the mechanism of spontaneous symmetry breaking, as the addition of a mass term to the Lagrangian, even its simplest form ($-m\psi\psi$), removes the gauge invariance. This symmetry breaking generates a new Higgs particle, as yet experimentally unconfirmed. The Higgs mechanism, described in detail below, then gives rise to the large masses of the weak bosons.

Electroweak Symmetry Breaking

The spontaneous symmetry breaking (SSB) of the electroweak $SU(2)_L \otimes U(1)_Y$ symmetry was proposed to accommodate the masses of the weak gauge bosons, ~ 80 GeV/c^2 and 91 GeV/c^2 respectively [6]. To preserve the gauge symmetry, the addition of an explicit mass term is forbidden, but the Lagrangian predicts the W and Z to be massless. SSB (defined as a system that is symmetric with respect to some symmetry group but which has a vacuum state that is not

symmetric) introduces a term to the Lagrangian that preserves the symmetry but allows the selection of a mass scale. A complex doublet of scalar fields are introduced, adding a potential to the Lagrangian:

$$V = \lambda(\phi^\dagger\phi)^2 - \mu^2\phi^\dagger\phi \tag{1.4}$$

where ϕ denotes the scalar field and which has a non-zero minimum at $|\phi| = \sqrt{\mu^2/2\lambda} \equiv \nu/\sqrt{2}$ for $\lambda,\ \mu^2 > 0$. It is this acquisition of a non-zero vacuum expectation value (VEV) (246 GeV) that spontaneously breaks the electroweak gauge symmetry. The quadratic terms in the physical boson field, shown in Equation 1.5, then give the W and Z bosons their masses, shown in Equation 1.6.

$$\mathcal{L}_{\text{mass}} = \frac{g^2\nu^2}{4}W_\mu^+W^{-\mu} + \frac{(g^2+g'^2)\nu^2}{8}Z_\mu Z^\mu \tag{1.5}$$

$$m_W = \frac{1}{2}\nu g \quad \text{and} \quad m_Z = \frac{1}{2}\nu\sqrt{g^2+g'^2} \equiv \frac{m_W}{\cos\theta_W} \tag{1.6}$$

The existence of the non-zero VEV also gives rise to the fermion masses, through interaction with the Higgs field, which also gives mass to the Higgs boson itself, and is the only known mechanism capable of giving mass to the gauge bosons that is also compatible with gauge theories. It does not, however, predict the fermion masses, which remain as free parameters in the SM.
According to the Higgs mechanism, as the particles acquire mass, they change handedness; left-handed particles become right-handed and vice versa. Experimentally, neutrinos have been shown to always be left-handed [7]. The theory therefore predicts that neutrinos can never acquire mass. In 1998, however, the first evidence for neutrino mass was announced [8], showing that at the very least the theory is incomplete. Several extensions to the SM have attempted to explain this, such as right-handed neutrinos that interact much

more weakly than any other particles and heavy right-handed neutrinos that are only created for a brief moment prior to interacting with the Higgs boson, producing light left-handed neutrinos [9].

1.1.4 Quantum Chromodynamics (QCD)

QCD is the quantum field theory describing the interactions of the quarks and gluons, and differs from QED in its non-Abelian nature (the gluon exhibits self-interaction). To explain the experimental observations of hadron spectroscopy, a three-fold colour degree of freedom is introduced, each quark carrying a single colour, so giving three quarks of each flavour, for a total of 18 quarks. An octet of bicoloured gluons then mediate the interactions between the quarks. The colour singlet does not contribute to strong interactions as it is colourless, so unable to mediate forces between colour charges. Emission of a gluon may lead to a quark changing colour, but the colour of the entire system is conserved. The Lagrangian must therefore be constructed to be invariant under both global and local gauge transformations. The strong interaction is described using the $SU(3)_{\text{colour}}$ gauge symmetry, which introduces eight massless vector fields, the gluons. The Lagrangian for quark fields q_a having colour a, written analogously with that of QED, is given by:

$$\mathcal{L}_{QCD} = \sum_{\text{flavours}} \bar{q}_a(x)(i\not{\mathcal{D}}_{ab} - m\delta_{ab})q_b(x) - \frac{1}{4}F^A_{\mu\nu}(x)F^{A\mu\nu}(x) \tag{1.7}$$

where

$$F^A_{\mu\nu} = \partial_\mu A^A_\nu - \partial_\nu A^A_\mu - f^{ABC}A^B_\mu A^C_\nu \tag{1.8}$$

and f^{ABC} are the structure constants of the group. The eight $SU(3)$ matrices $\mathbf{t}$ are contained in the covariant derivative; $(\mathcal{D}_\mu)_{ab} = \partial_\mu\delta_{ab} + ig_s(\mathbf{t}\cdot\mathbf{A}_\mu)_{ab}$.

The short range of the strong force arises from the fact that the strong

coupling constant, α_s, is a function of the separation distance between the interacting particles, i.e. it is a running coupling constant. Unlike QED, where each vertex introduces a factor of $\alpha = 1/137$, allowing the theory to be perturbative, $\alpha_s > 1$ at nuclear distances, but decreases at shorter distances. The potential for strong interactions at distances ≤ 0.1 fm is given by:

$$V(r) = -\frac{4}{3}\frac{\alpha_s}{r} \tag{1.9}$$

where r is the distance between the colour charges. The scaling of α_s then depends of the momentum transfer, Q^2, between the colour charged particles:

$$\alpha_s(Q^2) = \frac{12\pi}{(11n - 2f)\log(\frac{Q^2}{\Lambda^2})} \tag{1.10}$$

where n is the number of colours, f is the number of flavours and Λ is an experimentally determined parameter ~ 200 MeV. For large momentum transfer ($\alpha_s \to 0$ as $Q^2 \to \infty$), the strong coupling constant then becomes small, allowing the partons to be treated as essentially free particles. When Q^2 is of the same order as Λ, the perturbative description is no longer valid, leading to the asymptotic freedom of the quarks at short distances, legitimising the Feynman calculus in the high-energy regime and strong binding at large distances (quark confinement).

At $r \geq 0.1$ fm, the potential becomes a linear function, $V(r) \approx \lambda r$, where λ is a constant of the order of 1 GeV/fm. At large distances it is energetically more favourable that, as the quarks are pulled apart, a new quark-antiquark pair is produced, forming colourless hadrons with the original pair, meaning that only colourless objects are observed in nature.

1.1.5 Parton Distribution Functions

The composite structure of the proton and antiproton must be accounted for when predicting the interactions between them. The elementary entities within the (anti)proton are referred to as partons, and are described by parton distribution functions (PDFs). These are the valence quarks, which define the quantum numbers, sea quarks (virtual quark-antiquark pair produced from the splitting of a gluon) and the gluons themselves. The PDF gives the probability that a specific parton will have a fraction, x, of the (anti)proton mometum. For the proton-antiproton collisions considered in this analysis, each incident particle has an energy of 980 GeV, giving a centre-of-mass energy squared of $(1.96\text{ TeV})^2$. The square of the energy between the two interacting partons is then give by $\hat{s} = x_1 \cdot x_2 \cdot (1.96\text{ TeV})^2$. When probed at low energy (< 1 GeV), the proton can be treated as a single particle, with its composite nature only becoming apparent at energies ~ 10 GeV, where the valence quarks dominate the interactions. Above these energies, the gluons and sea quarks dominate. The probability of a parton carrying a momentum fraction x is determined by the probability distribution functions, which are subject to several normalisation rules. The probability that a parton of flavour a within the proton will have momentum fraction x for momentum transfer q^2 is given by the function $f_a^P(x, q^2)$. For a proton this implies:

$$\int_0^1 [f_u^P(x,q^2) - f_{\bar{u}}^P(x,q^2)]dx = 2 \quad \text{and} \quad \int_0^1 [f_d^P(x,q^2) - f_{\bar{d}}^P(x,q^2)]dx = 1 \tag{1.11}$$

as there are two valence u quarks and one d quark, the contribution from the antiquarks coming from the sea quarks. The total momentum contributions from all partons must then be unity:

$$\sum_a \int_0^1 x f_a^P(x, q^2) dx = 1 \tag{1.12}$$

To predict a theoretical cross-section for a $p\bar{p}$ interaction, all parton flavours and momenta are weighted by the PDF and integrated over all phase space. The full cross-section $p\bar{p} \to cd$ is calculated by summing over all quark flavours and integrating over all momenta (x_1 and x_2):

$$\sigma(p\bar{p} \to cd) = \sum_a^p \sum_b^{\bar{p}} \int_0^1 \int_0^1 d^2\sigma(ab \to cd) \tag{1.13}$$

where

$$d^2\sigma(ab \to cd) = \hat{\sigma}(ab \to cd) f_a^P(x_1, q^2) f_b^{\bar{P}}(x_2, q^2) dx_1 dx_2 \tag{1.14}$$

and $\hat{\sigma}$ is the matrix element cross-section for the parton interaction $ab \to cd$. A set of 'global' PDFs has been formed using measurements from several experiments, over a range of x and q^2. In this analysis, CTEQ5L [10] is used for the primary PDFs, with the effect of various PDFs on event kinematics being compared in Section 4.2.2.

1.2 Limitations of the Standard Model

The Standard Model gauge theories $SU(3)_C \otimes SU(2)_L \otimes U(1)_Y$ show excellent agreement with experimental data from high-energy experiments. Recent deviations, however, such as the discovery of neutrino oscillations (Section 1.1.3), its failure to answer questions such as why the fermions have the masses they do, the origin of flavour and its failure to provide a dark matter candidate, indicate that is not a complete theory. It also contains 19 empirically determined parameters and only unifies two of the four interactions. It is theoretically desirable to have a single, Grand Unified Theory (GUT) [11] describing all

of the fundamental interactions. It is therefore believed that the SM is an effective theory, a low-energy approximation of a more complete theory, which would contain the physics currently described by the SM, as well as explaining the questions it fails to answer, and have associated new phenomena. Many searches are ongoing for physics beyond-the-Standard Model (BSM).
The following section describes a further problem, the Hierarchy problem; the question of why the electroweak scale mass is sixteen orders of magnitude smaller than the Planck scale mass, which characterizes gravity's strength. This question cannot currently be answered within the framework of the SM. A possible solution is provided through the introduction of extra dimensions of space, discussed in Section 1.2.2, with a detailed of description of the Randall-Sundrum (RS) warped extra dimension model, used in this analysis, given in Section 1.2.2. Its associated collider phenomenology is described in Section 1.2.3.

1.2.1 The Hierarchy Problem

Firstly, consider the Hierarchy problem in the context of a GUT, where the problem was first identified. Although the Higgs mass must be of the order of the weak symmetry breaking scale ($M_{EW} \sim 10^3$ GeV), it is partnered with a strongly interacting particle, such that the weak and strong force should be interchangeable at high energy. Current limits on the proton lifetime indicate that the strongly interacting Higgs partner must have a mass of the order $M_{GUT}(\sim 10^{16}$ GeV), resulting in two particles, related by the GUT force symmetry, with enormously different masses. In addition to this, quantum contributions from the self-energy corrections (one-loop diagrams) have quadratic mass divergences which must be added to the classical Higgs mass to obtain the physical mass. Without the introduction of new physics, it must be assumed that the classical mass takes precisely the value that would cancel the

large quantum contribution, requiring fine-tuning to the order of one part in 10^{13}.

Looking at the problem in its wider context, self-energy corrections still generate very large contributions to the Higgs mass. Any theory attempting to include gravitational interactions contains the large disparity between the electroweak scale ($M_{EW} \sim 10^3$ GeV) and the Planck scale ($M_{Pl} \sim 10^{19}$ GeV), which determines the strength of gravitational interactions (from Newton's laws, the gravitational strength is inversely proportional to the second power of the Planck energy [12]). The Hierarchy problem may therefore be phrased as the remarkable weakness of gravity compared with all the other known forces. The contribution to the Higgs mass, from radiative corrections, is illustrated in Figure 1.1 for corrections due to a gauge boson, Higgs boson and top quark (fermions in general).

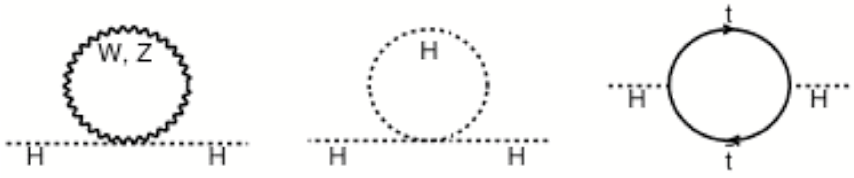

Figure 1.1: Radiative corrections to the Higgs boson mass from gauge bosons, the Higgs boson and fermion loops.

Consider the first order perturbative correction to the Higgs boson mass (m_H) for the one loop correction to m_H^2 from a fermion F of mass m_F and with coupling strength λ_F of the Higgs to the fermion. The correction is given by [13]:

$$\Delta m_H^2 = \frac{|\lambda_F|^2}{16\pi^2}\left[-2\Lambda_{UV}^2 + 6m_F^2 \ln\left(\frac{\Lambda_{UV}}{m_F}\right) + ...\right] \tag{1.15}$$

where Λ_{UV} is the momentum cutoff parameter used to regulate the loop integral. The first term diverges quadratically with the momentum cutoff. The most important contribution occurs in the case of the top quark ($\lambda_F \approx 1$), as the Higgs-fermion coupling is proportional to the fermion mass. Putting $\Lambda_{UV} \sim M_{Pl}$, the radiative correction becomes of the order of the Planck scale:

$$\Delta m_H^2 \approx (10^{19}\ GeV/c^2)^2 \tag{1.16}$$

Without extension to the SM, the required mass of the Higgs can only be achieved through the cancellation of the quadratic corrections by a fine-tuning of the parameters to the order of one part in 10^{16} (as opposed to 10^{13} in the context of a GUT). This must occur at every order in perturbation theory and is considered extremely unnatural.

1.2.2 Extra Dimensions

Several BSM theories have been developed to resolve the Hierarchy problem, such as supersymmetric theories (SUSY) [14], where there is an extended symmetry between bosons and fermions, allowing the quadratic divergences to cancel and removing the need for fine-tuning for the bare Higgs mass. One disadvantage of this approach is the large number of new parameters that must be introduced, with even the simplest SUSY model, minimal SUSY [15], introducing 105 new parameters. Other models, such as the strong coupling theories technicolor [16] and topcolor [17], introduce a new scale for gauge interactions with a new set of fermions at the 1-10 TeV scale.

A very different approach to the problem attempts to solve the Hierarchy through the modification of gravity itself, by proposing the existence of extra spatial dimensions, with the geometry of these dimensions being responsible for the hierarchy. There are many extra dimensional models, with signatures

that may be tested through high-energy collisions. The primary models are the ADD and RS models. In the ADD model, proposed by Arkani-Hamed, Dimopoulos and Dvali in 1998 [18], the electroweak scale is the only fundamental scale, with a fundamental $(4 + n)$-dimensional Planck scale being related to an effective 4-dimensional scale through the volume of compactified dimensions (V_n):

$$M_{Pl}^2 = V_n M_{Pl(4+n)}^{2+n} \tag{1.17}$$

M_{Pl} may then be set to $\sim$ 1 TeV, removing the hierarchy, by requiring the extra dimensions be large. Current limits from CDF set $M_{Pl(4+n)} >$ 1.2 TeV [19].

Alternatively, the hierarchy may be generated by the curvature of an extra dimension, rather than through size, as in the Randall-Sundrum model, used in this analysis. This model is discussed in detail below.

The Randall-Sundrum Model

In the Randall-Sundrum (RS) model, proposed in 1999 [20], the hierarchy is removed through the curvature of an extra dimension, generated through a non-factorisable metric; the 4-dimensional metric is multiplied by a 'warp' factor which is a rapidly changing function of the additional dimension, as shown in Equation 1.18:

$$ds^2 = e^{-2kr_c\phi}\eta_{\mu\nu}dx^\mu dx^\nu + r_c^2 d\phi^2 \tag{1.18}$$

where k is a scale of the order of the Planck scale, x^μ are the 4-dimensional coordinates and $0 \leq \phi \leq \pi$ is the coordinate for the extra dimension whose finite size is determined by the compactification radius, r_c and $\eta_{\mu\nu} = \text{diag}(1,-1,-1,-1)$. This metric is a solution to a set-up with an additional spatial dimension

of finite size, bounded by two 3-branes separated by a distance πr_c, in which gravity propagates. The SM particles are confined to the $\phi = \pi$ 'TeV' brane, while the gravitational wavefunction is localised at $\phi = 0$ (the 'Planck' brane). The curvature takes a 5-dimensional Anti-de-Sitter form (AdS_5). In this space, 4-dimensional mass scales are related to 5-dimensional input mass parameters and the warp factor, $e^{-2kr_c\pi}$, and the scale of physical phenomena on the TeV-brane is specified by:

$$\Lambda_\pi \equiv \overline{M}_{Pl} e^{-kr_c\pi} \tag{1.19}$$

where $\overline{M}_{Pl} = M_{Pl}/\sqrt{8\pi} = 2.4 \times 10^{18}$ GeV is the effective 4-dimensional (reduced) Planck scale. To remove the hierarchy, $\Lambda_\pi \sim$ TeV, which is obtained through setting $kr_c \simeq 11-12$, a configuration which does not require the use of fine tuning. The TeV scale may therefore be thought of as being fundamental, with the Planck scale arising from the small overlap of the graviton wave function in the fifth dimension with the TeV-brane. The Kaluza-Klein (KK) tower of graviton states [21], resulting from the compactification, gives a mass spectrum of modes in the effective 4-dimensional theory on the 3-brane, given by:

$$m_n = kx_n e^{-kr_c\pi} = x_n (k/\overline{M}_{Pl})\Lambda_\pi \tag{1.20}$$

where x_n are the roots of the first-order Bessel function, i.e. $J_1(x_n) = 0$, the KK tower states being the coefficients of a Bessel expansion which replaces the Fourier series of a flat geometry. Any mass parameter m_0 on the 3-brane will then correspond to a physical mass:

$$m = e^{-kr_c\pi} m_0 \tag{1.21}$$

The phenomenological implications are very distinctive, with the large mul-

tiplicity of states being key. The first KK mode is the massless graviton of the effective 4-dimensional theory, which couples with the usual 4-dimensional strength ($1/\overline{M}_{Pl}$), while all massive KK states couple with strength ($1/\Lambda_\pi$), of order of the weak scale, allowing each excited state to be individually detected as a resonance in an accelerator, up to the kinematic limit. In addition, the spacing of the states is dependent on successive roots of J_1, giving a distinctive signature, as discussed further in Section 1.2.3.

1.2.3 Collider Phenomenology

The RS model is detectable in colliders through the process of virtual graviton exchange, its signature being a series of narrow heavy graviton resonances. These may be individually detected in the dilepton, dijet or diboson channel, as an excess of events leading to an overall modification of the cross-section and angular distribution at high invariant mass, with branching fractions shown in Figure 1.2.

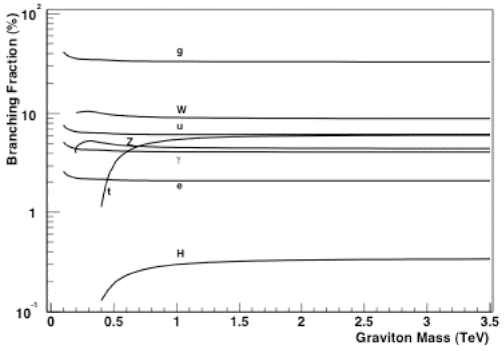

Figure 1.2: Graviton branching fractions for the Randall-Sundrum model [22].

The deviation in angular distribution arises from the spin-2 nature of the graviton. A spin-0 resonance has a flat angular distribution, spin-1 a parabolic shape and spin-2 a quartic distribution [22]. This property of the graviton could be used to distinguish an RS resonance from other new physics, such a Z' boson, which would otherwise look like the first resonance of an RS graviton. The ability to distinguish between these angular distributions, however, is dependent on the available statistics. In this analysis, only the invariant mass spectrum is studied, due to the low statistics at high invariant mass. It also uses the diphoton channel, which has the advantage of having a branching ratio of twice that of dielectrons or dimuons. This arises as a consequence of the combination of spin factors (spin 1 for photons, spin 1/2 for electrons) and decay through either the s or p wave states [23]. At high centre-of-mass energy, the dijet channel is expected to have large QCD background. Virtual graviton exchange in the diphoton channel can occur from a gluon-gluon (gg) initiated process or a quark-antiquark ($q\bar{q}$) initial state, as shown in Figure 1.3.

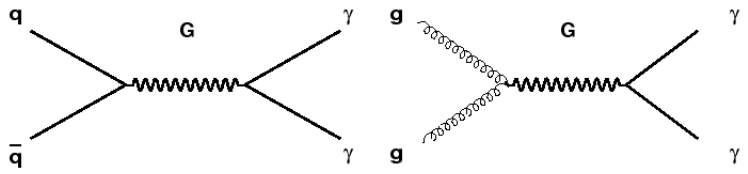

Figure 1.3: Feynman diagrams for virtual graviton exchange in the diphoton channel

.

The width (Γ) and location (m) of the resonances are dependent on the parameters Λ_π and $k/\overline{M}_{Pl}$, where, for the first KK resonance, $\Lambda_\pi = m_1\overline{M}_{Pl}/kx_1$ and $\Gamma_1 = \rho m_1 x_1^2(k/\overline{M}_{Pl})^2$. Here x_1 is the first non-zero root of the J_1 Bessel

function and ρ is a constant, the value of which depends on the number of decay channels available. Assuming the graviton decays only to SM particles, ρ takes a fixed value. Constraints from theoretical assumptions lead to two additional requirements. These are $\Lambda_\pi \leq 10$ TeV, as the scale of physics on the TeV-brane must be around the elecroweak scale to remove the hierarchy, and $0.01 \leq k/\overline{M}_{Pl} \leq 0.1$, as k must be large enough to remove the apparent weakness of gravity, but cannot exceed 0.1 due to bounds on the curvature of the AdS_5 space [23]. The individual KK excitations, for values of $k/\overline{M}_{Pl}$ between 1.0 and 0.01, are illustrated in Figure 1.4 for a KK graviton of mass 700 GeV/c^2, showing the first excitation as would be seen at the Tevatron, and for a 1500 GeV/c^2 graviton and its subsequent tower states, as would be seen at the Large Hadron Collider (LHC), the future higher energy collider.

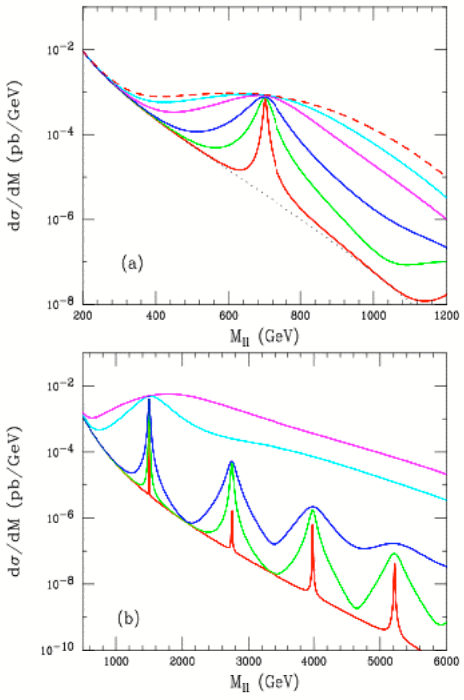

Figure 1.4: A 700 GeV/c^2 KK graviton, decaying to the dilepton channel, for $k/\overline{M}_{Pl}$ = 1.0, 0.5, 0.1, 0.05, and 0.01, from top to bottom. Below, a 1500 GeV/c^2 KK graviton, and its subsequent tower states [24].

Once kinematically allowed, the KK excitations will decay to lighter graviton states, meaning that for higher mass resonances the peak of the cross-section will decrease. This does not apply to the peak of the first resonance, as it cannot decay to a lighter graviton.

For a fixed value of $k/\overline{M}_{Pl}$, the resonance width increases with mass, as seen in the tower states in Figure 1.4. The reconstructed invariant mass shape will therefore depend on the width of the graviton generated and the detector resolution. For the range of widths considered ($0.01 \leq k/\overline{M}_{Pl} \leq 0.1$), the detector resolution is considered to dominate the intrinsic width of the RS graviton [25]. This is taken into account in the method for setting limits through the use of a simulated signal. This requires that the detector resolution be well modeled in simulation, which is verified through the comparison of data and simulation for Z bosons decaying as $Z \rightarrow e^+e^-$, a very clean, well understood channel. This comparison is shown in Figure 1.5 for events in which both decay products are reconstructed in the CDF central calorimeter (top), see Section 2.2.3 for calorimeter description, or where one event is reconstructed centrally and the other is reconstructed in the plug (bottom). (See Section 5.2.1 for details of Z boson selection).

Previous Best Limits

Constraints on the RS model come from theoretical restrictions, as previously mentioned, graviton searches and precision electroweak data, where contributions to a large set of electroweak observables from the KK gauge tower at tree-level are analysed [23]. Figure 1.6 shows the previous best limits on RS graviton production, as a function of graviton mass against $k/\overline{M}_{Pl}$. The dotted line shows the experimental limit obtained from the combination of the dimuon and diEM (combined electron and photon) channels, using 246 pb^{-1} and 275 pb^{-1} of data respectively, using the D0 detector [26]. The area below

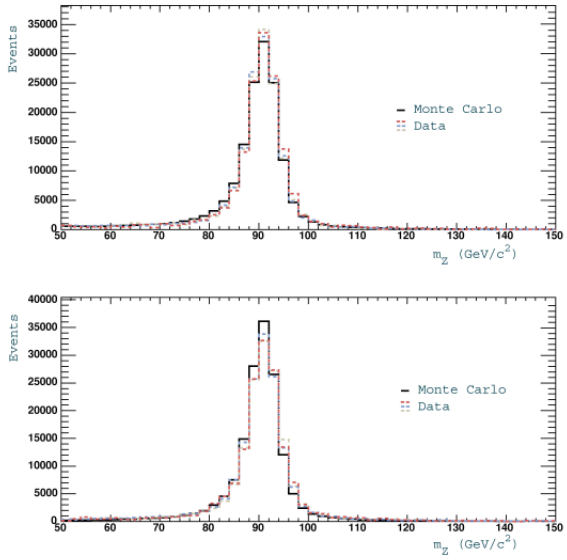

Figure 1.5: Comparison of Z boson peaks and widths for central-central and central-plug events.

the dashed line is excluded by the precision electroweak data and the dark shaded area in the right hand corner corresponds to $\Lambda_\pi > 10$ TeV.

Previous best experimental constraints from CDF are shown in Figure 1.7. These limits combine the dilepton and diphoton channels, using 200 pb^{-1} and 345 pb^{-1} of data respectively [27].

This analysis extends the search in the diphoton channel, using 1.2 fb^{-1} of data, through the inclusion of the two plug calorimeters, resulting in greater angular coverage. It is the first RS diphoton search in Run II to use these calorimeters.

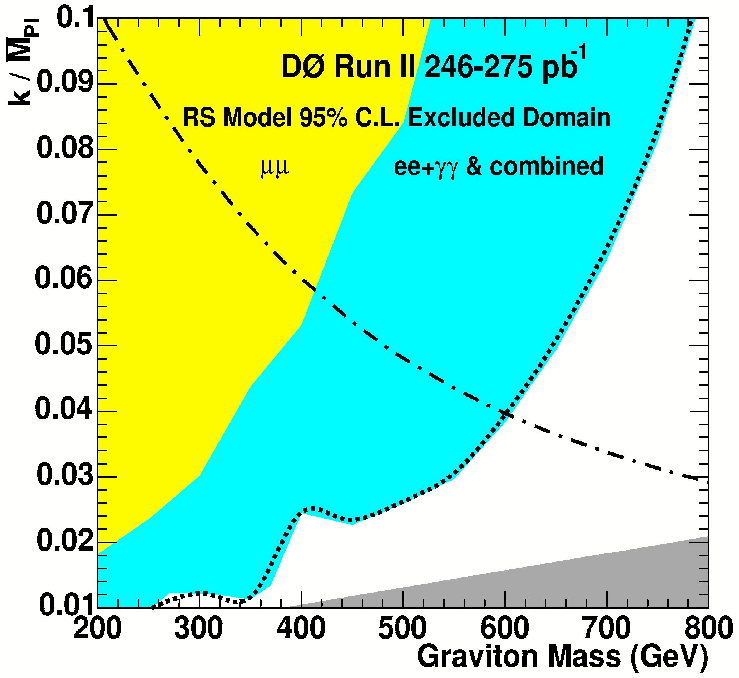

Figure 1.6: Excluded RS graviton mass region, as a function of $k/\overline{M}_{Pl}$. The dotted line shows the experimental limit using 246 pb^{-1} and 275 pb^{-1} of data, for the dimuon and diEM channels respectively, using the D0 detector. The area below the dashed line is excluded by the precision electroweak data and the dark shaded area in the right hand corner corresponds to $\Lambda_\pi > 10$ TeV [26].

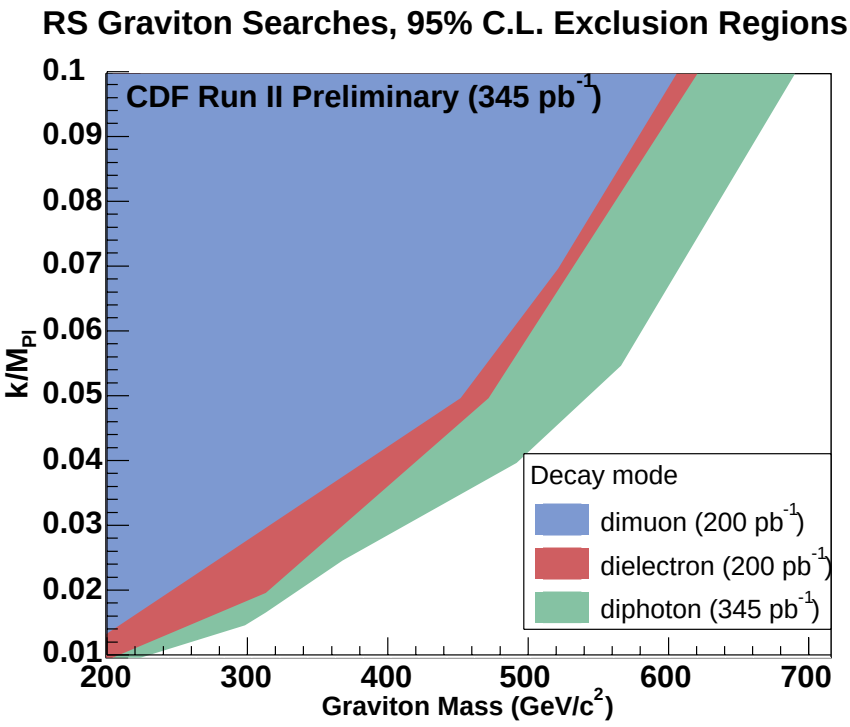

Figure 1.7: Excluded RS graviton mass region, as a function of $k/\overline{M}_{Pl}$, for the combined dilepton and diphoton channels at CDF using 200 pb^{-1} and 345 pb^{-1} of data, respectively [27].

Chapter 2

The Fermilab Accelerator and CDF Detector

The Fermi National Accelerator Laboratory (Fermilab), in Batavia, Illinois, is home to the Tevatron accelerator complex, shown schematically in Figure 2.1. It is currently the world's highest energy particle accelerator, accelerating protons (p) and antiprotons ($\bar{p}$) to energies of 0.98 TeV for a centre of mass energy ($\sqrt{s}$) of 1.96 TeV. It has two collision points, each with a general purpose detector; the Collider Detector at Fermilab (CDF) at one point and D0 at the other, to detect the secondary particles produced in the $p\bar{p}$ collisions, along with the $p\bar{p}$ remnants.

This chapter describes the components of the accelerator and the CDF detector used in this analysis.

2.1 The Tevatron Accelerator Chain

A series of accelerators are used to obtain the desired $p\bar{p}$ energies prior to injection into the Tevatron, a 0.98 TeV proton synchrotron. This acceleration

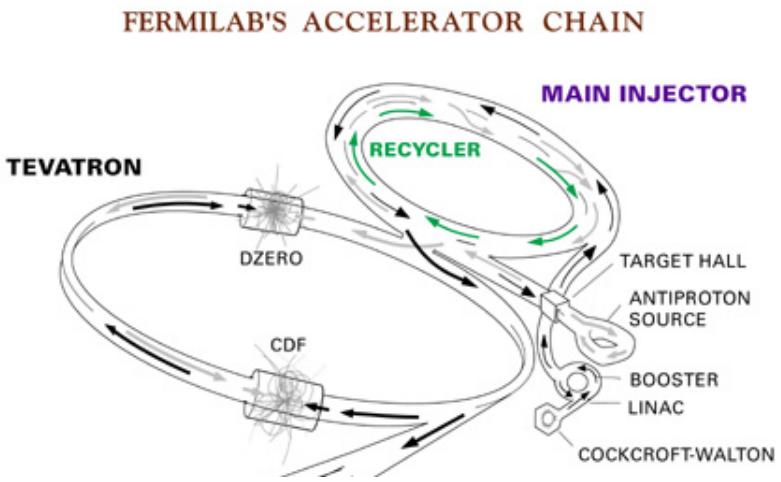

Figure 2.1: Schematic of the Fermilab accelerator complex.

process begins with the Cockroft-Walton pre-accelerator and is followed by the Linac, the Booster and the Main Injector. Antiprotons must also be produced to be sent to the Main Injector and finally the Tevatron, where they are focused into $p\bar{p}$ collisions in the Tevatron ring.
The following sections describe these stages in greater detail.

2.1.1 Proton Production

The protons are produced in the Cockroft-Walton pre-accelerator using a hydrogen gas source. The hydrogen molecules are ionized to produce negative ions (H^-) and are subsequently accelerated by a constant positive electric potential to 750 keV, from an initial energy of 25 keV. The H^- ions are then injected into the 150 m linear accelerator (LINAC) [28], where they are accelerated through a sequence of radio-frequency cavities, resulting in the particles being grouped in bunches, where an oscillating electromagnetic field boosts their energy to 400 MeV. The ions subsequently pass through a carbon foil, stripping off both electrons, leaving a beam of pure protons.

These protons are passed into the Booster, a synchrotron of diameter 150 m, located approximately 6 m below ground. Magnetic fields are used to bend the trajectory of the particles to a circular orbit, with protons traversing the Booster around 20,000 times, each pass increasing the energy through an applied electric potential. The magnetic field must be increased, as the protons are accelerated, to maintain the orbit. The beam is focused through the use of quadrupole magnets. In a period of 0.033 s the kinetic energy is raised from 400 MeV to 8 GeV.

The method of increasing the proton energy through short sections of electric potential results in stable regions of acceleration known as buckets. Here, protons are collected to form bunches, consisting of 6×10^{10} particles each, destined to be used in collisions or in antiproton generation.

2.1.2 The Main Injector

The Main Injector (MI), a synchrotron 3 km in circumference, is used for further proton acceleration, collection and storage and for antiproton production [29].

The Booster transfers seven bunches of protons at a time into the MI, where they are accelerated to an energy of 120 GeV and then to 150 GeV and are coalesced into a single bunch, consisting of approximately 6×10^{13} protons. This process is repeated 36 times, resulting in 36 proton bunches in the Tevatron.

The antiprotons are produced by randomly selecting protons which have reached 120 GeV and focusing them on to a nickel target, every 1.5 s. This produces, among many secondary particles, antiprotons. For every million protons which are collided only about 20 antiprotons are produced. A lithium lens is used to focus and align the secondary particles, which exit with a wide distribution of energies, peaking near 8 GeV. The antiprotons are subsequently selected using

pulsed dipole magnets acting as a charge-mass spectrometer [30]. To reduce the spread in energies, the antiprotons, which are bunched as a result of the protons leaving the Booster in bunches, are injected into a Debuncher accumulator ring. Their momentum is then decreased through stochastic cooling, also increasing their spatial distribution, so that they form a continuous beam. This beam must then be separated back into bunches to be compatible with the radio-frequency cavities used in the MI and Tevatron. This is achieved through stacking in the Accumulator, creating stacks of approximately 100×10^9 antiprotons with an energy of 8 GeV, which are then injected into the MI and coalesced into 4 bunches separated by 396 ns. They are then accelerated up to 150 GeV for injection into the Tevatron, where they accelerate in opposite directions to the previously injected protons. This is repeated so that 36 bunches of protons and 36 bunches of antiprotons (a store) are circulating in the Tevatron.

The MI tunnel also houses the Recycler, preventing antiprotons that are not used at the end of a store from being dumped (around 75%). They are collected and sent to the MI and to the Tevatron again, a process which approximately doubles the luminosity obtainable.

2.1.3 The Tevatron

The Tevatron, located approximately 10 m below ground, is a superconducting synchrotron composed of approximately 1000 superconducting dipole, quadrupole and sextupole magnets, cooled to 4 K to provide a magnetic field of 4.2 T. It is the final stage of acceleration and receives the 150 GeV protons and antiprotons (the 'shot'), accelerating them to 0.98 TeV in helical orbits. These intertwine with each other, the protons traveling clockwise and antiprotons traveling anticlockwise. Once the required energy is reached, the beams are

focused, using low beta quadrupole magnets (a 'low beta squeeze'), into collisions at two interaction points (D0 and B0, with B0's nominal interaction point being the Collider Detector at Fermilab (CDF)). This changes the helical orbit and reduces the transverse beam size, allowing collisions on average every 396 ns. The store is maintained for approximately 18 hrs, at which point beam decay and collisions reduce the luminosity sufficiently to warrant a new store.

2.1.4 Performance Parameters

The design of a detector must reflect the parameters which define the performance of the accelerator. These are summarized here for the CDF detector.

- Centre of mass energy of colliding particles ($\sqrt{s}$)
  With both particles in the same reference frame (the lab frame), this is given by E_1+E_2, where $E_{1/2}$ is the energy of the proton/antiproton. However, due to the composite nature of hadrons, with each parton carrying some fraction of the 980 GeV, x_i, the actual interaction energy is given by $\sqrt{\hat{s}} = \sqrt{s x_p x_{\bar{p}}}$. It is therefore $\sqrt{\hat{s}}$ that determines the highest mass of the secondary particles produced, the cross-sections and the event yields.

- Instantaneous luminosity
  Defined as $\mathcal{L} = f(n_p n_{\bar{p}})(4\pi\sigma_p\sigma_{\bar{p}})^{-1}$, where f is the frequency of bunch crossing, $n_{p/\bar{p}}$ is the number of protons/antiprotons per bunch and $\sigma_{p/\bar{p}}$ is the Gaussian transverse beam profile. The collision rate is obtained by multiplying the instantaneous luminosity by the inelastic cross-section for a $p\bar{p}$ interaction. To date, the highest value of $\mathcal{L}$ achieved at the Tevatron is 3×10^{32} cm^{-2}s^{-1} , achieved during the week starting January

1, 2007. $\mathcal{L}$ is integrated over the data taking period to find the integrated luminosity. To predict the number of events for a given process, $\int \mathcal{L}dt$ is multiplied by the cross-section for that process. Luminosity must be measured experimentally and is further discussed in Section 2.2.5.

- Bunch spacing

  Defined as $1/f$, this is the time between two bunch crossings at the collision point and determines the time limit for the detector to collect and store event data. The data acquisition system for the CDF detector, described in Section 2.2.6, is therefore designed for a bunch crossing rate of 396 ns.

2.2 Collider Detector at Fermilab

The Collider Detector at Fermilab (CDF) is a general purpose detector, consisting of many detector systems, designed to measure the energy, momentum and position of charged and neutral particles produced in the $p\bar{p}$ interactions. It is a forward-backward and azimuthally symmetric detector, shown in Figure 2.2, with the geometric centre located at the nominal interaction point of the collisions. Full technical details can be found in Reference [31].

It consists of tracking detectors, located around the beam pipe, a calorimetry system designed to measure particle energies and drift chambers, used for muon detection. These are described in detail in the following sections.
Data taking at CDF has been divided into periods to coincide with Tevatron operations, and several of the subdetectors are new to Run II, designed for the increased luminosity. The data taking periods and corresponding integrated luminosities are summarised in Table 2.1, with this analysis using Run II data taken between February 2002 and February 2006. The current total integrated luminosity (both delivered and recorded to tape) for Run II, at time of writing,

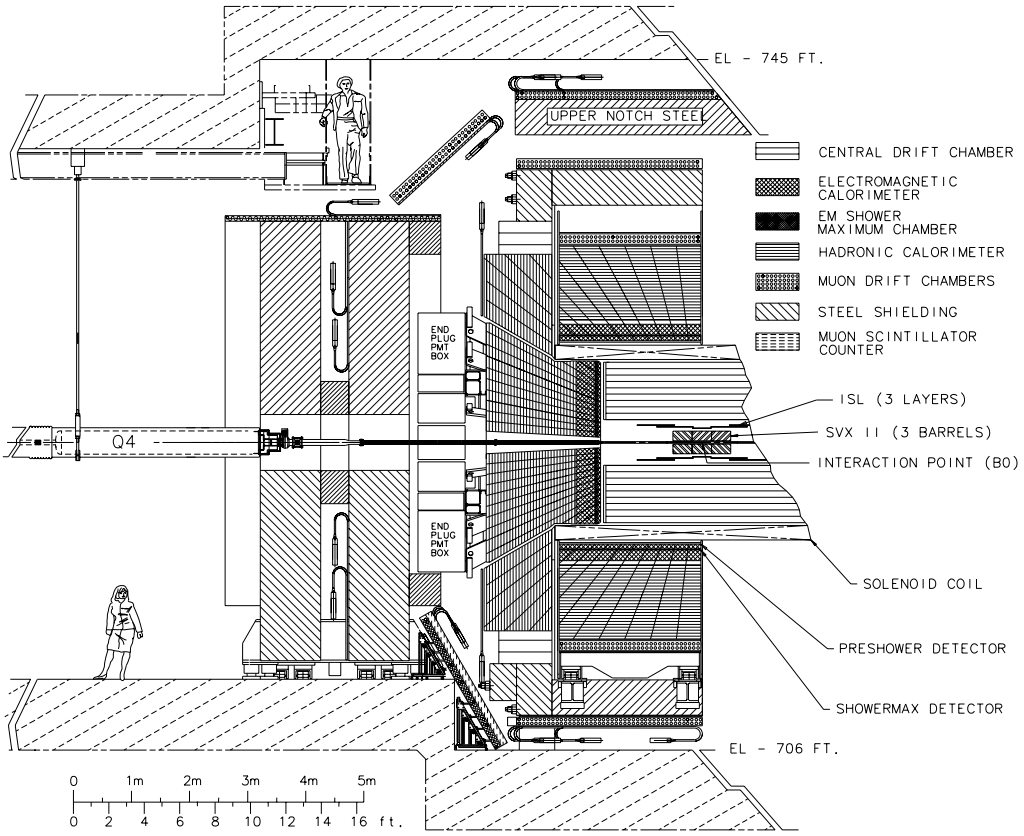

Figure 2.2: Longitudinal view of half of the CDF Run II detector.

is shown in Figure 2.3.

Run	**Year**	**Integrated Luminosity ($\mathbf{pb^{-1}}$)**
	1987	0.025
Run 0	1988-89	4.5
Run Ia	1992-93	19.4
Run Ib	1994-96	90.4
Run II	2001-ongoing	$>$ 2000 (see Figure 2.3)

Table 2.1: Summary of data taking periods at CDF.

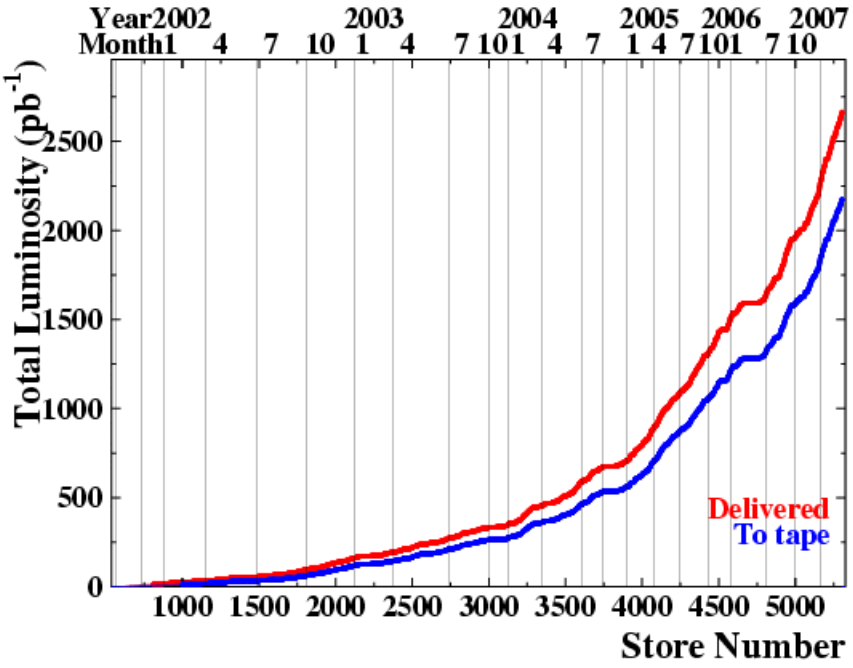

Figure 2.3: Current total integrated luminosity recorded at CDF for Run II.

2.2.1 Geometrical Coordinate System

A cylindrical system of coordinates is used, with the $+z$ direction defined by the direction of the proton beam and the origin at the centre of the detector. The r coordinate and azimuthal angle ϕ are orthogonal to this plane (lying in the transverse plane) and pass through the interaction point, as shown in Figure 2.4.

A cartesian system is also used with x and z lying in the transverse plane and the polar angle θ measured from the z axis. The two systems are related through:

$$z = r \cdot \cos\theta \tag{2.1}$$

Additionally, the rapidity (y) is also used, due to its invariance under Lorentz boosts. It is defined as:

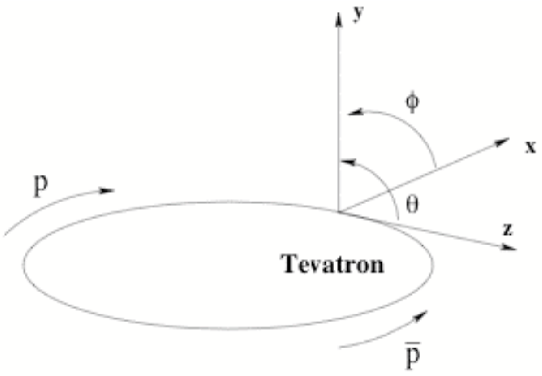

Figure 2.4: CDF coordinate system.

$$y = \frac{1}{2} \ln \frac{E + P_z}{E - P_z} \tag{2.2}$$

where P_z is the longitudinal momentum along the beamline and E is the energy. A massless approximation of this ($E \approx p$), the pseudorapidity, is defined as:

$$\eta = -\ln(\tan(\frac{\theta}{2})) \tag{2.3}$$

The detector η refers specifically to the location of a particle with respect to the centre of the detector, i.e. $z = 0$.

2.2.2 Tracking System

The tracking system is used to record the paths of the charged particles produced in an interaction and to measure their position and momentum. Its main components are the Silicon Vertex Detector (SVX II) [32] [33], providing tracking information out to $|\eta| < 2$, surrounded by the Central Outer Tracker (COT) [34], a new open cell drift chamber providing coverage out to $|\eta| < 1$. The integrated tracking system is shown in Figure 2.5 and provides a 50% increase in angular coverage compared to Run I. The entire tracking system

is contained within a superconducting solenoid, 1.5 m in radius and 5 m in length, providing a 1.4 T magnetic field parallel to the beamline. A charged particle then experiences a curved trajectory in the $r - \phi$ plane with a constant velocity in z, resulting in a helical path through the tracking volume. The transverse momentum is then obtained through the relation $p_T = 0.3B\rho$ GeV/c, where B is the magnetic field (in T) and ρ is the radius of curvature (in m).

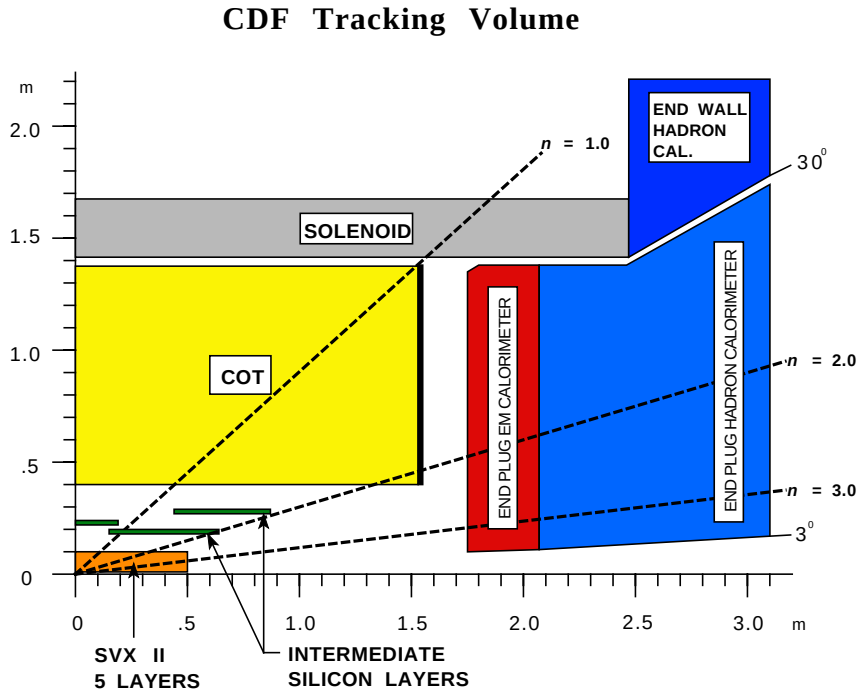

Figure 2.5: Longitudinal view of the CDF tracking system, representing one quadrant.

Silicon Tracking

The CDF silicon tracking system is the sub-detector closest to the interaction region and consists of three concentric silicon detectors. Its main purpose is to reconstruct tracks used for secondary vertex positioning from the production of long lived particles. To accomplish this, the tracker measures the position

and charge deposited by particles passing through the sensors. It is made up of three subcomponents, Layer 00, the Silicon Vertex Detector and the Intermediate Silicon Layers, shown from the $r-\phi$ and $r-z$ perspectives in Figure 2.6.

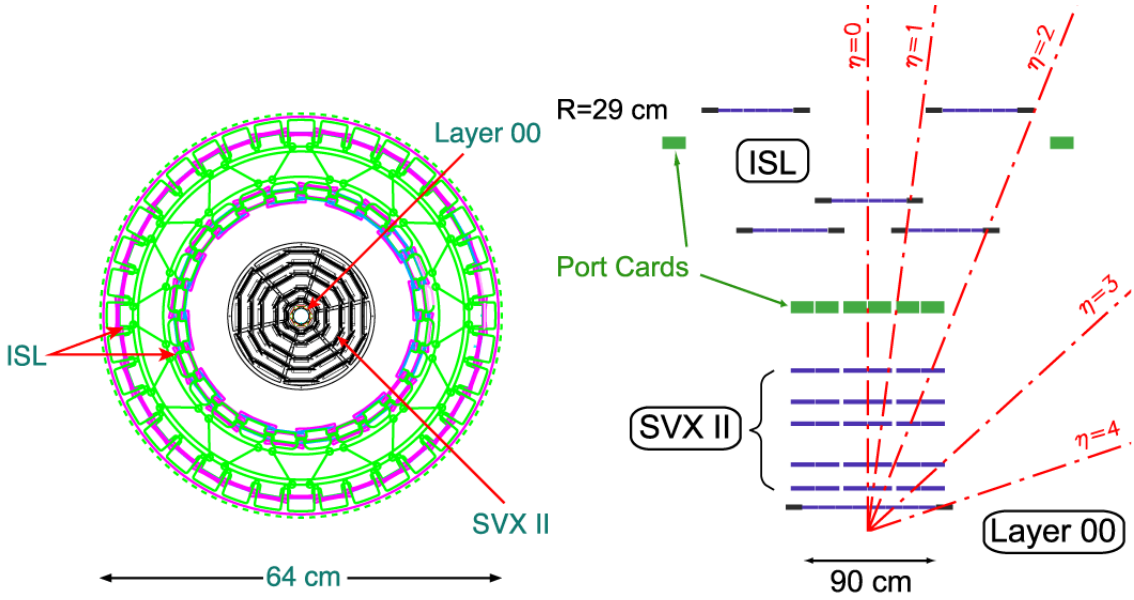

Figure 2.6: $r-\phi$ and $r-z$ perspectives of the silicon detector, showing all subcomponents. The port cards, located around the periphery of the barrel ends, decode the data and convert it from electrical to optical signals via optical interface modules.

An innermost, single sided silicon layer, Layer 00 (L00), is located at 1.35 cm radius, mounted onto the beampipe which is located between radii of 0.83 and 1.25 cm. Due to its proximity to the interaction point, it is radiation hard up to a delivered luminosity of 3 fb^{-1}. Consisting of 144 single sided silicon microstrip sensors, organised into modules with a '6 + 6' fold configuration, which are interleaved into a 12 sided pattern, as shown in Figure 2.7, it gives complete ϕ and z coverage extending to $\pm$78.4 mm from z. Both the sensors and the support structure for L00 were developed and constructed by the Liverpool High Energy Physics group.

The SVX II is located outside L00 and has an inner radius of 2.44 cm

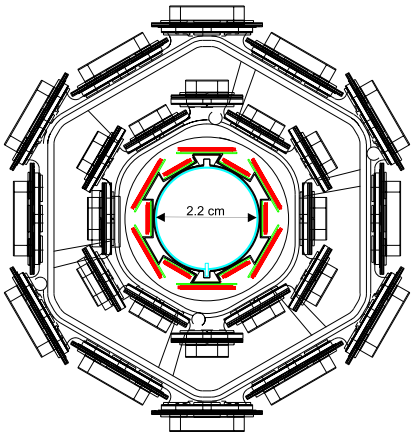

Figure 2.7: Endview of innermost three layers showing L00 along with first two layers of the SVX II region.

and outer radius of 10.7 cm. It is composed of three identical 29 cm long barrels, giving a combined length of 87 cm. Each barrel is further divided into 12 wedges in ϕ and is composed of five layers of double sided silicon microstrip detectors, see Figure 2.8, providing coverage of $-2 < \eta < 2$. Stereo angle information from the layers is combined to form a three dimensional helical track through combining the $r - \phi$ measurement from three layers on one side and a 90° stereo measurement on the other, with the further two layers combining the $r - \phi$ measurements on one side with a small stereo angle of 1.2° on the other.

The purpose of the Intermediate Silicon Layers (ISL) is to match the silicon tracks to tracks in the Central Outer Tracker (COT), with inner radius 43.4 cm. It consists double-sided silicon placed at a radius of 22 cm from the beam and provides coverage for $|\eta| < 1$ for the central region. In addition, for the plug region $1 < |\eta| < 2$, two additional layers at radii 20 and 28 cm provide tracking coverage where that from the COT is incomplete, as shown in Figure 2.9.

The three layers allow for standalone silicon tracking (reconstruction of three dimensional tracks independently of the COT) out to an $|\eta|$ of 2, using

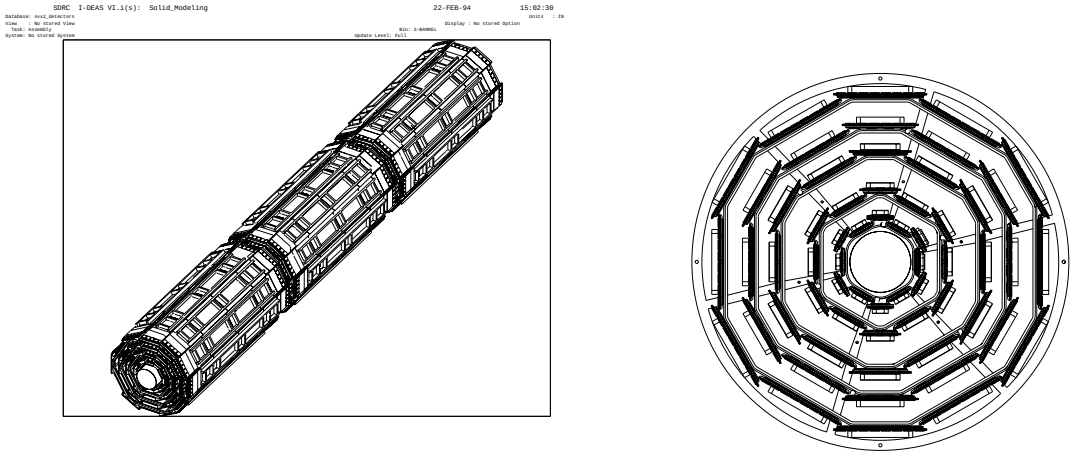

Figure 2.8: On the left, view of the three barrels of the SVX silicon detector. On the right, end view of one barrel showing the 12 wedges with the 5 layers.

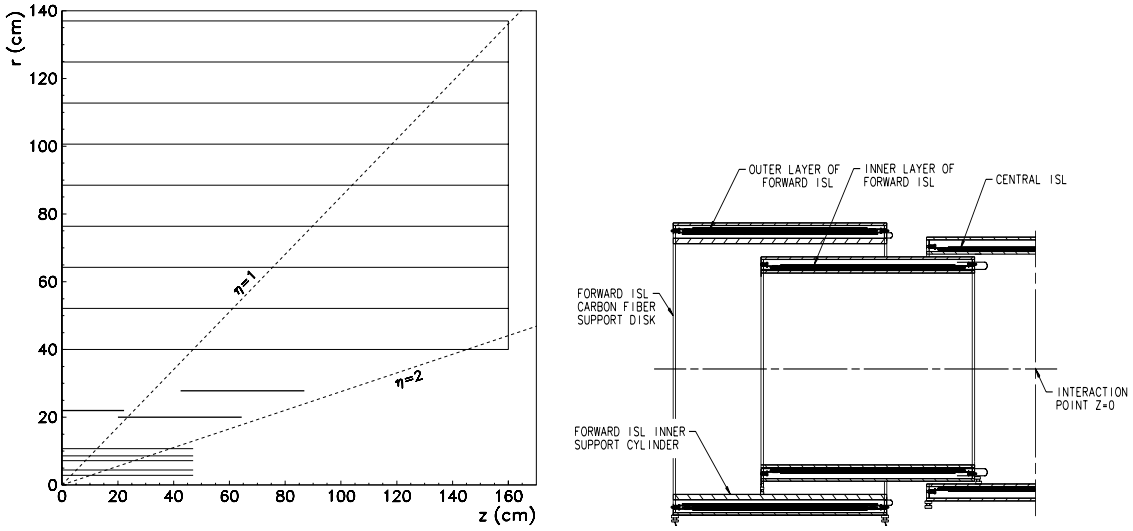

Figure 2.9: On the left, the $r - z$ view of the silicon detector layout and on the right a schematic view of the ISL, both showing the additional silicon layer for matching SVX and COT tracks and two layers providing tracking coverage out to $|\eta| < 2$.

the combined information of the SVX II and ISL. The design parameters of these sub-detectors are summarized in Table 2.2, where χ_0 indicates radiation

length.

SVX II	
Radial coverage	2.4 to 10.7 cm, staggered quadrants
Number of layers	5
Readout coordinates	$r-\phi$ on one side of all layers
Stereo side	$r-z$, $r-uv$, $r-z$, $r-uv$ ($uv \equiv 1.2°$stereo)
Resolution per measurement	12 μm (axial)
Total length	96.0 cm
Rapidity coverage	$\lvert\eta\rvert \leq 2.0$
Number of channels	405 504
Material thickness	3.5% χ_0
ISL	
Radial coverage	20 to 28 cm
Number of layers	one for $\lvert\eta\rvert \leq 1$; two for $1 < \lvert\eta\rvert < 2$
Resolution per measurement	16 μm (stereo)
Total length	174 cm
Rapidity coverage	$\lvert\eta\rvert \leq 1.9$
Number of channels	268 800
Material thickness	2% χ_0

Table 2.2: Design parameters of the tracking systems.

Central Outer Tracker

The Central Outer Tracker (COT), a 96 layer open-cell drift chamber, is used to measure the three-dimensional tracks in the region $|\eta| \leq 1.0$. Located at radii of 40 cm and 132 cm from the beampipe and inside the solenoid, it is composed of eight superlayers (SL), each containing 12 wire planes, with

30 240 gold plated tungsten sense wires in total. The eight superlayers are divided, alternately, into 4 axial layers (for $r-\phi$ measurements) and 4 stereo layers (for z measurements). Two aluminium endplates, of 1.4 m radius, are separated by 310 cm in z. Figure 2.10 shows a schematic of the axial and stereo superlayers. Each superlayer is then divided into cells by gold covered Mylar field sheets strung between the endplates. A 50:50 Argon-Ethane and isopropyl alcohol gas mixture fills the space between cells, giving a fast drift velocity (100 μm/ns) to work at high luminosities.

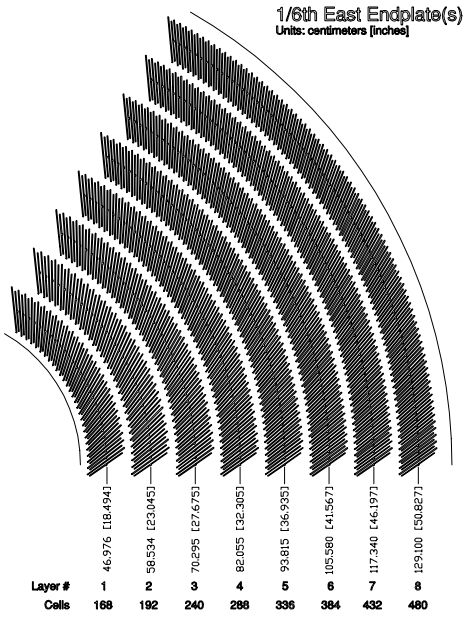

Figure 2.10: Schematic of the four axial (even) and four stereo (odd) superlayers.

Charged particles, traveling on a helical path through this gas, cause ionization, the freed electrons drifting to the sense wires and providing $r-\phi$ information on the position of the hits. Combining the hit information from the axial and stereo wires gives the z position, and the track momentum and charge can be determined through the track curvature. The momentum resolution, δp_T, is approximately $0.003 \cdot p_T^2$ GeV/c, therefore greater momentum

leads to poorer resolution as the reconstructed track becomes harder to measure.

A fully reconstructed track is defined by the following quantities, defined with respect to the track vertex (the track position closest to the z-axis, denoted z_0):

- The track curvature is given by $(2 \cdot r)^{-1}$, where r is the radius of the track. The curvature in the $x-y$ plane is positive with a counter-clockwise track and negative if clockwise.
- The impact parameter, d_0, is the distance between the track vertex and the z-axis in the transverse direction, with a resolution of 300 μm.
- To determine the event η, the cotangent of the track angle ($\cot\theta$) with the z-axis is used.
- The direction of the track at the track vertex in the $r-\phi$ plane is denoted ϕ_0.

A wide coverage and excellent momentum resolution mean that the COT is used as the primary tracker for event reconstruction and triggering. A summary of the properties of the COT are given in Table 2.3.

Time of Flight System

Located between the COT and the solenoid is the Time of Flight (TOF) detector [35]. It is composed of 216 scintillator bars, with dimensions $4 \times 4 \times 276$ cm, with a photomultiplier tube mounted at the end of each. It measures the length of time that a particle has taken to travel from the interaction point and is important in the tagging of cosmic ray events.

Radial coverage	44 to 132 cm
Number of superlayers	8
Stereo angle (°)	+3, 0, -3, 0, +3, 0, -3, 0
Layers per superlayer	12
Drift field	2.5 kV/cm
Maximum drift distance	0.88 cm
Maximum drift time	100 ns
Resolution per measurement	180μm
Rapidity coverage	$\|\eta\| < 1$
Number of channels	30 240
Material thickness	1.6% χ_0

Table 2.3: COT design parameters.

2.2.3 Calorimeters

The calorimeter modules are located outside the solenoid of the tracking systems and measure the amount of energy deposited by electrons, photons and jets, together with a position measurement provided by the segmented structure of the detector. The calorimetry system is divided into central ($|\eta| < 1.1$) and plug ($1.1 < |\eta| < 3.6$) regions, with an additional end wall hadronic calorimeter (WHA) to cover the region in between, as shown in Figure 2.5. Note that, due to cryogenic utilities required by the solenoid, the region $0.77 < \eta < 1.0$, $75^\circ < \phi < 90^\circ$ is uninstrumented. Each region is subdivided into electromagnetic (CEM, PEM) and hadronic sections (CHA, PHA), to distinguish energy deposited by electrons and photons from that deposited by jets, and is segmented into 15° in the azimuth and 0.1 in η, forming projective towers pointing back to the nominal interaction point, as shown in Figure 2.11. All calorimeters at CDF are based upon sandwiching scintillating (sampling) material between layers of heavy (absorbing) metal. The

absorbing material causes particles entering the calorimeter to shower (photons, electrons and positrons in the CEM and PEM and a shower of baryons, mesons and photons in the CHA and PHA). The sampling material then produces photons in response to these showers, whose intensity is measured by PMTs and is proportional to the number of particles produced in the shower (N). The intensity is therefore also dependent on the energy of the incident particle. The uncertainty on the number of particles in the shower (δN) is proportional to $\sqrt{N}$, giving the energy resolution of the calorimeter ($\delta E/E$) as proportional to $1/\sqrt{N}$ as $E \propto N$. The values for the resolution of the EM and hadronic calorimeters are given in Table 2.4.

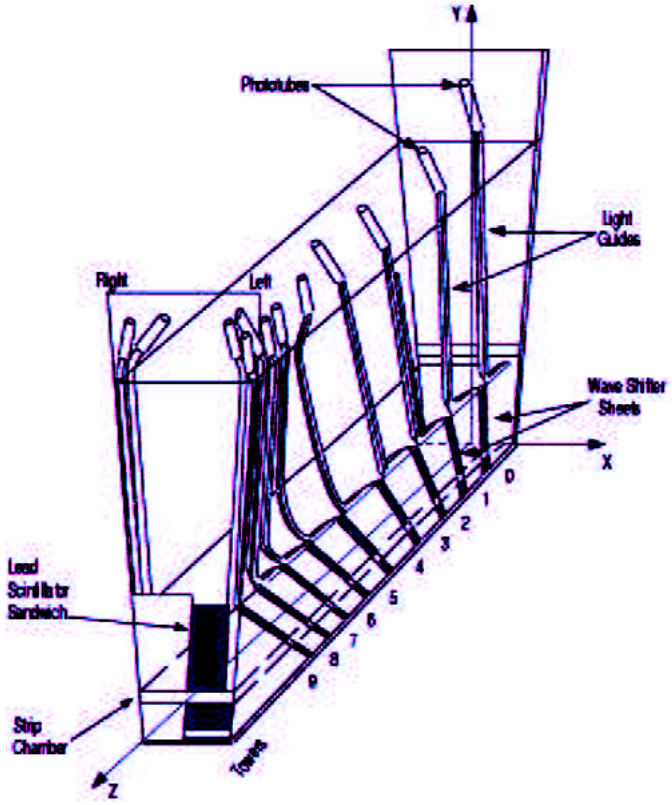

Figure 2.11: Schematic of a wedge of the central calorimeter, illustrating the towers pointing back to the interaction point.

Central Calorimeter

The central calorimeter is cylindrically symmetric about $\eta = 0$ and divided into two ('east' and 'west'), each part containing 24 wedges of 15° in ϕ. Each wedge is then divided into ten towers in η, labeled 0 - 9, giving full 2π azimuthal coverage.

The electromagnetic section (CEM) [36] extends outward from the beamline to a depth of 18 radiation lengths (χ_0). Thirty layers of 3.2 mm thick lead clad aluminium are interlaced with 31 layers of 5 mm thick polystyrene scintillator, as shown in Figure 2.11, giving a resolution $\delta E/E$ of $14\%/\sqrt{E}$. The energy resolution of a reconstructed photon in the central or plug EM calorimeter is described in Section 3.2.1. To improve the position information of the EM shower, the Central Electromagnetic Shower maximum (CES) [36] detector is embedded in the CEM at the shower maximum (approximately 6 χ_0, 184 cm from the beamline), the point at which showers have reached their maximum transverse extent and the energy is low enough that no further multiplication takes place.

The CES is a proportional chamber composed of orthogonal strips and wires and a drift gas mixture of 95% argon and 5% carbon dioxide. These give the 'local x' (the distance from the centre of the calorimeter in the $r-\phi$ direction) and 'local z' positions, which are used to help associate electromagnetic particles with their helical tracks, which are extrapolated to the CES. It also gives additional information on the shape of the EM shower, helping to distinguish single and multi-particle final states; final state photons from a π^0 decaying to two photons, for example.

The central hadronic calorimeter (CHA) [37] is located directly after the CEM and is retains the same wedge structure. A hadron shower, produced by the inelastic scattering of a incident hadron, may start in the CEM but will only be fully absorbed in the denser CHA. This is composed of 32 layers of 1.0 cm thick

acrylic scintillator sandwiched between sheets of 2.5 cm thick iron absorber, with a resolution $\delta E/E$ of $75\%/\sqrt{E}$. The endwall calorimeter is similarly composed, using 5.0 cm thick steel and covers the gap between $0.7 < |\eta| < 1.1$.
To further help particle identification, a second set of proportional chambers, the Central Preradiator Detector (CPR), is located between the CEM and the solenoid at a radius of 168 cm from the beampipe. Each chamber is 116 cm long, 37.3 cm wide and 2.85 cm deep and has 2.22 cm cells segmented in $r-\phi$. The solenoid and tracking detectors act as a radiator, helping to distinguish between prompt photons and electrons and those originating from π^0 decays and conversions.

Plug Calorimeter

The Plug calorimeter is completely new to Run II and is shown in Figure 2.12. It is composed of two parts; the Plug Electromagnetic Calorimeter (PEM) and Plug Hadronic Calorimeter (PHA). It has a similar construction to the central system. Details of the segmentation are displayed in Table 2.4.
The PEM [38] consists of 23 layers of 4.5 mm thick lead sheets interlaced with 4 mm thick polystyrene scintillator, out to 21 χ_0 and has resolution $\delta E/E$ of $16\%/\sqrt{E}$. The Plug Electromagnetic Shower (PES) detector [39] is embedded at 6 χ_0 and is divided into eight 45° sectors, ranging from 11 to 130 cm from the beampipe. The sectors are composed of two layers (U and V) of 5 mm pitch scintillator strips, aligned at $+22.5°$ and $-22.5°$ to the radial direction from the beamline. Combining the position information from the U and V layers provides a two-dimensional position measurement.
The PHA is made up of 22 layers of 5 cm thick iron absorber and 6 mm scintillator and extends out to a distance of 7 hadronic interaction lengths (λ_0). It has a resolution $\delta E/E$ of $80\%/\sqrt{E}$.

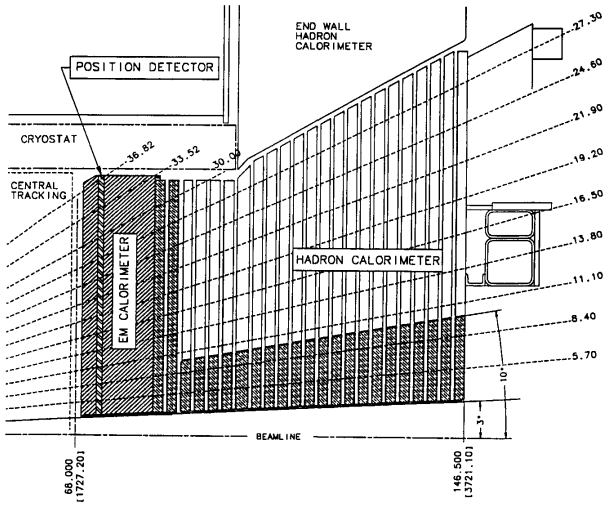

Figure 2.12: Schematic of one quadrant of the plug calorimeter.

Subdetector	CEM	CHA	WHA	PEM	PHA
Coverage	$\|\eta\| < 1.1$	$\|\eta\| < 0.9$	$0.7 < \|\eta\| < 1.3$	$1.1 < \|\eta\| < 3.6$	$1.1 < \|\eta\| < 3.6$
Modules	48	48	48	24	24
η towers per module	10	8	6	12	10
Layers	31	32	15	23	23
Material	Lead	Iron	Iron	Lead	Iron
Radiation length	18 χ_0	4.7 λ_0	4.5 λ_0	21 χ_0	7.0 λ_0
Fractional energy resolution ($\delta E/E$)	$14\%/\sqrt{E}$	$75\%/\sqrt{E}$	$75\%/\sqrt{E}$	$16\%/\sqrt{E}$	$80\%\sqrt{E}$

Table 2.4: Properties of Run II calorimeters.

2.2.4 Muon System

The muon system is located outside all other subdetectors and is composed of absorbers, scintillators and proportional chambers. It covers the region $|\eta| \leq 2.0$ and is divided into the Central Muon detector (CMU), the central Muon Upgrade detector (CMP) [40], the Central Muon Extension detector (CMX) [41] and the Intermediate Muon System (IMU). The coverage in η and ϕ is shown in Figure 2.13. The detectors are composed of single wire drift chambers, of which alternating layers are staggered, to provide more accurate

position information. Muon objects are created by matching hits in the muon chambers with a COT track, as a muon will leave an ionizing track but very little energy in the calorimeter.

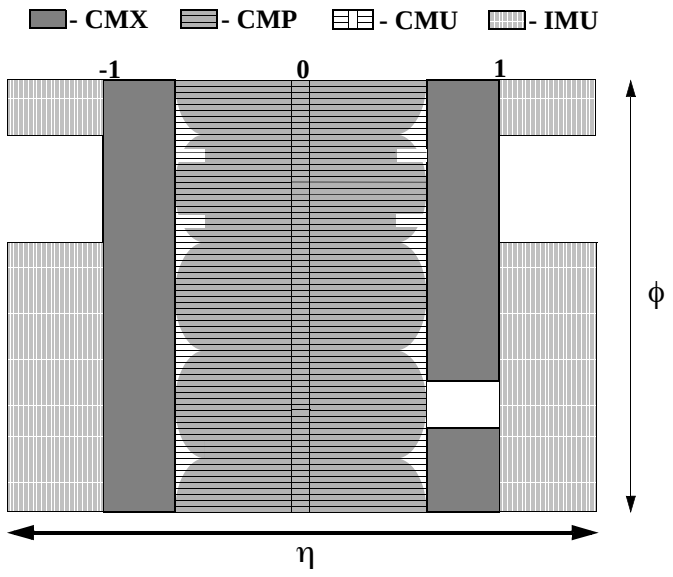

Figure 2.13: Muon system coverage in η and ϕ.

2.2.5 Luminosity

The instantaneous luminosity is experimentally determined using two gas Cherenkov Luminosity Counters (CLCs) [42], located between the beampipe and the plug calorimeters. They are made up of 48 thin conical gas-filled Cherenkov counters, arranged in three concentric circles consisting of 16 counters. They cover the region $3.7 < |\eta| < 4.7$ and measure the number of interactions per beam crossing. Previously defined as $\mathcal{L} = f(n_p n_{\bar{p}})(4\pi\sigma_p\sigma_{\bar{p}})^{-1}$, the instantaneous luminosity may be rewritten in terms of the interaction rate and the inelastic $p\bar{p}$ cross-section, as given in Equation 2.4, as the interaction rate is defined as $\mathcal{L}\times\ \sigma_{in}$, where σ_{in} is the inelastic $p\bar{p}$ scattering cross-section and is also equal to the frequency of bunch crossing times the average number of interactions

per beam crossing.

$$\mathcal{L} = \frac{f \times \mu}{\sigma_{in}} \tag{2.4}$$

Here f is the frequency of bunch crossing and μ is the average number of interactions per crossing, given by the CLC hit rate (~ 5). The average of the inelastic cross-sections as measured by CDF Run I and the E811 experiments is 60 ± 2.3 mb [43]. A 6% systematic uncertainty is assigned to the luminosity, coming equally from the CLC detector acceptance and the uncertainty on the total inelastic cross-section.

2.2.6 Trigger Systems and Data Acquisition

The Tevatron collision rate for Run II is approximately 7.6 MHz, while the rate that events can be written to tape is less than 75 Hz. A three-level minimal deadtime triggering system is therefore used to filter and synchronize the recording of events. It is designed to recognize events that are of interest among the minimum bias events which have activity at small angle to the beamline, satisfying the minimal trigger conditions, with the minimal amount of deadtime. It has a three level architecture, the Level 1 (L1) trigger reducing the rate from 7.6 MHz to 50 kHz, L2 to 300 Hz and L3 to the required 75 Hz. At each stage more event data are available and processed, with L3 fully reconstructing events. To compensate for increases in luminosity, dynamic prescaling is used. This prescales the triggers at high luminosity and removes the prescale when the luminosity drops. The prescale may be retained, if required, as the luminosity drops, by disabling it. The dataflow of the trigger system is illustrated in Figure 2.14.

Level-1

The initial decision about an event is made using hardware which is custom designed to find physics objects based on a subset of the detector information. These are found using three parallel synchronous processing streams, feeding input into a single Global L1 decision unit that is synchronized with the Tevatron master clock, whose period is 396 ns. A decision must be made by this time or the data are lost, translating to a decision time of 5.544 μs for the Global L1 Trigger. One stream is used for calorimeter data, finding electrons, photons and jets. A second stream, the eXtremely Fast Tracker (XFT) uses COT information to reconstruct tracks, which is then used by the third stream to match tracks to muon stubs, to trigger on muon candidates. Triggers can be formed using these streams singularly or combined using AND or OR combinations, for a total of 64 different possible triggers.

Level-2

Once an event has passed the L1 requirement, it is passed to the Level 2 (L2) trigger, where the data are written to one of four data buffers within the Data Acquisition (DAQ) electronics of each detector component. This differs from L1 in that the data are stored until a decision is made. It cannot be overwritten by a subsequent event. If a L1 accept occurs while all four buffers are occupied, deadtime is incurred. In order to minimize this deadtime, the time for a L2 decision must be less than approximately 80% of the time between L1 accepts. To achieve this, the L2 trigger is divided into two synchronous processes, each having a decision time of 10 μs. The L2 trigger uses all the data collected for L1, along with information from the CES and SVX II detectors, and is processed with higher granularity for improved particle resolution and identification. In addition, a jet reconstruction algorithm is applied using the improved resolution. Typical L2 accept rates during data taking vary from 100 to 300 Hz, depending on the instantaneous luminosity.

Level-3

The Level 3 (L3) trigger is composed of the Event Builder (EVB), used to assemble and package all information, and the L3 processing farm which uses full detector resolutions to fully reconstruct events. Once a L2 accept has been issued, the information is sent to the EVB where it is packaged, together with digital information from each detector, which is aligned based on the bunch counter to ensure information from different bunch crossings is not mixed. These event fragments are then received by 16 subfarms which compose the L3 farm. Complete events are then built using the full detector information and improved resolution unavailable at L1 and L2. The designed latency for the L3 trigger is a second, so full event reconstruction can take place. A trigger decision is then made based on this detailed information. The accept rate is based on the rate at which data can be written to tape, approximately 75 Hz.

2.2.7 Data Processing

Events that have successfully passed the L3 trigger are then processed using the CDF Offline reconstruction. This creates detector objects, such as calorimeter clusters, for each subdetector by applying calibration data to the raw subdetector data. These objects are then associated, using a customized software framework, to form physics objects such as photons, electrons etc., which are then written to magnetic tape for permanent storage.

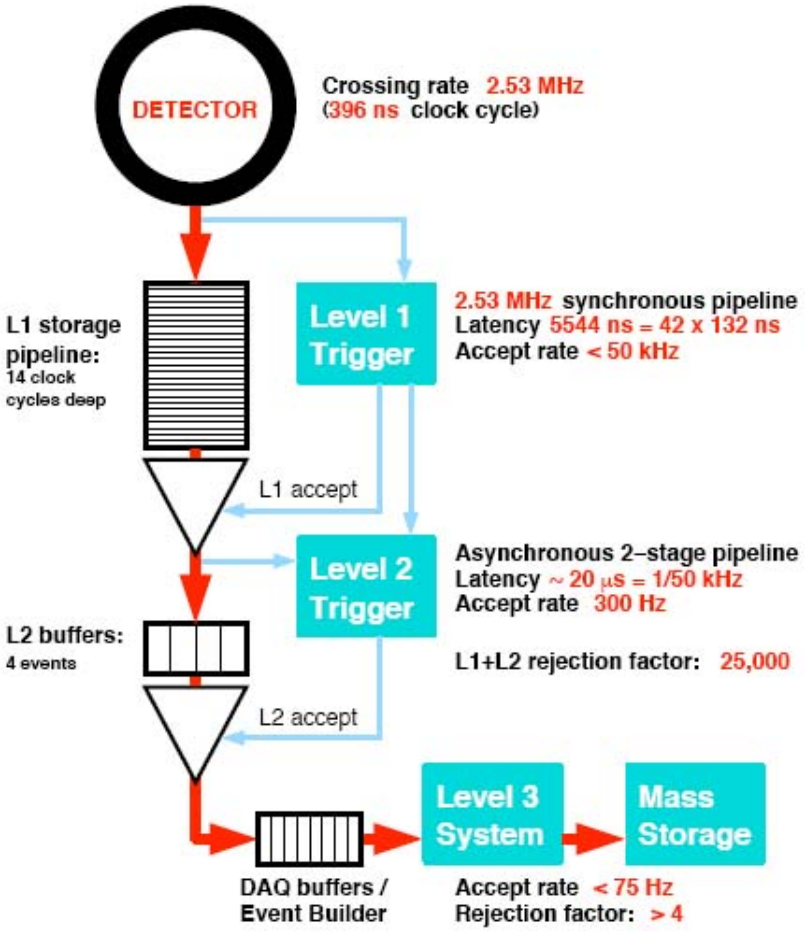

Figure 2.14: Dataflow diagram of the CDF three-level trigger system.

2.3 Detector Simulation

To understand the collision data obtained, the expected properties of physics processes occuring within the CDF detector must first be understood. This is done in two stages. The first stage is 'generation', in which events and cross-sections are generated using a Monte Carlo program. The kinematics for a given process, $p\bar{p} \rightarrow \gamma\gamma$ for example, are then reproduced for a given incoming proton/antiproton energy. The second stage is 'simulation', simulating particle behaviour within the detector and the resolution of the detector components.

This is done using CDFSim, a GEANT-based simulation [44] of the full detector, which includes many different physics concepts, such as bremsstrahlung, to accurately describe particle behaviour. This simulated data are then analyzed with the same code as the collision data to ensure the detector response is well understood. Corrections may need to be applied where the simulation does not perfectly model the data. Theses are described in Section 3.2.3.

Chapter 3

Data Sample and Event Selection

Events matching the $\gamma\gamma$ final state are selected from the collision data using high transverse energy (E_T) photon and diphoton triggers, to select events containing photon candidates. In addition to the main data sample used in this analysis, a further sample is required for the study of the performance of the detector simulation, as described in Section 5.2.1. This is done using a $Z \rightarrow ee$ sample, triggered using the central high-p_T electron trigger. Triggered events are then analysed using the offline reconstruction, generating physics objects from the detector data and allowing selection of photon and electron candidates.

The details of the photon and electron triggers used, event reconstruction and event selection are discussed in the following sections.

3.1 Triggers

To filter events containing a photon or electron pair final state from other interactions, several trigger paths are chosen, each based on the three-tier

trigger system, as described in Section 2.2.6. The requirements of each path are described in the following sections.

3.1.1 Photon Trigger

The dataset for this analysis is collected using the diphoton triggers DIPHOTON_12 and DIPHOTON_18 [45]. In addition, the high-E_T single photon triggers ULTRA_PHOTON_50 and SUPER_PHOTON_70 [45] are used, as the analogue-to-digital conversion boards which digitize the calorimeter phototube signals to form the L1 and L2 tower E_T for trigger decisions saturate at an energy of 128 GeV for both the electromagnetic and hadronic calorimeters. The DIPHOTON triggers may therefore be inefficient for high E_T photons. The triggers specifically designed for high-E_T photons, which have no E_{had}/E_{em} requirement at high-E_T, are added to ensure full efficiency.
The requirements at each level are described below and summarised in Tables 3.1 and 3.2.

DIPHOTON_12

- **Level 1:** The E_T of an EM cluster, as defined in section 3.2.1, is required to be above 8 GeV, with the z vertex set to zero. The ratio of the hadronic to electromagnetic energy (E_{had}/E_{em}) must be < 0.125, unless the EM cluster has $E_T > 14$ GeV.

- **Level 2:** At L2 the trigger requires two EM clusters, each with $E_T >$ 10 GeV and $E_{had}/E_{em} < 0.125$. The isolation energy must be < 3 GeV, or the ratio to the EM cluster E_T must be less than 15%.

- **Level 3:** The L3 filter requires two EM objects with EM $E_T > 12$ GeV with a $\chi^2 < 20$, as described in Section 3.4.2, for a central cluster. Additionally, a sliding E_{had}/E_{em} requirement is imposed: $E_{had}/E_{em} <$

$0.055 + 0.00045 \times E/GeV$, as the EM shower length increases with increasing energy. This is removed above 200 GeV.

DIPHOTON_18

The DIPHOTON_18 trigger imposes the same trigger requirements as DIPHOTON_12, differing only at L2 where the EM cluster E_T must be > 16 GeV and L3 where the cluster $E_T > 18$ GeV.

ULTRA_PHOTON_50

- Level 1: As for DIPHOTON_12 and DIPHOTON_18.
- Level 2: An EM calorimeter cluster with $E_T > 40$ GeV is required, with $E_{had}/E_{em} < 0.125$.
- Level 3: The EM cluster must have $E_T > 50$ GeV, with a E_{had}/E_{em} requirement of < 0.125, which is removed at 200 GeV.

SUPER_PHOTON_70 EM and JET

- Level 1: As for DIPHOTON_12 and DIPHOTON_18 for the EM trigger. A single tower EM+Hadronic $E_T > 10$ GeV is required by the jet trigger.
- Level 2: A cluster E_T of > 70 GeV is required by the EM trigger and jet $E_T > 90$ GeV by the jet trigger.
- Level 3: Additionally, at L3, a sliding E_{had}/E_{em} requirement is imposed: $E_{had}/E_{em} < 0.2 + 0.001 \times E/GeV$, which is removed above 100 GeV.

‘

DIPHOTON_12	
L1	Single tower $E_T > 8$ GeV ($z = 0$) Single tower $E_{had}/E_{em} < 0.125$ unless $E_T > 14$ GeV
L2	$E_T > 10$ GeV ($z = 0$) $E_{had}/E_{em} < 0.125$ Calorimeter Isolation < 3.0 GeV or 15% Two photons required
L3	$E_T > 12$ GeV ($z = 0$) E_{had}/E_{em} sliding, removed at 200 GeV $\chi^2 < 20$ (if CEM) Two photons required
DIPHOTON_18	
L1	Single tower $E_T > 8$ GeV ($z = 0$) Single tower $E_{had}/E_{em} < 0.125$ unless $E_T > 14$ GeV
L2	$E_T > 16$ GeV ($z = 0$) $E_{had}/E_{em} < 0.125$ Two photons required
L3	$E_T > 18$ GeV ($z = 0$) E_{had}/E_{em} sliding, removed at 200 GeV $\chi^2 < 20$ (if CEM) Two photons required

Table 3.1: DIPHOTON_12 and DIPHOTON_18 trigger requirements.

3.1.2 Electron Trigger

The $Z \rightarrow ee$ data sample, required for the Monte Carlo behaviour study, requires a central electron to pass the high transverse momentum electron ELECTRON_CENTRAL_18 trigger, with the trigger path as follows:

ULTRA_PHOTON_50	
L1	Single tower EM $E_T > 8$ GeV ($z = 0$) Single tower $E_{had}/E_{em} < 0.125$ unless $E_T > 14$ GeV
L2	$E_T > 40$ GeV ($z = 0$) $E_{had}/E_{em} < 0.125$
L3	$E_T > 50$ GeV ($z = 0$) $E_{had}/E_{em} < 0.125$, removed at 200 GeV
SUPER_PHOTON_70 EM	
L1	Single tower EM $E_T > 8$ GeV ($z = 0$) Single tower $E_{had}/E_{em} < 0.125$ unless $E_T > 14$ GeV
L2	$E_T > 70$ GeV ($z = 0$)
L3	$E_T > 70$ GeV ($z = 0$) $E_{had}/E_{em} < 0.2 + 0.001 \cdot E$, removed at 100 GeV
SUPER_PHOTON_70 JET	
L1	Single tower EM+Had $E_T > 10$ GeV ($z = 0$)
L2	Jet $E_T > 90$ GeV ($z = 0$)
L3	EM $E_T > 70$ GeV ($z = 0$) $E_{had}/E_{em} < 0.2 + 0.001 \cdot E$, removed at 100 GeV

Table 3.2: ULTRA_PHOTON_50 and SUPER_PHOTON_70 trigger requirements.

- Level 1: A central EM cluster with $E_T > 8$ GeV, associated with a track from the eXtremely Fast Tracker (XFT), is required. The XFT track must have $p_T > 8$ GeV/c and at least 10 (or 11) hits in at least 3 (or 4) layers. Clusters with $E_T < 14$ GeV are also required to have $E_{had}/E_{em} < 0.125$.

- Level 2: The cluster E_T must be > 16 GeV with an XFT track pointing at the seed tower and $E_{had}/E_{em} < 0.125$.

- Level 3: A calorimeter cluster with $E_T > 18$ GeV must be associated with a COT track with $p_T > 9$ GeV/c and $E_{had}/E_{em} < 0.125$. Additionally, for all data taken after January 2003, it is required that $L_{shr} < 0.4$ and $|\Delta Z| < 8$ cm (these variables are defined in Sections 3.4.2 and 3.4.3), whilst the E_{had}/E_{em} is calculated using 3 hadronic towers as opposed to only 2.

The ELECTRON_CENTRAL_18 trigger is summarised in Table 3.3.

ELECTRON_CENTRAL_18	
L1	CEM cluster, $E_T > 8$ GeV and XFT track, $p_T > 8$ GeV/c ($E_{had}/E_{em} < 0.125$ for $E_T < 14$ GeV)
L2	CEM cluster, $E_T > 16$ GeV and XFT track, $p_T > 8$ GeV/c
L3	CEM cluster, $E_T > 18$ GeV and COT track, $p_T > 9$ GeV/c ($E_{had}/E_{em} < 0.125$)

Table 3.3: ELECTRON_CENTRAL_18 trigger requirements.

3.2 Event Reconstruction

An offline, object-oriented, event reconstruction program processes and calibrates all recorded events, forming the physics objects used for particle identification. Examples of these include electromagnetic (EM) clusters, tracks and jets. This section gives details of the reconstruction modules used in the selection and analysis of $\gamma\gamma$ final state events and $Z \rightarrow ee$ events used in the data/Monte Carlo comparison study (see Section 5.2.1).

3.2.1 Calorimeter Clustering

Photons and electrons are reconstructed through EM clustering and the creation of a 'CdfEmObject', matching the cluster with other detector objects such as tracks and pre-radiator clusters, to optimize particle identification [46].

Electromagnetic Clustering

EM clusters are formed from seed towers, defined as towers with $E_T > 3$ GeV, which are sorted by E_T with the event vertex set to $z = 0$. A single calorimeter tower, with a coverage of 0.1 in η and 15° in ϕ, as described in Section 2.2.3, will rarely contain all energy deposited by a particle. The highest energy 'seed' tower is then clustered with the adjacent towers, 'shoulder' towers, which are towers adjacent in η with a non-zero energy, are then added to the seed tower. They must be located within the same wedge in ϕ and in the same detector as the seed tower, i.e. CEM seed towers may only have CEM shoulder towers associated with them, and similarly for the PEM. To remove the possibility of assigning a tower to more than one cluster, shoulder towers are removed from the seed tower list and both are marked as 'used'. Clusters formed in this way have an energy resolution of $1.7\% + \frac{13.5\%}{\sqrt{E}}$ in the CEM and $1\% + \frac{16\%}{\sqrt{E}}$ in the PEM, with a typical size of 0.2 in η and 15° in ϕ for both central and plug regions.

The clustering technique used for the central and plug regions varies slightly, due to the differing subdetector geometry. Within the CEM, a shoulder tower must neighbour the seed tower in η and be located within the same half of the detector; east or west. It is then added to the cluster if it has an E_T greater than 100 MeV. A central cluster can then consist of, at most, three towers. Should the seed tower be the innermost or outermost tower in the wedge, the cluster can have at most two towers.

Plug EM clustering uses a 'brute force', BF_PEM Clustering, method. Towers

sharing a border or corner with the seed tower are considered neighbouring towers. Of the eight then possible neighbour towers, that with the maximum E_T, the 'daughter' tower, is clustered to the seed tower if it has an EM E_T greater than 100 MeV. The towers then bordering the seed and daughter are searched for a pair of towers with E_T greater than 100 MeV. Those with the highest E_T are added, giving a 2×2 tower structure. It is, however, also possible to have a 3×3 PEM cluster.

Electromagnetic Objects

Once an EM cluster has been formed, a CdfEMObject is created to construct a photon or electron, collectively known as EM objects, by matching detector objects to the EM cluster. Those used for photon and electron candidate identification in this analysis are discussed below.

Shower maximum clustering: a precision measurement of a particle's position is obtained through matching an EM cluster to its shower maximum cluster. This also allows for multi-particle discrimination. As the shower maximum response to a particle is usually spread across several channels, they are grouped into CEM and PEM clusters. Within a wedge and for a given view, channels above threshold are matched to surrounding channels above shoulder threshold, with a total width of 11 in the CES and 9 in the PES. The CES cluster position is measured in z and ϕ coordinates, with the views perpendicular. The PES uses x and y coordinates with the view at 45°. Once the cluster has been formed the shower shape profile is matched to single particle test beam data and the cluster centroid is used as the EM cluster position for the given view. The clusters are reconstructed with a position resolution of 1 mm.

Track reconstruction: high precision track reconstruction is required for the identification of EM objects in the offline reconstruction. Objects in the

central region use hit-based, unseeded tracks, using COT data only (COT tracks), while plug objects require a seeded algorithm, reconstructing tracks in the SVX, as they only cross a small section of the COT (Phoenix tracks). These algorithms are discussed in further detail below, with additional details on track requirements given in Table 3.4, where the variable z_0 is the COT only beam constrained z coordinate of the track (i.e. it must extrapolate back to the beamline), at the point of closest approach to the beam, and ΔR indicates a cone in $\eta - \phi$ space defined as $\Delta R = \sqrt{\Delta\phi^2 + \Delta\eta^2}$.

- COT Tracking

  The central track reconstruction algorithm forms 3-dimensional charged-particle tracks [47]. The hit position and timing information within each axial superlayer (SL) of the COT are used to group hits together into segments, forming 2-dimensional tracks in the $r - \phi$ view. Hits within a SL may be shared by two segments during the segment building process, but only the segment with the greater number of total hits retains a shared hit after processing is complete. A histogramming algorithm is then run to create additional segments that may have been missed through the initial method. This is then repeated in the stereo layers, the segments providing the z information to form the 3-dimensional tracks. Should the case arise that no stereo hits are found after the stereo linking, individual hits in the stereo layers may be added to the track to provide z information, should enough be successfully linked. Once the axial and stereo information has been added together, the tracks have complete p_T and 3-dimensional orientation information. The track p_T has a resolution of $\sigma(p_T) = 0.15\% \cdot p_T^2$ GeV/c and tracking reconstruction efficiency, measured using central electron W events which have been triggered without a track requirement, of 99.3%.

- Phoenix Tracking

  The Phoenix tracking algorithm, (so called as it 'resurrects' tracks from their constituent parts in the various sub-detectors), is specifically designed for high-p_T plug EM objects [48] [49]. It looks for a COT resolved event vertex and an EM calorimeter cluster. The cluster position, as determined by the shower-max detector and its associated E_T, together with the event vertex, define two points from which two paths are constructed allowing for positive and negative charge. The SVX is then scanned along these paths for hits to obtain a high-precision track. As the algorithm is seeded by the PEM cluster, the cluster resolution dominates the tracking resolution. The efficiency, measured with $Z \rightarrow ee$ events, is found to be 83.2 ± 1.0 %.

	Variable	Cut
COT	Good Super Layer	≥ 7 hits
	N_{goodSL}^{axial}	≥ 3
	N_{goodSL}^{stereo}	≥ 3
	Variable	Cut
Phoenix	$\|z_0\|$	≤ 60.0 cm
	N_{svx}^{hits}	≥ 3
	ΔR (track, PES)	≤ 3

Table 3.4: Offline track reconstruction.

3.2.2 Event Vertex Reconstruction

Events with a well defined high-p_T lepton use the track to set the location of the interaction. In the event of multiple leptons, the highest p_T lepton track is

used. In the case where there are no well reconstructed lepton tracks, a COT track based vertex algorithm is used to determine the point of hard scattering in the collision. The z_0 position of the tracks are extrapolated out to the beam spot and the tracks grouped together accordingly. The weighted average of tracks that have been grouped together in this way is then used to calculate the vertex location. If multiple vertices are present, that with the highest sum of associated track p_Ts is chosen as the event vertex.

3.2.3 Detector Calibration

To ensure event reconstruction is independent of time and detector geometry, as subdetector responses change slowly during operation, calibrations are carried out during the offline processing. A low background, tightly selected control sample is used to derive the correction factors, details of which are given below.

Central Electromagnetic Calorimeter Response

The central EM calorimeter response must be determined and corrected for to enable accurate measurement of photon and electron energy. Three main effects must be corrected for; x and z position-dependent variations, time-dependent tower-to-tower variations and overall scaling.

- **Position-dependent variations:** the position-dependent response across the face of the wedge, due to the decrease of the calorimeter response as a shower approaches an edge, is compensated for using 'face corrections', extracted from 1994 test beam data [50]. These are applied to both simulation and data. It also takes into account the effect of the attenuation of light passing through the scintillator and light loss in the wavelength shifting fibres. Once the face corrections are applied, a 7% variation in $\langle E/P \rangle$ as a function of the CES local x position (CES-x) is still seen,

where $\langle E/P \rangle$ is the average value of E/P in the range $0.9 \leq E/P \leq 1.1$, E is the calorimeter energy and P the momentum of the COT track associated with the CEM cluster. The following correction is applied to the CEM energy to obtain a flat distribution:

$$E_T^{corr} = \frac{1.015}{1 + 0.000157 \cdot x^2} \times E_T \tag{3.1}$$

where the x position is measured by the CES.

- **Time-dependent variations:** tower-to-tower gain variations, where gains are defined as the $\langle E/P \rangle$ per tower in the range 0.8-1.25, are corrected for using calibrated electrons spanning the full data sample. The correction gives a measured average E/P of unity, resulting in a 5% improvement in the energy resolution. This is applied to data only, as the simulated tower response is uniform over time.

- **Absolute energy scale:** a pure sample of central $Z \rightarrow ee$ candidates are used to calibrate the CEM absolute energy scale, as the Z mass has been accurately determined. The data, fitted to a Gaussian distribution, is tuned such that it is in accordance with a mass of 91.18 GeV/c^2.

Plug Electromagnetic Calorimeter Response

The PEM uses both a face response and a time-dependent correction.

- **Face response:** a 57 GeV positron beam [51], scanned across the face of a wedge, was used to obtain the correction factor. As the towers vary in size within the wedge, this is determined per tower, and then applied across all ϕ regions.

- **Time-dependent variations:** a time-dependent degradation in energy measurements is seen over the period of data taking, which is corrected

for using online calibrations. An absolute energy scale correction must be used in conjunction with this, matching $Z \rightarrow ee$ events with one plug electron to the correct Z mass distribution. This is done over three time periods [52].

Curvature Correction

Misreconstructed COT hits, arising from a misalignment within the COT, cause a bias in the E/P distribution as a function of ϕ. The correction in Equation 3.2 is applied, where Q is the charge of the track, p_T the beam constrained transverse momentum and ϕ the azimuthal angle of the track [53].

$$\frac{Q}{p_T^{corr}} = \frac{Q}{p_T} - 0.00037 - 0.00110 \times \sin(\phi + 0.28) \tag{3.2}$$

A flat distribution in ϕ is then obtained.

3.3 Additional Energy Corrections

Events containing one central electron with a beam-constrained, COT-only track and one plug electron are used to find the optimum method for reconstructing the plug electron energy, and subsequently obtain the energy scale factors required for the mass spectrum to peak at 91 GeV/c^2. They are required to have an invariant mass in the range $70 < M_{ee} < 110$ GeV/c^2, the resulting spectrum being fitted with a Gaussian in the range $86 < M_{ee} < 98$ GeV/c^2.

The energy is reconstructed through adding the 2×2 PEM cluster energy, after face corrections are applied (see Section 3.2.3), to the energy from the Plug Pre-Radiator (PPR). This is composed of a layer of scintillator tiles, placed in front of the PEM, which give improved particle identification in the plug. It is read out separately and must therefore be included for a complete measure-

ment of the energy. A leakage correction factor is then applied, as the fraction of the electron's energy which is outside the 2×2 cluster is dependent on the position of the centre of the electron's shower. An electron whose shower centre is near the edges of the cluster has a higher leakage energy fraction than one which has a shower centre in the middle of the cluster. The plug electron energy and E_T are thus defined as:

$$E^{EM} = E^{EM}_{2\times2}(face_corrected) + E^{PPR} + leakage_correction \quad (3.3)$$

$$E^{EM}_T = E^{EM} \cdot \sin(\theta_{PES}) \quad (3.4)$$

where the PES is used to provide all angular information.
The scale factors are subsequently found using the following formulae, so that the mass peak is located at 91 GeV/c^2:

$$E^{CEM}_{scale} = \frac{91}{M_{CC}} \quad (3.5)$$

$$E^{PEM}_{scale} = (\frac{91}{M_{CP}})^2 \times \frac{1}{E^{CEM}_{scale}} \quad (3.6)$$

where M_{CC} denotes the invariant mass of two electrons reconstructed in the central region, and M_{CP} the mass where one electron is reconstructed in the central region and one in the plug.
In data, a difference in energy scales is found between the east and west plugs. Consequently, separate scale factors are derived for each region. This discrepancy is not present in simulation, so a combined scale factor is given for Monte Carlo. The η and ϕ dependence of the mean of the mass distribution and widths show that at $\eta < 1.8$ the data are systematically lower than the Monte Carlo. To account for this, two scale factors are used, corresponding to an η

position of $\eta < 1.78$ and $\eta > 1.78$. This is used rather than 1.8 as it corresponds to the tower edge boundary. The scale factors obtained are given below in Tables 3.5 and 3.6, together with the invariant mass distributions once the scale factors have been applied.

	Calorimeter	Scale Factor
$\eta < 1.78$	CEM	-
	PEM east	1.020
	PEM west	1.015
$\eta > 1.78$	CEM	-
	PEM east	1.010
	PEM west	1.007

Table 3.5: Scale factors as applied to data.

	Calorimeter	Scale Factor
$\eta < 1.78$	CEM	0.996
	PEM	0.996
$\eta > 1.78$	CEM	0.996
	PEM	0.998

Table 3.6: Scale factors as applied to Monte Carlo.

3.4 Event Selection

Once events have been processed with the offline reconstruction software, photon and electron candidates are selected. Global cuts are applied to all data samples satisfying the trigger requirements, ensuring optimum data quality.

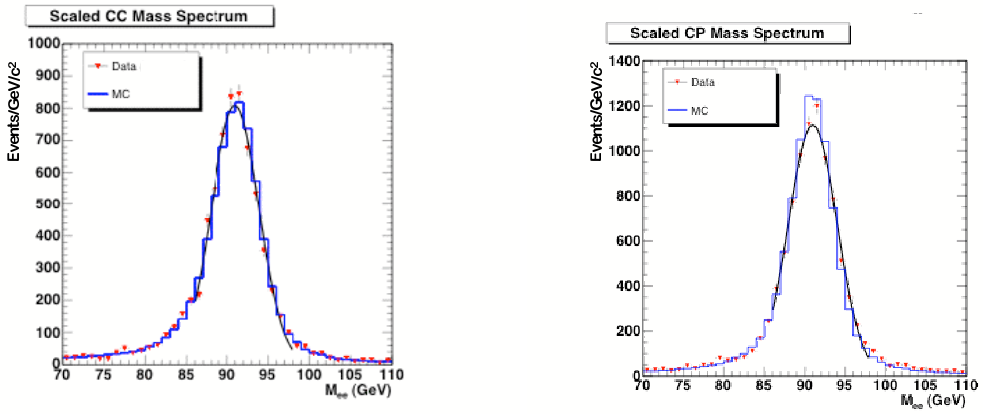

Figure 3.1: $Z \rightarrow ee$ invariant mass distribution, plotted in bins of 1 GeV/c^2, for central-central and central-plug dielectron candidates, with energy scale factors applied to data and Monte Carlo. The data are fitted to a Gaussian distribution in the range 86 GeV/c^2 < M_{ee} < 98 GeV/c^2.

Selection cuts are then made to identify photon and electron candidates in the central (CEM) and plug (PEM) regions of the detector. Both the CEM and PEM photon and electron identification variables are defined below, together with the applied cuts.

3.4.1 Global Event Selection

Good Run List

The operational status of each detector component is recorded through its assignment of a binary bit in a database, which can be set to 1(good) or 0(bad). To ensure optimum quality, all data are required to be marked 'good' for the calorimeter, the COT and the showermax systems, prior to applying selection cuts to photon and electron candidate identification variables. The silicon system is also required to be marked good for all electron candidates and for plug photon candidates, due to the use of plug tracking. Data taken during a period in which COT operations were not optimal were included in the photon data sample, but good silicon performance is required during this

period.

The integrated luminosities of the individual channels (to within a systematic error of 6%, see Section 2.2.5), once 'good runs' have been selected, are given in Table 3.7.

Data Sample	Trigger Path	$\mathcal{L}$ (pb^{-1})
Central Photon	DIPHOTON_12/ 18, ULTRA_PHOTON_50, SUPER_PHOTON_70	1115
Plug Photon	DIPHOTON_12/ 18, ULTRA_PHOTON_50, SUPER_PHOTON_70	1070
Electron (all)	ELECTRON_CENTRAL_18	683

Table 3.7: Integrated luminosity ($\mathcal{L}$) for central and plug photon and electron data samples, showing the L3 trigger paths used.

Good Vertex

To select events consistent with a beam-beam interaction, the primary vertex of the event, as defined above in Section 3.2.2, must lie less than 60 cm away from the centre of the detector:

$$|z_{vertex}| < 60 \text{ cm} \tag{3.7}$$

where $|z_{vertex}|$ is the position of the reconstructed vertex of the object in the event, with the highest p_T track associated with it. A requirement is also made on vertex quality, to reduce the possibility of misreconstruction from minimum bias backgrounds (non-single-diffractive events). The quality is assigned according to the number of tracks within 3σ in z, to differentiate between Silicon Standalone and COT defined tracks. Here, a vertex must have more than one COT track within 3σ, known as a class 12 vertex.

3.4.2 Photon Identification and Event Selection

Final state events with two photons are selected using the standard CDF baseline analysis cuts for high-p_T photons. The selection cuts are applied to the photon identification variables described below, and are displayed in Tables 3.8 and 3.9. The χ^2 selection cut has been loosened from the standard $\chi^2 < 20$ to $\chi^2 < 50$ for $E_T > 50$ GeV, due to a strong E_T dependence seen in Monte Carlo in the central χ^2 efficiency, as described in Section 5.1.1. Silicon Standalone tracking is used for plug track rejection, as opposed to Phoenix tracking used in electron selection, as this is required to measure the selection cut efficiency in $Z \rightarrow ee$ data for data/Monte Carlo comparison, as described fully is Section 5.2.1.

Due to the lower efficiency of tracking in the plug, events are required to have one photon in the central region and a second in either the central or plug region. In the case of events where more than two photons pass the selection cuts, the two highest E_T photons are selected.

In addition to the standard selection cuts, both photons are required to have an $E_T > 15$ GeV and an invariant mass ($M_{\gamma\gamma}$) > 30 GeV.

Central Variables

- CES Fiducial

  The fiducial, or well instrumented, region of the detector is defined in terms of the CES shower local coordinates. Photon EM clusters are required to be located within this area to maximise the resolution of the selection variables. The local x position is measured using the CES wires and is required to be within $|x_{CES}| < 21$ cm of the tower centre in the $r - \phi$ view, removing the poorly instrumented regions at the calorimeter wedge boundaries. The local z position is measured using the strips and must lie in the region 9 cm $< |z_{CES}| < 230$ cm, thereby excluding the

division between the east and west barrels of the central calorimeter and tower 9, the outside of the outermost central tower, where energy leakage is high.

- E_T

  Photon E_T is the total two-tower electromagnetic energy associated with the EM cluster, in the transverse direction, determined from the z_0 of the track associated with the maximum E_T central electron in the event.

- E_{had}/E_{em}

  E_{had}/E_{em} is defined as the ratio of the total energy deposited in the hadronic calorimeter to that in the electromagnetic calorimeter, for the towers included in the EM cluster. Photons deposit the majority of their energy in the electromagnetic calorimeter, leaving a minimal amount to be deposited in the hadronic calorimeter. Therefore the ratio is required to be < 0.125 for a photon candidate, rejecting hadronic jets which mainly deposit energy in the hadronic calorimeter. The requirements for a photon candidate are also met if it passes a sliding cut of $E_{had}/E_{em} < 0.055 + 0.00045 \cdot E$. This compensates for energy leakage in the hadronic calorimeter as energy increases, maintaining photon identification efficiency.

- Isolation

  Isolation requirements are used to suppress backgrounds, such as jets, which deposit energy near the EM cluster in the calorimeter. A cone of radius 0.4 ($\Delta R = \sqrt{\Delta\phi^2 + \Delta\eta^2} < 0.4$) is constructed around the EM cluster seed position. The isolation energy is then defined as the total transverse electromagnetic and hadronic energy within the cone, excluding the 1-3 cluster towers. It is corrected for energy leakage into neighbouring towers in η [54] and for additional energy from the un-

derlying event by using a sliding cut, as the underlying E_T in the event grows as the collision becomes more energetic. Backgrounds are removed by placing a requirement on the energy contained within the cone. For photons with $E_T < 20$ ($E_T > 20$), it is required that the isolation energy (Iso) satisfy the condition $Iso < 0.1$ ($Iso < 2.0 + 0.02 \cdot (E_T - 20.0)$) GeV.

- CES χ^2

  The observed lateral shower shape in the CES from test beam studies, in the strip (z) and wire ($r - \phi$) view, is compared to that from a photon candidate, to distinguish prompt photons from the decay products of other particles, e.g. $\pi^0 \rightarrow \gamma\gamma$, which produce two energy clusters. A χ^2 measurement is made between the data and test beam for both strip and wire views, with a cut being made on the average of the two measurements: $(\chi^2_{wire} + \chi^2_{strip})/2 < 20$ if $E_T < 50$ GeV and < 50 if $E_T > 50$ GeV .

- N tracks and track p_T

  To distinguish photons from electrons, the number of COT tracks leading to the EM cluster must be ≤ 1. If a track exists it must have $p_T < 1 + 0.005 \cdot E_T$ GeV/c.

- Track Isolation (cone 0.4)

  Tracks located near an EM cluster indicate that it originates from a jet. The track isolation places a restriction on the p_T of all tracks with z_0 5 cm from the event vertex in a cone of 0.4 around the EM cluster centroid. The track isolation must be $< 2 + 0.005 \cdot E_T$ GeV for a photon, where the scaling ensures a flat efficiency as a function of E_T.

- 2nd CES cluster

  To remove background from neutral mesons decaying to two photons, which produce two separate CES clusters, a cut is placed on the energy of

the second highest strip or wire CES cluster matched to the EM cluster, multiplied by $\sin\theta$ to ensure that the amount of material traversed by the photon is accounted for. The maximum energy allowed is $(0.14 \times E_T)$ GeV for $E_T < 18$ GeV, or $(2.4 + 0.01 \times E_T)$ GeV for $E_T > 18$ GeV.

Plug Variables:

Several additional identification variables are used for the plug region [55].

- Fiducial

  The detector η of the electromagnetic shower, as measured by the PES, is required to lie in the range $1.2 < |\eta| < 2.8$, to ensure optimum data quality.

- PEM χ^2_{3x3}

  The energy distribution, in a 3×3 block of calorimeter towers around the seed tower, is fitted to electron test beam data, and the χ^2 of this fit is used to measure the agreement.

- PES 5x9

  An EM cluster is composed of 9 strips within the PES, the seed strip having the highest energy. To discriminate between prompt photons and neutral meson decays, the energy in the middle 5 strips is divided by the energy in all 9 and must be > 0.65.

The invariant mass distributions for central-central and central-plug diphoton events, once all selection criteria have been applied, are shown in Figure 3.2, with bin widths comparable to the mass resolution. There are 11 088 central-central events and 20 933 central-plug events. Figure 3.3 shows this distribution for both channels combined. Most Z bosons that decay to e^+e^- are

Variable	Cut
Fiducial	Ces $\|x\| < 21$ cm, $9 <$ Ces $\|z\| < 230$ cm
E_{had}/E_{em}	< 0.125 or $< 0.055 + 0.00045 \cdot E$
Isolation E_T (Cone 0.4)	$E_T < 20$: $< 0.1 \cdot E_T$ GeV
	$E_T > 20$: $< 2.0 + 0.02 \cdot (E_T - 20.0)$ GeV
χ^2 (Strips + Wires)/2.0	< 20 if $E_T < 50$ GeV or < 50 if $E_T > 50$ GeV
N track (N3d)	≤ 1
Track p_T	$< 1 + 0.005 \cdot E_T$ GeV/c
Track Isolation (Cone 0.4)	$< 2.0 + 0.005 \cdot E_T$ GeV
2nd CES Cluser $E \cdot \sin\theta$	$E_T < 18$: $< 0.14 \cdot E_T$ GeV
	$E_T > 18$:$< 2.4 + 0.01 \cdot E_T$ GeV

Table 3.8: Central photon candidate selection criteria.

Variable	Cut
Fiducial	$1.2 < \|\eta\| < 2.8$
E_{had}/E_{em}	< 0.05 for $E \leq 100$ GeV
	$< 0.05 + 0.026 \cdot \ln(E/100)$ for $E > 100$ GeV
Isolation E_T (Cone 0.4)	$< 0.1 \cdot E_T$ GeV for $E_T < 20$ GeV
	$< 2.0 + 0.02 \cdot (E_T$ - 20.0) GeV for $E_T > 20$
PEM χ^2	< 10
PES 5×9	> 0.65
Track Isolation (Cone 0.4)	$< 2.0 + 0.005 \cdot E_T$ GeV

Table 3.9: Plug photon candidate selection criteria.

rejected by asking for no associated track, however approximately 1% remains in the central-plug sample as a mass peak below the search region, visible in the invariant mass spectrum at $\sim$ 91 GeV/c^2.

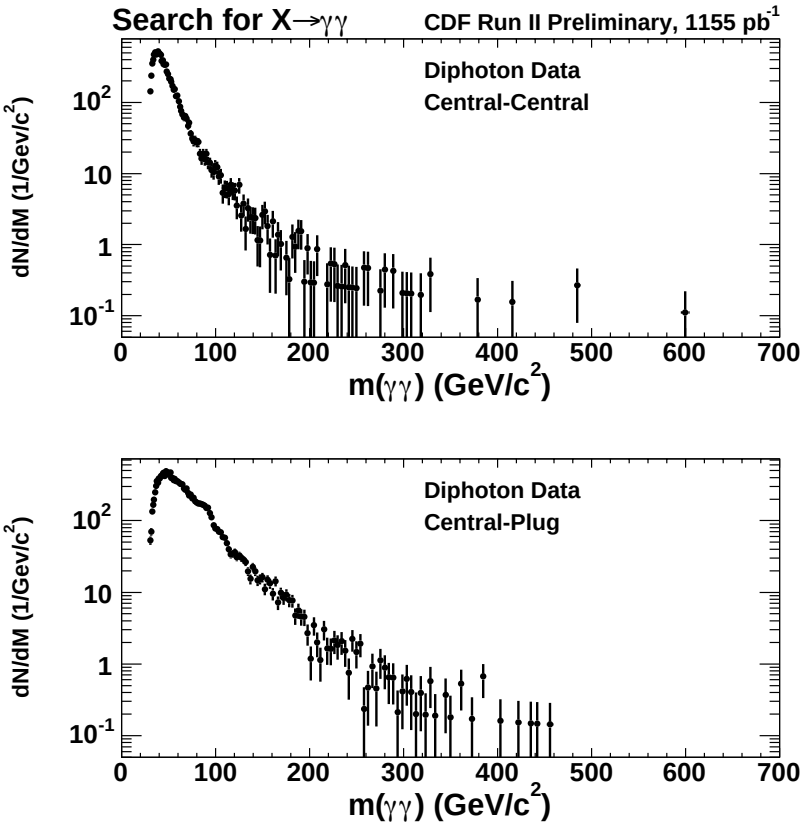

Figure 3.2: Invariant mass distribution for central-central (top) and central-plug (bottom) events after all selection criteria are applied, with bin widths comparable to the mass resolution.

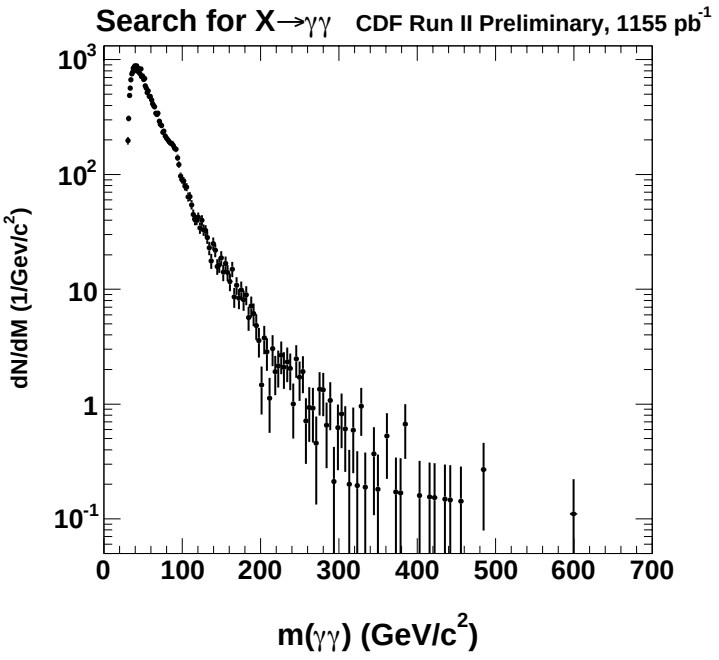

Figure 3.3: Invariant mass distribution after all selection criteria are applied, for central and plug channels combined, with bin widths comparable to the mass resolution.

3.4.3 Electron Identification and Event Selection

Electrons behave similarly to photons in the calorimeter, and are therefore identified using many of the same variables, with modified selection cuts. For example, the number of associated tracks to the EM cluster must be ≤ 2, rather than ≤ 1, as is the case for photons. Modified photon selection criteria are used rather than the standard electron cuts, as this sample is used for the data/Monte Carlo comparison for photon variable scale factors. Variables used exclusively for electron selection are described below, with Tables 3.10 and 3.11 showing the selection cuts required for an electron candidate.

Central and Plug Variables

- E_T

  Electron E_T is determined using the angle θ between the beam axis and the maximum-p_T COT track.

- E/P

  The energy momentum ratio is used to ensure that a 'good' electron is selected, where an E/P of $0.9 < \text{E/P} < 1.1$ is required. A larger ratio indicates that the track momentum has decreased due to Bremsstrahlung, however the photon energy is still contained within the EM cluster energy. An electron that has undergone Bremsstrahlung may give a poor χ^2 value due to the deviation in the shower shape. A smaller ratio indicates that some measured energy has been lost, due to cracks in the calorimeter.

- L_{shr}

  L_{shr} is another variable that helps differentiate EM clusters formed by hadronic jets from those resulting from electrons and is used in the CENTRAL_ELECTRON_18 trigger. The lateral shower profile is a measure

of the lateral sharing of energy across adjacent towers. It is, in a sense, an isolation cut. It is defined as:

$$L_{shr} = 0.14 \cdot \sum_i \frac{E_i^{adj} - E_i^{exp}}{\sqrt{(0.14)^2 \cdot E + (\Delta E_i^{exp})^2}} \tag{3.8}$$

where E_i^{adj} is the amount of energy measured in a tower adjacent to, and within, the same wedge as the seed tower, E_i^{exp} is the expected energy, from test beam data, deposited in that tower, E is the total EM energy of the cluster and ΔE_i^{exp} is the uncertainty on E_i^{exp}. The CES is seeded using the track associated with the EM cluster and the sum is over 3 towers.

- $|\Delta Z|$

  Also used by the trigger at L3, $|\Delta Z|$ is the distance between the track and CES shower z coordinate and is required to be < 8 cm.

Variable	Cut
Fiducial	CES $\|x\| < 21.0$cm
	CES $9.0 < \|z\| < 230.0$cm
E_T	>15 GeV
E/P	> 0.9 and < 1.1
E_{had}/E_{em}	$< 0.055 + 0.00045 \cdot E$
Isolation E_T	$< 0.1 \cdot E_T$ GeV if $E_T < 20$ GeV
	$< 2.0 + 0.02 \cdot (E_T - 20.0)$ GeV if $E_T < 20$ GeV
χ^2	< 20
N3d	≤ 2
Second highest p_T track	$< 1 + 0.005 \cdot E_T$ GeV/c
Sum track p_T (cone 0.4) - highest track p_T	$< 2.0 + 0.005 \cdot E_T$ GeV/c
Second CES cluster E (strip + wire) $\cdot \sin\theta$	$< 0.14 \cdot E_T$ GeV if $E_T < 18$ GeV
	$< 2.4 + 0.01 \cdot E_T$ GeV if $E_T > 18$ GeV

Table 3.10: Central electron candidate selection criteria.

Variable	Cut
PES Fiducial	$1.2 < \|\eta\| < 2.8$
E_T	>15 GeV
Phoenix hits	$\geq$3
E_{had}/E_{em}	< 0.05 if $E \leq 100$
	$< 0.05 + 0.026 \cdot \ln(E/100)$
Isolation E_T	$< 0.1 \cdot E_T$ GeV if $E_T < 20.0$ GeV
	$< 2.0 + 0.02 \cdot (E_T - 20.0)$ GeV if $E_T \geq 20.0$ GeV
$\chi^2_{3\times3}$	< 10
5×9 U and V	> 0.65
Sum track p_T (cone 0.4) - highest track p_T	$< 2.0 + 0.005 \cdot E_T$ GeV/c

Table 3.11: Plug electron candidate selection criteria.

Chapter 4

Signal Acceptance

The probability of a diphoton event passing the identification selection must be known accurately, in order to predict the expected number of signal events. This probability is dependent on the product of the acceptance and efficiency, where the acceptance takes the geometric and kinematic effects into account, and is determined using $G \rightarrow \gamma\gamma$ Monte Carlo, while the efficiency comes from the probability that an event containing two photon candidates will pass the online trigger, measured using data, and that the photon candidates will subsequently pass the identification cuts described in Section 3.4.2. This identification efficiency is also measured using Monte Carlo and is corrected for variations between data and detector simulation using $Z \rightarrow ee$ events, as described in Section 5.2.1. The predicted number of events, given by the cross-section times the integrated luminosity, is then scaled by the product of the acceptance and efficiency, as shown in Equation 4.1.

$$N^{G\rightarrow\gamma\gamma}_{predicted} = A \cdot \epsilon^{corr}_{trigger\times id} \cdot \int \mathcal{L} \cdot \sigma \tag{4.1}$$

In this chapter, the acceptance, together with its associated systematic uncertainties, are presented. The efficiencies are presented in Chapter 5.

4.1 Acceptance for $G \rightarrow \gamma\gamma$ events

The acceptance (A) is presented as a function of graviton mass for $G \rightarrow \gamma\gamma$ events, generated using *HERWIG* Monte Carlo, with 10 000 events generated for each mass point in the range 200 GeV/c^2 to 1050 GeV/c^2, at increments of 50 GeV/c^2. It is defined as the fraction of events passing geometric and kinematic requirements, in addition to the global selection cuts :

$$A = \frac{N_{recon}}{N_{gen}} \tag{4.2}$$

where N_{recon} is the number of events passing these additional requirements and N_{gen} is the number of events passing the global selection cut of $|z_{vtx}| <$ 60 cm only (the good run list requirement need not be taken into account here, as only simulation is used). The kinematic and geometric requirements are included in the photon candidate selection cuts given in Section 3.4.2, and are summarized below.

The geometric, or fiducial, cuts require the photon EM clusters be located in well-instrumented regions of the detector. Two photons are required in the central region (CC events), or one in the central region and one in the plug (CP events). Due to the lower efficiency of tracking in the plug region, as described in Section 3.2.1, a poor signal to background ratio and a very low acceptance, events with two photons reconstructed in the plug are not considered here. A central photon candidate must be within 21 cm of the centre of a calorimeter tower in the $r - \phi$ plane and lie in the region 9 cm $< |z| <$ 230 cm, where $|z|$ is the z-coordinate measured by the CES. A plug photon candidate must have a seed tower which lies in the region $1.2 < |\eta| < 2.8$, to exclude edge effects. The kinematic requirement on each photon candidate is $E_T > 15$ GeV. The reconstructed invariant mass of the diphoton pair is then required to be greater than 30 GeV/c^2.

Table 4.1 and Figure 4.1 show the signal acceptance as a function of graviton mass for CC events, CP events and total acceptance (the addition of the CC and CP channels), together with the statistical errors.

$M_G(GeV/c^2)$	Acceptance (CC)	Acceptance (CP)	Total Acceptance (CC + CP)
200	0.221 ± 0.004	0.317 ± 0.005	0.538 ± 0.005
250	0.262 ± 0.004	0.291 ± 0.005	0.553 ± 0.005
300	0.307 ± 0.005	0.263 ± 0.004	0.569 ± 0.005
350	0.361 ± 0.005	0.223 ± 0.004	0.585 ± 0.005
400	0.382 ± 0.005	0.197 ± 0.004	0.580 ± 0.005
450	0.417 ± 0.005	0.171 ± 0.004	0.588 ± 0.005
500	0.427 ± 0.005	0.153 ± 0.004	0.580 ± 0.005
550	0.456 ± 0.005	0.137 ± 0.003	0.593 ± 0.005
600	0.467 ± 0.005	0.125 ± 0.003	0.591 ± 0.005
650	0.485 ± 0.005	0.112 ± 0.003	0.597 ± 0.005
700	0.490 ± 0.005	0.101 ± 0.003	0.591 ± 0.005
750	0.500 ± 0.005	0.095 ± 0.003	0.595 ± 0.005
800	0.507 ± 0.005	0.085 ± 0.003	0.592 ± 0.005
850	0.508 ± 0.005	0.081 ± 0.003	0.589 ± 0.005
900	0.527 ± 0.005	0.070 ± 0.003	0.596 ± 0.005
950	0.526 ± 0.005	0.068 ± 0.003	0.595 ± 0.005
1000	0.531 ± 0.005	0.062 ± 0.002	0.593 ± 0.005
1050	0.541 ± 0.005	0.056 ± 0.002	0.596 ± 0.005

Table 4.1: Signal acceptance for the $G \rightarrow \gamma\gamma$ decay channel, measured using simulation, showing statistical errors only.

At low mass the CP acceptance is $\sim 32\%$, while the CC is $\sim 22\%$, the CP then falls to $\sim 6\%$ at high mass and the CC rises to $\sim 54\%$. The total acceptance is then approximately constant, varying between $\sim 54\%$ and $\sim 58\%$.

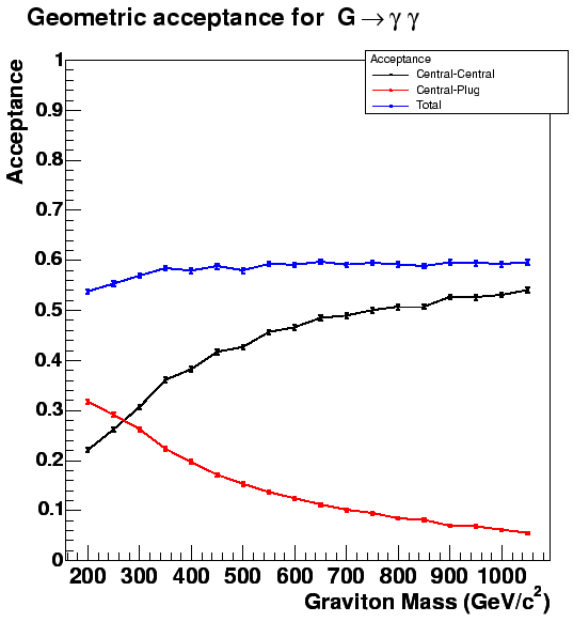

Figure 4.1: Signal acceptance for the $G \to \gamma\gamma$ decay channel, measured using simulation, showing statistical errors only.

This results from the different angular decay distributions of the gluon-gluon and quark-quark initiated fractions, with gluon fusion dominating the cross-section at low mass, favouring decays resulting in at least one photon being reconstructed in the plug region. The angular distributions for the diphoton decay mode, in the graviton rest frame, are summarized in Table 4.2 and illustrated in Figure 4.2 [22].

Process	Distribution
$gg \to G \to \gamma\gamma(\text{or } gg)$	$1 + 6\cos^2\theta^* + \cos^4\theta^*$
$q\bar{q} \to G \to \gamma\gamma(\text{or } gg)$	$1 - \cos^4\theta^*$

Table 4.2: Angular distributions in graviton production for the diphoton decay mode. θ^* is the polar angle of the outgoing particle in the graviton rest frame.

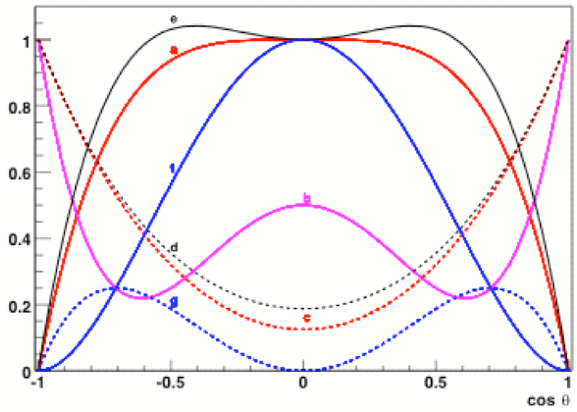

Figure 4.2: Angular distributions in graviton production and decay. Line (c) shows $gg \rightarrow G \rightarrow \gamma\gamma$ and line (a) $q\bar{q} \rightarrow G \rightarrow \gamma\gamma$.

4.2 Systematic Uncertainties

The following sections describe the systematic uncertainties on the acceptance arising from uncertainties in the energy scale, the parton distribution function used in Monte Carlo generation and variations in the initial and final state radiation.

4.2.1 Energy Scale

To perform an accurate comparison between data and Monte Carlo, any differences in the energy scale must be accounted for. A change in the CEM or PEM scales may result in a migration of events in and out of the E_T selection cuts and the $M_{\gamma\gamma} > 30$ Gev/c^2 mass window cut. The energy scales in data and Monte Carlo are compared using $Z \rightarrow ee$ events in a mass range of 82 GeV/c^2 $< M_{ee} <$ 98 GeV/c^2, providing a pure sample [56]. The percentage difference between the means of the data and Monte Carlo mass spectra, as shown in Figure 4.3, are calculated for various detector subregions, roughly corresponding to the individual towers. The error is then given by the standard deviation of the Gaussian distribution fitted to the difference in the means.

Both CEM and PEM uncertainties are taken as 1%.

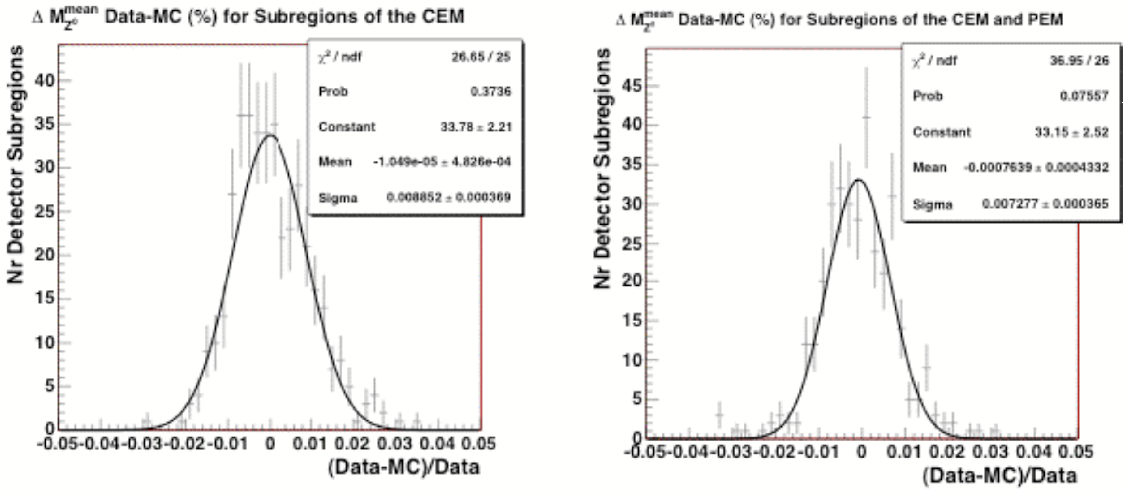

Figure 4.3: Difference between the mass spectra in $Z \rightarrow ee$ data and Monte Carlo, in the range 82 GeV/c^2 < M$_{ee}$ < 98 GeV/c^2, for the differing subdetector regions, for CC and CP events.

The corresponding change in the acceptance, estimated by varying the 15 GeV threshold by ± 1% uncertainty in the energy scales is shown, as a function of graviton mass, in Table 4.3 for CC events and in Table 4.4 for CP events. The systematic uncertainty is then taken as the resulting fractional percentage difference in the acceptance, as shown in Equation 4.3:

$$\% \text{ Diff} = \frac{\delta A}{A} \cdot 100 \tag{4.3}$$

where δA is the difference between the acceptance calculated using the 15 GeV selection cut and that calculated with the threshold fluctuated by ±1%, the greater of the two values being taken. The uncertainty on the energy scale is then taken as 0.1% for the CEM and 0.8% for the PEM.

$M_G(GeV/c^2)$	Acceptance (%)			% Diff
	$E_T > 15$ GeV	$E_T > 15.15$ GeV	$E_T > 14.75$ GeV	
200	20.65	20.64	20.66	0.05
250	26.43	26.41	26.45	0.08
300	30.06	30.06	30.10	0.13
350	34.23	34.22	34.24	0.03
400	37.61	37.60	37.61	0.03
450	41.12	41.12	41.12	0.00
500	42.53	42.53	42.52	0.02
550	45.82	45.81	45.87	0.11
600	47.06	47.06	47.07	0.02
650	49.62	49.61	49.62	0.02
700	50.75	50.75	50.76	0.02
750	50.82	50.80	50.85	0.06
800	52.36	52.36	52.38	0.04
850	52.59	52.57	52.63	0.08
900	53.95	53.94	53.96	0.02
950	53.97	53.96	54.00	0.06
1000	55.45	55.45	55.46	0.02
1050	54.82	54.81	54.84	0.04

Table 4.3: Fractional variation in acceptance in central-central events, resulting from a 1% fluctuation in the E_T threshold.

4.2.2 Parton Distribution Functions

The event kinematics are dependent on the parton distribution functions (PDFs), describing the parton structure used to generate the Monte Carlo, and are included as a systematic error on the acceptance. As described in Section 1.1.5, the quarks carry only a fraction of the total proton energy. Data from ex-

$M_G(GeV/c^2)$	Acceptance (%)			% Diff
	$E_T > 15$ GeV	$E_T > 15.15$ GeV	$E_T > 14.75$ GeV	
200	33.44	33.43	33.45	0.03
250	30.60	30.59	30.63	0.10
300	27.90	27.88	27.92	0.07
350	24.61	24.59	24.63	0.08
400	21.43	21.42	21.45	0.09
450	19.31	19.29	19.31	0.10
500	17.36	17.35	17.39	0.17
550	15.20	15.19	15.21	0.07
600	13.14	13.13	13.16	0.15
650	11.75	11.75	11.77	0.17
700	11.32	11.31	11.34	0.18
750	10.25	10.24	10.27	0.20
800	9.06	9.05	9.06	0.11
850	8.75	8.74	8.75	0.11
900	7.32	7.31	7.36	0.55
950	6.59	6.57	6.62	0.46
1000	6.09	6.09	6.10	0.16
1050	5.81	5.76	5.82	0.86

Table 4.4: Fractional variation in acceptance in central-plug events, resulting from a 1% fluctuation in the E_T threshold.

periments such as HERA, and fixed target experiments at the Tevatron, have been used to probe the structure of the proton, to establish the probability that a given parton carries a fraction x of the momentum, where the momentum density functions are then given by:

$$\sum_f \int_0^1 x f(x, Q^2) dx = 1 \tag{4.4}$$

where Q is the momentum transfer of the probe particle. The PDFs are dependent on both x and Q^2, with measurements over a range of of values being used by the CTEQ and MRST groups to form sets of 'global' PDFs. The CTEQ5L PDFs are used to generate the $G \rightarrow \gamma\gamma$ *HERWIG* Monte Carlo, from which the acceptance is calculated. To investigate the effect of varying the PDFs, *PYTHIA* $G \rightarrow \gamma\gamma$ Monte Carlo is used, as the PDFs may then be changed at the parton level, with the events generated over a range of graviton masses, using CTEQ5L and MRST high and low gluon and MRST high and low α_s, and using CC events to obtain the fractional difference:

$$\text{Diff}_{\text{PDF}} = \frac{A_{PDF} - A_{CTEQ5L}}{A_{CTEQ5L}} \tag{4.5}$$

The acceptance, together with the statistical error, is shown in Table 4.5 as a function of graviton mass for the CTEQ5L and MRST PDFs. The fractional difference is then shown as a function of graviton mass in Table 4.6, from which we take the relative change in acceptance due to a change in PDF to be 4%, independent of graviton mass, with the statistical uncertainty deemed to be insignificant.

4.2.3 Initial and Final State Radiation

Possible biases may also originate from differences in the amount of radiation between the data and the Monte Carlo, due to mismodelling of the QCD radiation in leading order (LO) generators. The effects of increasing and decreasing this radiation are taken as a systematic error on the acceptance, and are estimated using *PYTHIA*, generating events at each graviton mass, as with the

$M_G(GeV/c^2)$	Acceptance (%)					
	CTEQ5L	MRST leading order fit				
		Central	High Gluon	Low Gluon	High α_s	Low α_s
250	27.9 ± 0.3	27.5 ± 0.4	27.0 ± 0.5	26.7 ± 0.5	27.3 ± 0.4	26.3 ± 0.4
350	34.5 ± 0.4	33.6 ± 0.6	33.2 ± 0.5	34.0 ± 0.6	35.0 ± 0.6	35.2 ± 0.6
450	42.1 ± 0.4	40.7 ± 0.6	38.8 ± 0.7	40.5 ± 0.9	40.7 ± 0.6	41.2 ± 0.6
550	48.6 ± 0.5	46.3 ± 0.7	44.6 ± 0.7	47.4 ± 0.7	46.6 ± 0.9	47.3 ± 0.7
650	52.2 ± 0.5	50.8 ± 0.8	50.3 ± 0.8	51.4 ± 0.9	50.6 ± 0.8	50.9 ± 0.8
750	55.3 ± 0.5	54.0 ± 0.8	52.6 ± 0.8	54.4 ± 0.9	53.4 ± 0.8	54.0 ± 0.8
850	56.5 ± 0.6	54.4 ± 0.9	54.2 ± 0.8	55.7 ± 0.8	54.3 ± 1.0	55.5 ± 0.8

Table 4.5: Acceptance as a function of graviton mass for CTEQ5L and different MRST parton distribution functions, showing statistical errors.

$M_G(GeV/c^2)$	$Diff_{PDF}$
250	0.04
350	0.02
450	0.05
550	0.05
650	0.03
750	0.03
850	0.03

Table 4.6: Difference in acceptance caused by changing the parton distribution function, as a function of graviton mass.

PDF uncertainty. The fractional difference in the acceptance in CC events, shown in Table 4.7, is then used to obtain the fractional percentage error in the acceptance, which is taken conservatively as 4%.

M_G (GeV/c^2)	Acceptance			$\text{Diff}_{\text{IFSR}}$
	more IFSR	less IFSR	default	
200	0.228 ± 0.004	0.223 ± 0.004	0.226 ± 0.004	0.02
250	0.250 ± 0.004	0.239 ± 0.004	0.242 ± 0.004	0.03
300	0.259 ± 0.004	0.254 ± 0.004	0.256 ± 0.004	0.01
350	0.281 ± 0.004	0.275 ± 0.004	0.271 ± 0.004	0.04
400	0.278 ± 0.004	0.274 ± 0.004	0.269 ± 0.004	0.04
450	0.269 ± 0.004	0.270 ± 0.004	0.278 ± 0.004	0.03
500	0.286 ± 0.005	0.275 ± 0.004	0.284 ± 0.005	0.05
550	0.281 ± 0.004	0.278 ± 0.004	0.275 ± 0.004	0.02
600	0.284 ± 0.005	0.283 ± 0.004	0.284 ± 0.005	0.01
650	0.281 ± 0.004	0.275 ± 0.004	0.277 ± 0.004	0.01
700	0.276 ± 0.004	0.265 ± 0.004	0.275 ± 0.004	0.04
750	0.274 ± 0.004	0.265 ± 0.004	0.267 ± 0.004	0.03
800	0.258 ± 0.004	0.251 ± 0.004	0.257 ± 0.004	0.03
850	0.255 ± 0.004	0.239 ± 0.004	0.247 ± 0.004	0.03
900	0.229 ± 0.004	0.230 ± 0.004	0.233 ± 0.004	0.01
950	0.221 ± 0.004	0.220 ± 0.004	0.220 ± 0.004	0.005
1000	0.196 ± 0.004	0.196 ± 0.004	0.204 ± 0.004	0.04
1050	0.178 ± 0.004	0.174 ± 0.004	0.177 ± 0.004	0.02

Table 4.7: Difference in acceptance as a function of graviton mass, showing systematic errors, due to differences in the initial and final state radiation.

Chapter 5

Efficiency

Particle identification efficiency is defined as the probability that a final state photon is selected, once all selection criteria are applied. To determine the expected number of $G \rightarrow \gamma\gamma$ signal events, the probability of a diphoton event passing the identification selection must be known accurately. The loss of photon candidates due to kinematic and geometrical effects is accounted for in the acceptance, as described in Chapter 4. The efficiency then takes into account the probability that a diphoton event will pass the particle identification selection (ϵ_{id}), and the probability that the event will be selected by the online trigger ($\epsilon_{trigger}$). To measure the identification efficiency, pure samples of events are required, to determine the probability of a final state particle being selected by the applied cuts. No pure samples of photons are available in data, therefore the efficiency is measured in simulation and tuned to match the response in data, using $Z \rightarrow ee$ events, as the electrons produce near identical signals to photons in the EM calorimeter. These have minimal background contamination, and the efficiencies in data and simulation may then be compared. Single photon efficiencies are also presented, measured using simulation, to estimate high energy efficiency behaviour, as no data are available for very high-E_T studies. The efficiency of the online trigger is measured using

data.

5.1 Single Photon Identification Efficiency

The identification efficiencies of single photons are measured to verify that there is an approximately flat distribution in the efficiency, as a function E_T. As no data are available in the high energy regime, $G \rightarrow \gamma\gamma$ Monte Carlo is used. Photons are selected using the central and plug photon candidate selection criteria, as described in Section 3.4 and shown in Tables 3.8 and 3.9. The initial χ^2 selection cut used for central photon candidates was the standard CDF baseline analysis cut of $\chi^2 < 20$, rather than the χ^2 cut of ($\chi^2 < 20$ if $E_T < 50$ GeV and $\chi^2 < 50$ if $E_T > 50$ GeV), as shown in Table 3.8. This was changed due to the strong E_T dependence seen in the (N-1) distribution, which is defined as the efficiency of given a cut after all other cuts have been applied:

$$\epsilon_{(N-1)} = \frac{\text{number of events passing all photon cuts}}{\text{number of events passing all cuts with no requirement on selected cut}} \tag{5.1}$$

The modification of the χ^2 cut is described in detail in Section 5.1.1. Figures 5.1 and 5.2 show the (N-1) efficiencies for all other single photon identification cuts used, as a function of E_T, for $E_T > 50$ GeV. They show an approximately flat distribution. The low energy behaviour is discussed in Section 5.6.

5.1.1 χ^2 Efficiency

Figure 5.3 shows the (N-1) distribution for the central photon selection cut $\chi^2 < 20$. Due to the strong E_T dependence exhibited at high energies, two

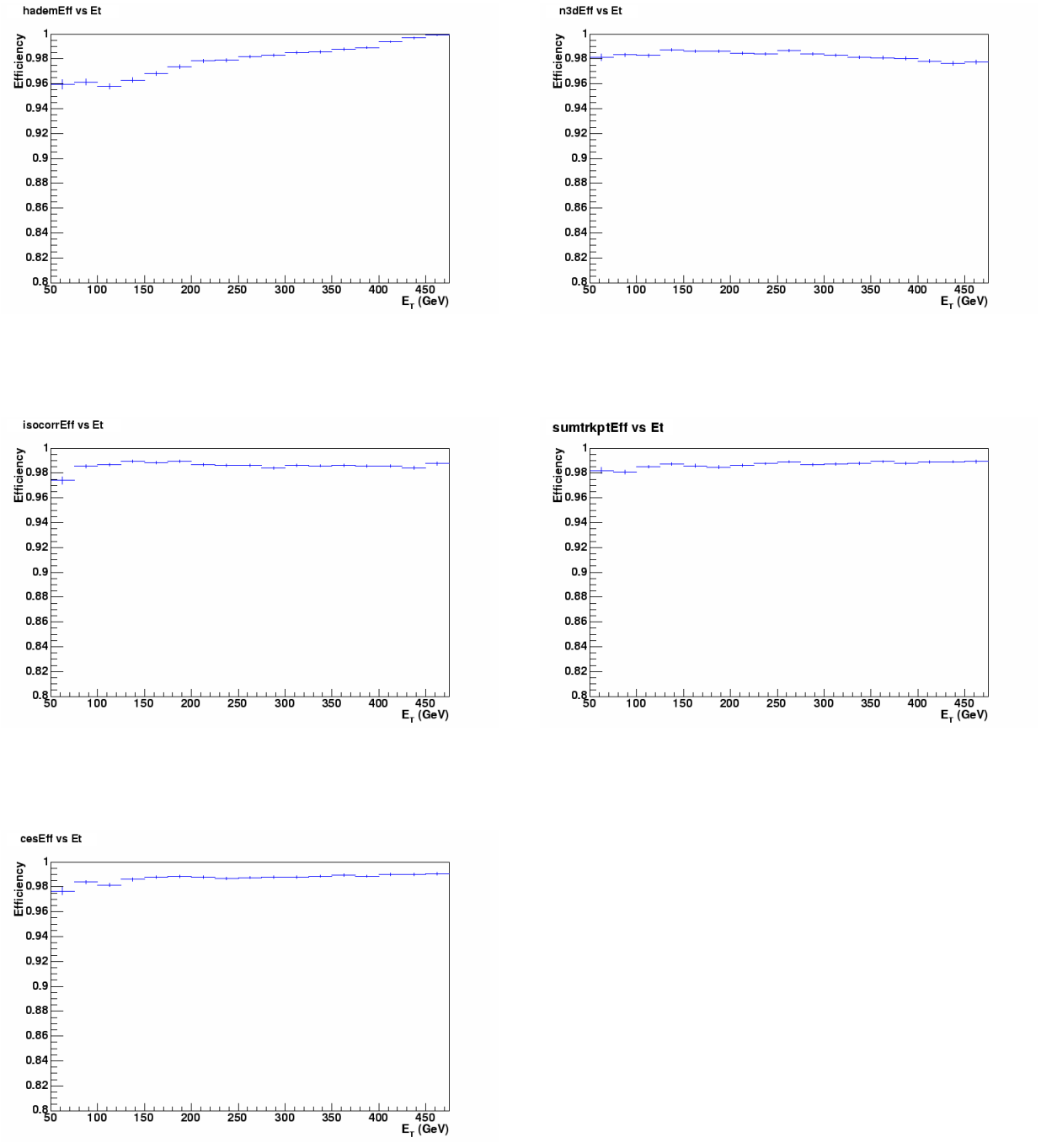

Figure 5.1: (N-1) efficiencies for central photon identification selection cuts as a function of E_T, for $E_T > 50$ GeV.

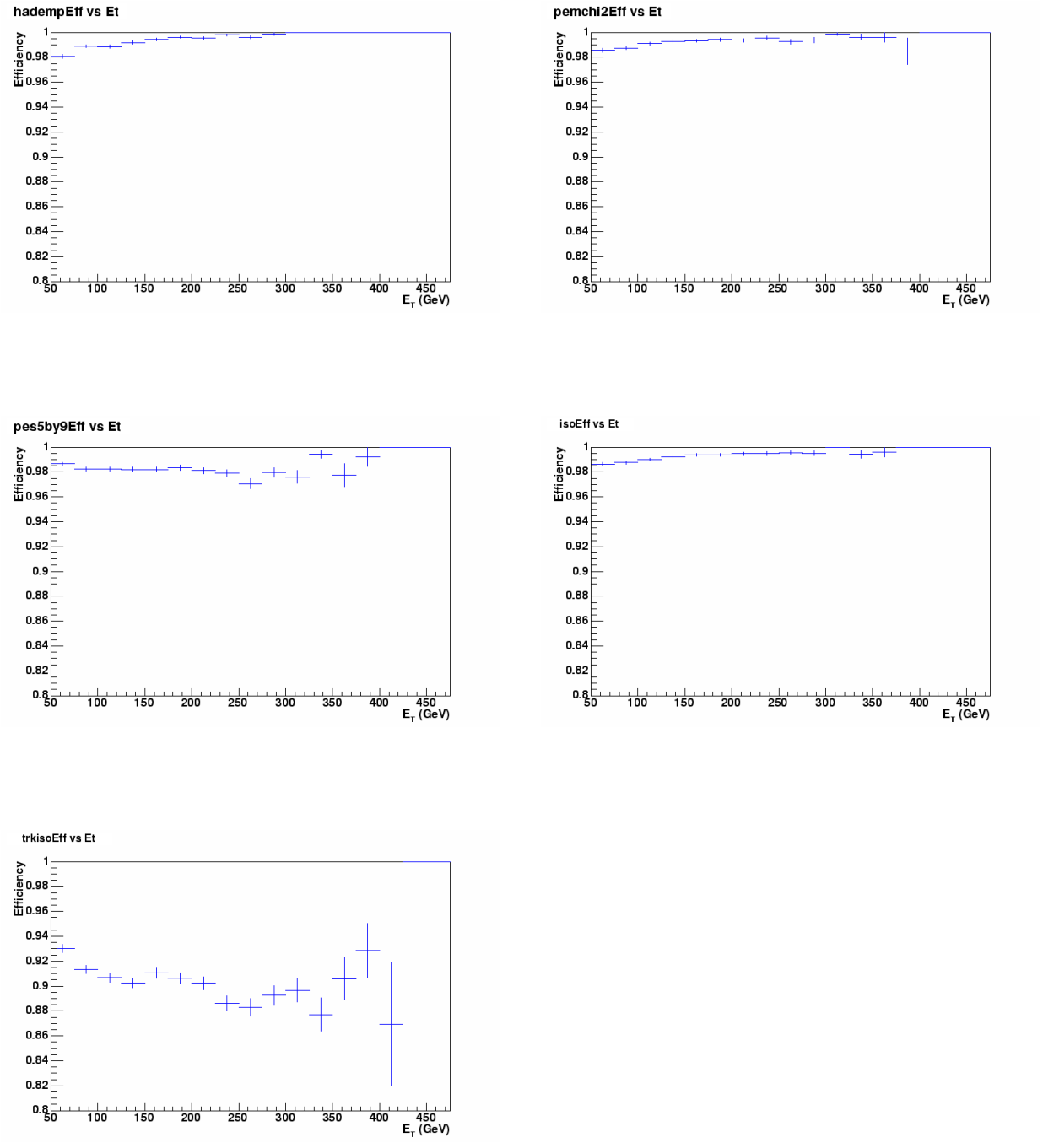

Figure 5.2: (N-1) efficiencies for plug photon identification selection cuts as a function of E_T, for $E_T > 50$ GeV.

high-E_T ($\geq$ 100 GeV) jet data samples (labelled 'gjt40d' and 'gexo1h') are used to show whether this is a Monte Carlo generated effect or whether the data exhibit the same behaviour.

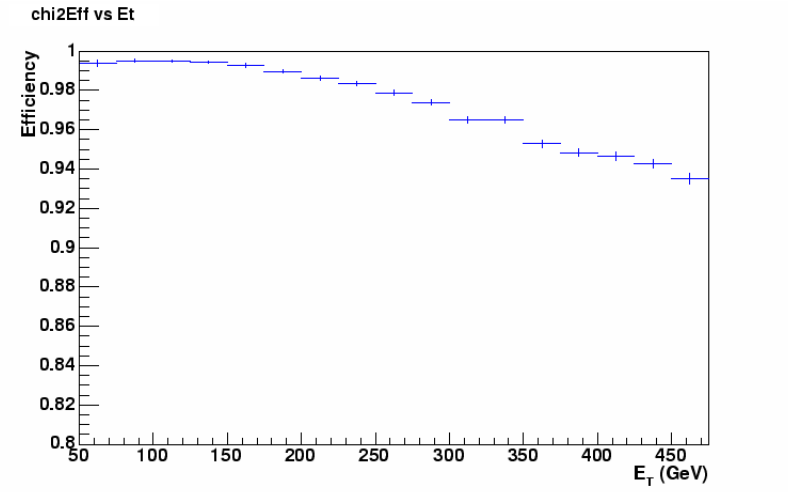

Figure 5.3: Central χ^2 (N-1) efficiency as a function of E_T.

Central photons are selected from the jet samples using the standard cuts shown in Table 3.8, with no χ^2 cut applied. Additional selection criteria, shown in Table 5.1, are applied for the removal of cosmic ray and halo events.

Variable	Cut
Number of track stubs (within 30° of γ)	$= 0$
Hadron TDC timing	$-4 < t\ (ns) < 7$
ϕ seed index	$\neq 0$ or 23
Missing E_T	< 20.0

Table 5.1: Additional photon selection cuts applied to jet data for cosmic ray and halo event removal [57].

The (N-1) efficiencies, when applying the standard $\chi^2 < 20$ cut, and for a looser cut of $\chi^2 < 50$, are then calculated. These are shown, as a function of E_T, in Table 5.2 and Figure 5.4. No strong E_T dependence is exhibited in the data, indicating that it is an effect generated in the modelling of the Monte Carlo. Applying the looser cut to the Monte Carlo results in a gain in efficiency and flattening of the distribution, as shown in Figure 5.5. This behaviour in the simulation is not currently well understood and, as a result of requiring a flat distribution, the central photon selection cut used for the analysis is $\chi^2 < 20$ if $E_T < 50$ GeV and $\chi^2 < 50$ if $E_T > 50$ GeV.

$\chi^2 < 20$		
Photon E_T (GeV)	Efficiency (dataset 1, 'gjt40d')	Efficiency (dataset 2, 'gexo1h')
15-50	0.920 ± 0.015	0.939 ± 0.013
51-100	0.917 ± 0.010	0.908 ± 0.009
101-150	0.906 ± 0.010	0.916 ± 0.008
151-200	0.926 ± 0.032	0.922 ± 0.025
201-250	1.000 ± 0	0.857 ± 0.094
> 251	1.000 ± 0	1.000 ± 0
$\chi^2 < 50$		
photon E_T (GeV)	Efficiency (dataset 1, 'gjt40d')	Efficiency (dataset 2, 'gexo1h')
15-50	0.974 ± 0.009	0.970 ± 0.009
51-100	0.963 ± 0.007	0.961 ± 0.006
101-150	0.967 ± 0.006	0.963 ± 0.006
151-200	0.985 ± 0.015	0.965 ± 0.017
201-250	1.000 ± 0	0.929 ± 0.069
> 251	1.000 ± 0	1.000 ± 0

Table 5.2: (N-1) efficiencies for $\chi^2 < 20$ and $\chi^2 < 50$ using jet data samples.

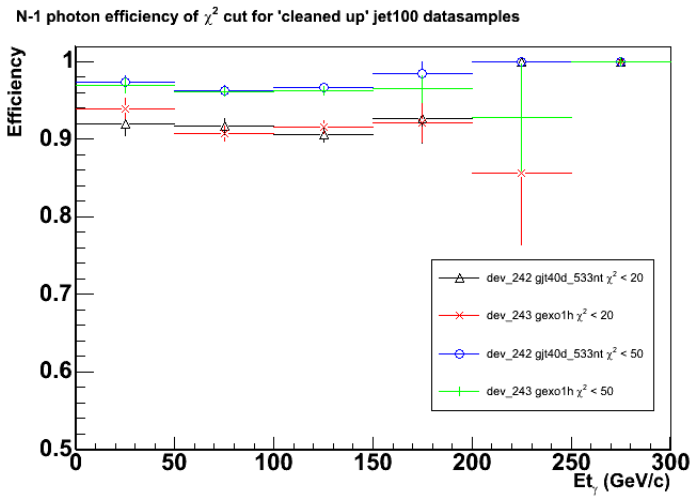

Figure 5.4: (N-1) efficiencies for $\chi^2 < 20$ and $\chi^2 < 50$ using jet data samples.

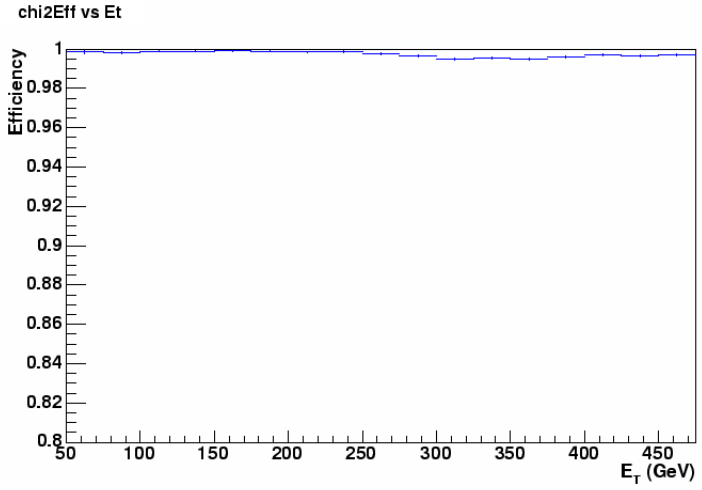

Figure 5.5: Central χ^2 efficiency for the looser $\chi^2 < 50$ for $E_T > 50$ GeV.

To ensure agreement between data and simulation, a pure $Z \to ee$ dataset is compared to Monte Carlo. This is described in Section 5.6, following Section 5.2.1, as it utilizes the same method in selecting Z candidates.

5.2 $G \to \gamma\gamma$ Efficiency

Due to the difficulty in distinguishing true photons from background, it is not possible to use a highly pure sample of final state photons to measure the $G \to \gamma\gamma$ identification efficiency. They must therefore be measured using simulation. A highly pure sample of electrons, from decays of the Z boson, are then used to emulate the photon cuts, to validate the simulation's treatment of the photon variables, as the total energy signal deposited in the calorimeter is indistinguishable for photons and electrons. The efficiency for $G \to \gamma\gamma$ events is then given by:

$$\epsilon_{id} = \epsilon_{MC} \times \text{Corr} \tag{5.2}$$

where ϵ_{MC} is the efficiency measured in simulation and Corr is a correction factor applied to the diphoton Monte Carlo to account for variations between data and simulation, measured using the $Z \to ee$ samples.

5.2.1 $G \to \gamma\gamma$ Correction Factors

Using the central electron trigger described in Section 3.1.2, electron data are selected. Two datasets are used, with the average of the resulting correction factors being taken. In each event, one electron is randomly selected, to remove possible trigger bias, and required to pass the central selection criteria, discussed in Section 3.4.3 and summarised in Table 3.10. These emulate the selection criteria used for photons, in order that the data/simulation comparison may be used to validate the photon variable efficiencies. To emulate these

cuts, the track associated with the electron must be taken into account. The number of tracks pointing to a cluster must be ≤ 2 rather than ≤ 1, since one track is required for an electron. The second (low p_T) track can arise from a soft underlying event. The cut on the highest p_T track is therefore also changed to a cut on the second highest p_T track. Similarly, for tracking isolation, the sum of track p_Ts in a cone of 0.4 is modified to the sum of track p_Ts minus the highest track p_T. Additionally, the ratio of energy (E) to momentum (p) must satisfy $0.9 < E/P < 1.1$, to suppress radiative electrons.

The second electron from the Z decay, either central or plug, is selected with the loose requirements shown below in Tables 5.3 and 5.4, and regarded as an unbiased electron for the efficiency study, forming the 'probe' leg. To suppress background, the loose requirements include the E/P cut for central electrons and a cut of Nhits ≥ 3 on the number of Phoenix tracking hits in the plug (defined in Section 3.2.1). Despite a better electron rejection factor, as defined in Equation 5.3:

$$e_rej = \frac{\text{number of electrons passing selection criteria with no tracking requirement}}{\text{number passing with all cuts applied}} \tag{5.3}$$

being obtained for the Phoenix tracking (see Appendix A), the photon selection for this analysis uses the Silicon Standalone tracking to differentiate photons from electrons in the plug. This is due to the method of scaling the photon efficiencies, measured in simulation, by the correction factors obtained using the pure $Z \rightarrow ee$ sample. As the photon variables are emulated in the electron selection, it is necessary to modify the photon cut for electrons. For the standalone silicon tracking method, this is simply done by subtracting off the highest p_T track, giving:

$$\text{Sum Track } p_T \text{ (cone0.4)} - \text{Highest Track } p_T < (2.0 + 0.005 \times E_T) \text{ GeV/c} \tag{5.4}$$

as opposed to Sum track p_T (cone0.4) $< 2.0 + 0.005 \times E_T$. In order to use the Phoenix tracking, a second dataset would need to be created as the main Phoenix track would have to be removed to emulate the photon cut using electrons. The second dataset would then be created without the main track, and checked for remaining tracks. To remove this need for generating a second dataset, the Silicon Standalone tracking method is used in photon selection.

Variable	Cut
Region	Central
Fiducial	CES $\lvert x\rvert < 21.0$ cm
	CES 9.0 cm $< \lvert z\rvert <$230.0 cm
E_T	>15 GeV
E/p	$0.9 < E/P < 1.1$

Table 5.3: Loose selection cuts for the probe electron in the central calorimeter.

Variable	Cut
Region	Plug
PES Fiducial	$1.2 < \lvert\eta\rvert < 2.8$
E_T	>15 GeV
Phoenix hits	$\geq$3

Table 5.4: Loose selection cuts for the probe electron in the plug calorimeter.

To determine the number of signal and background events in the data, a fit range of 60 GeV/c^2 $< M_{ee} <$ 120 GeV/c^2 is used. The signal is assumed to

take the form of a Gaussian distribution with a linear background. The tight cuts are applied sequentially to the probe leg, each time fitting the Gaussian in the range of 86-98 GeV/c^2 around the Z pole, fixing the mean and width, and allowing the other parameters to float. This ensures that the mean and width of the Z peak are correct. The identification efficiencies are then measured using two methods, with the difference in efficiencies between the methods in Monte Carlo being taken as a systematic uncertainty on the method, as they are not affected by background. The first method uses the fact that the height of the Gaussian is proportional to the number of signal events. The efficiency of the ith selection cut is determined by dividing the height of the Gaussian, after the ith selection cut has been applied, by that of the height after only loose selection criteria have been applied. For the second method, the linear background fit is integrated between 66-72 GeV/c^2 and 112-118 GeV/c^2 (the sidebands) and averaged, thereby obtaining an estimate of the background around the Z pole. These values are chosen to give a combined width of 12 GeV/c^2, corresponding to the peak width, and are both 14 GeV/c^2 from this region. The integral of the peak, between 86 and 98 GeV/c^2, for the invariant mass spectrum of the ith cut, minus the background from the sidebands, is then divided by the integral of the peak, again after background subtraction, after only probe cuts are applied.

For events with the probe electron in the central calorimeter, the fact that one electron has already passed tight selection cuts must be taken into account. The efficiency is then calculated using:

$$\epsilon^{i}_{central} = \frac{N_{Ti} + N_{TT}}{2N_{TT} + N_{TL}} \tag{5.5}$$

where $N^{central}_{Ti}$ is the number of central-central events with one leg passing all tight cuts and the second leg passing all cuts up to and including the ith cut, N_{TT} is the number of events with both legs passing all cuts and N_{TL} is

the number of events with one leg passing all cuts and one leg passing loose cuts but failing tight cuts. The full derivation is given in Appendix B. For plug probe electrons, the electron identification efficiency is calculated using:

$$\epsilon^{i}_{plug} = \frac{N^{plug}_{Ti}}{N_{TP}} \tag{5.6}$$

where N^{plug}_{Ti} is the number of central-plug events with one leg passing all tight cuts and the second leg passing all cuts up to and including the ith cut and N_{TP} is defined as the number of events where at least one electron passes the tight cuts and the other one can pass either the loose or tight cuts. Tables 5.5 and 5.6 show the cumulative efficiencies for data and simulation for central electrons for the two datasets, while Tables 5.7 and 5.8 show the plug efficiencies.

	Data (Method 1)	Simulation (1)	Data (Method 2)	Simulation (2)
Variable	Efficiency %			
Had/Em	99.51 ± 0.10	98.99 ± 0.06	99.27 ± 0.24	98.53 ± 0.08
Isolation	97.57 ± 0.35	96.74 ± 0.11	96.23 ± 0.53	95.65 ± 0.14
χ^2	96.92 ± 0.43	96.49 ± 0.12	95.19 ± 0.59	95.47 ± 0.14
N3D	96.27 ± 0.50	95.96 ± 0.13	94.34 ± 0.64	94.95 ± 0.15
Track p_T	95.62 ± 0.56	95.11 ± 0.14	93.36 ± 0.68	94.00 ± 0.16
Sum track p_T	93.84 ± 0.65	93.82 ± 0.15	91.49 ± 0.76	92.58 ± 0.17
Second CES cluster	93.35 ± 0.69	92.61 ± 0.16	90.66 ± 0.79	91.45 ± 0.18

Table 5.5: Cumulative efficiencies for central electron selection cuts for data and simulation, showing statistical errors, for the first dataset.

The correction factor for the simulated data is calculated as the ratio of the two efficiencies (data/ Monte Carlo). The total central and plug electron

	Data (Method 1)	Simulation (1)	Data (Method 2)	Simulation (2)
Variable	Efficiency %			
Had/Em	99.10 ± 0.21	98.99 ± 0.06	99.56 ± 0.17	98.53 ± 0.08
Isolation	96.40 ± 0.44	96.74 ± 0.11	96.66 ± 0.47	95.65 ± 0.14
χ^2	95.05 ± 0.50	96.49 ± 0.12	95.70 ± 0.52	95.47 ± 0.14
N3D	94.15 ± 0.59	95.96 ± 0.13	94.64 ± 0.58	94.95 ± 0.15
Track p_T	92.50 ± 0.65	95.11 ± 0.14	93.39 ± 0.63	94.00 ± 0.16
Sum track p_T	91.15 ± 0.73	93.82 ± 0.15	91.77 ± 0.69	92.58 ± 0.17
Second CES cluster	90.85 ± 0.73	92.61 ± 0.16	91.52 ± 0.70	91.45 ± 0.18

Table 5.6: Cumulative efficiencies for central electron selection cuts for data and simulation, showing statistical errors, for the second dataset.

	Data (Method 1)	Simulation (1)	Data (Method 2)	Simulation (2)
Variable	Efficiency %			
Had/Em	97.75 ± 0.22	98.90 ± 0.03	97.48 ± 0.24	98.69 ± 0.04
Isolation	93.58 ± 0.34	96.46 ± 0.06	93.53 ± 0.37	95.90 ± 0.07
$\chi^2_{3\times3}$	83.95 ± 0.51	90.34 ± 0.09	84.23 ± 0.55	89.42 ± 0.10
5 by 9	82.83 ± 0.52	90.01 ± 0.09	83.51 ± 0.56	89.03 ± 0.10
Track isolation	77.85 ± 0.57	87.21 ± 0.11	79.97 ± 0.61	86.00 ± 0.12

Table 5.7: Cumulative efficiencies for plug electron selection cuts for data and simulation, showing statistical errors, for the first dataset.

efficiencies, with corresponding correction factors, are shown in Tables 5.9 and 5.10, respectively, for the two datasets.

The correction factors are then averaged for the central and plug regions, keeping a conservative value of 1% for the systematic error, giving final values of $1.00 \pm 0.52\%(\text{stat}) \pm 1\%(\text{syst})$ for the central region and $0.91 \pm 0.39\%(\text{stat}) \pm 1\%(\text{syst})$ for the plug.

	Data (Method 1)	Simulation (1)	Data (Method 2)	Simulation (2)
Variable	Efficiency %			
Had/Em	95.66 ± 0.25	98.90 ± 0.03	96.97 ± 0.23	98.69 ± 0.04
Isolation	91.95 ± 0.36	96.46 ± 0.06	92.42 ± 0.36	95.90 ± 0.07
$\chi^2_{3\times3}$	83.27 ± 0.48	90.34 ± 0.09	81.22 ± 0.53	89.42 ± 0.10
5 by 9	82.50 ± 0.49	90.01 ± 0.09	80.53 ± 0.53	89.03 ± 0.10
Track isolation	80.08 ± 0.51	87.21 ± 0.11	77.13 ± 0.57	86.00 ± 0.12

Table 5.8: Cumulative efficiencies for plug electron selection cuts for data and simulation, showing statistical errors, for the second dataset.

Calorimeter	Data (%)	Simulation (%)	Correction Factor
Central	93.35 ± 0.69	92.61 ± 0.16	1.01 ± 0.71% (stat) ± 1% (syst)
Plug	77.85 ± 0.57	87.21 ± 0.11	0.89 ± 0.59% (stat) ± 1% (syst)

Table 5.9: Total central and plug electron efficiencies and correction factors for first dataset, with statistical and systematic errors.

5.3 Trigger Efficiency

The trigger efficiency describes the probability that a $G \rightarrow \gamma\gamma$ signal event, passing the kinematic requirements, will be accepted by the trigger. The simulated data must then be re-weighted by this probability to predict the number of signal events expected. It is measured using samples which contain the trigger object, i.e. which pass the offline selection cuts, but do not have the trigger requirements imposed. The efficiency is given by

$$\epsilon_{trigger} = \frac{\text{number of triggered events passing offline cuts}}{\text{number of events passing offline cuts}} \qquad (5.7)$$

The efficiencies, at L2, are shown in Figure 5.6 for the DIPHOTON_12 and DIPHOTON_18 triggers, defined in Section 3.1, as a function of mass. A source of inefficiency arises at high mass due to the saturation of the ana-

Calorimeter	Data (%)	Simulation (%)	Correction Factor
Central	90.85 ± 0.73	92.61 ± 0.16	0.98 ± 0.75% (stat) ± 1% (syst)
Plug	80.08 ± 0.51	87.21 ± 0.11	0.92 ± 0.52% (stat) ± 1% (syst)

Table 5.10: Total central and plug electron efficiencies and correction factors for second dataset, with statistical and systematic errors.

logue to digital conversion boards, which digitize the calorimeter phototube signals to form the L1 and L2 tower E_T for trigger decisions, at an energy of 128 GeV for both the electromagnetic and hadronic calorimeters. Due to this, the ULTRA_PHOTON_50 and SUPER_PHOTON_70 EM and JET triggers, also described in Section 3.1, are used in conjunction with DIPHOTON_12 and 18. This removes any possible sources of inefficiency at L3. The trigger efficiency is then taken as 100%.

5.4 Scaled Single Photon Efficiencies

The cumulative efficiencies for single photons at each mass point, when sequentially applying the selection cuts and scaling by the correction factor, are defined as:

$$\epsilon_{cumulative} = \frac{\text{number passing selection cuts up to } i\text{th cut in given detector region}}{\text{number passing acceptance criteria for same region}} \tag{5.8}$$

and shown in Figure 5.7 for the central and plug regions.

5.5 Total Scaled $G \to \gamma\gamma$ Efficiencies

The total efficiency, defined as the fraction of diphoton events generated passing all selection cuts (equivalent to the acceptance times the efficiency), is pre-

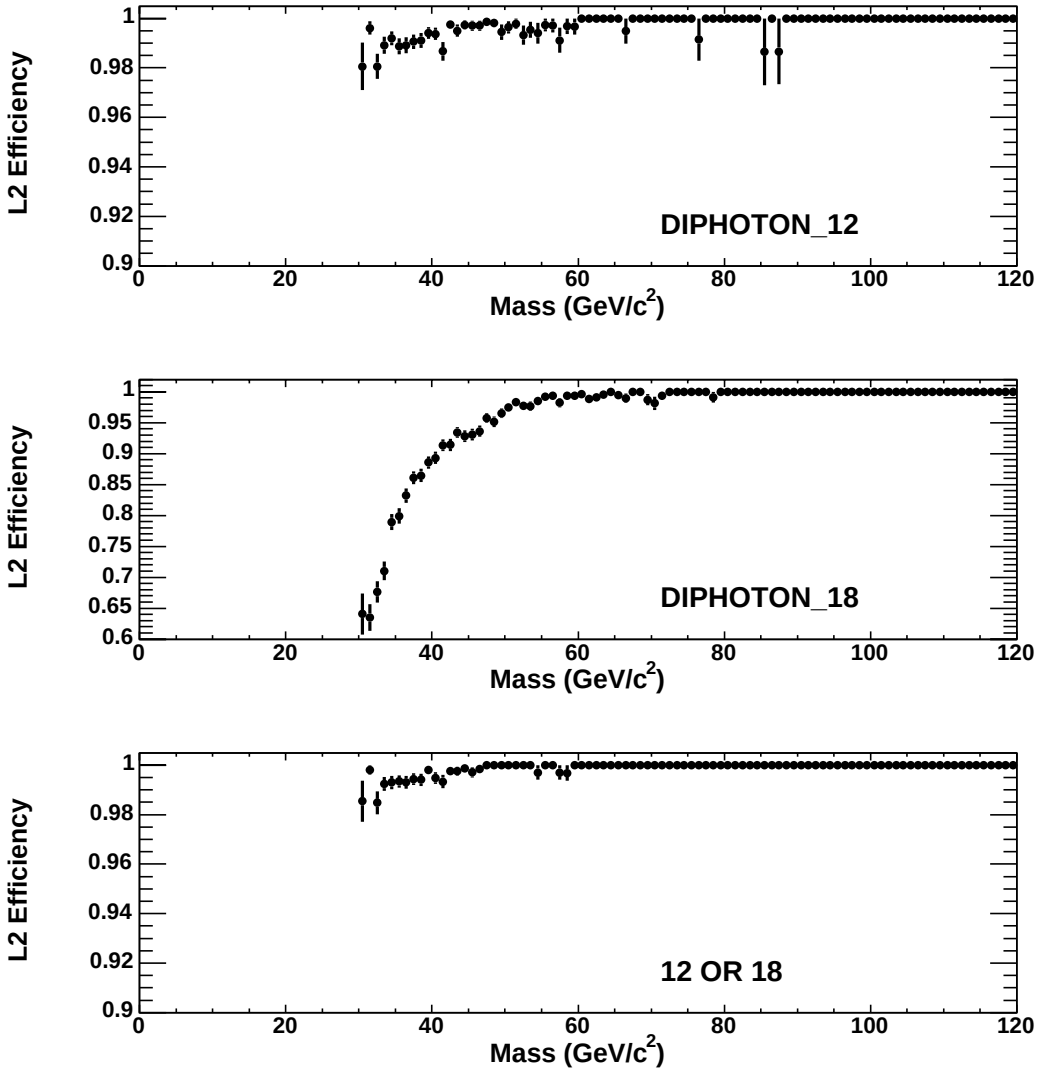

Figure 5.6: DIPHOTON_12 and DIPHOTON_18 trigger efficiencies, given as a function of mass.

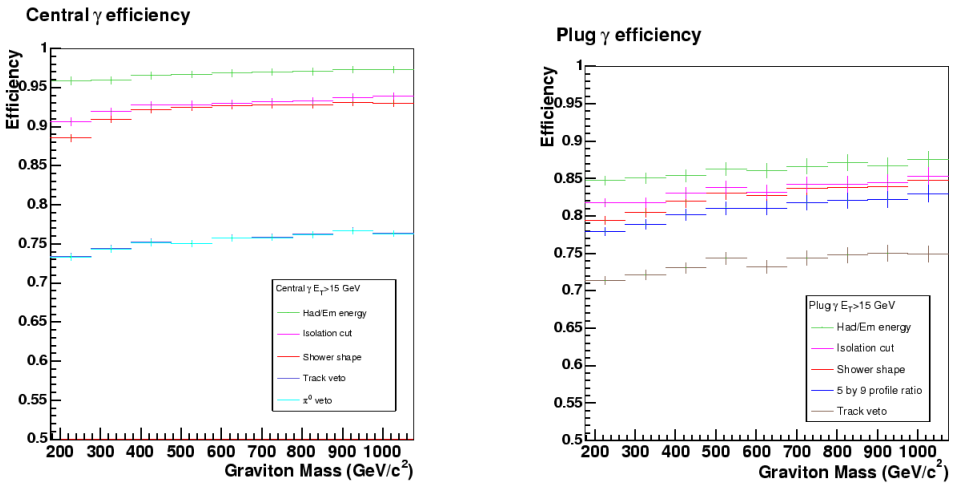

Figure 5.7: Scaled efficiency for a single photon to pass the selection criteria, shown for central photons on the left plot and plug photons on the right.

sented as a function of graviton mass, with masses in the range 200 GeV/c^2 to 1050 GeV/c^2, in Table 5.11. These efficiencies are then scaled by the correction factor ($Corr_{central} \times Corr_{central}$ for central-central events and $Corr_{central} \times Corr_{plug}$ for central-plug). The total corrected efficiencies are shown in Figure 5.8.

5.6 Low Energy Behaviour Data/ Monte Carlo Comparison

Data and simulation are compared, to ensure no anomalous behaviour is observed, using the low energy regime. This enables pure samples of Z candidates, selected with emulated photon selection criteria, as described above in Section 5.2.1, to be used. One electron is required to be central and to pass all tight central selection criteria. For central-central candidates the invariant

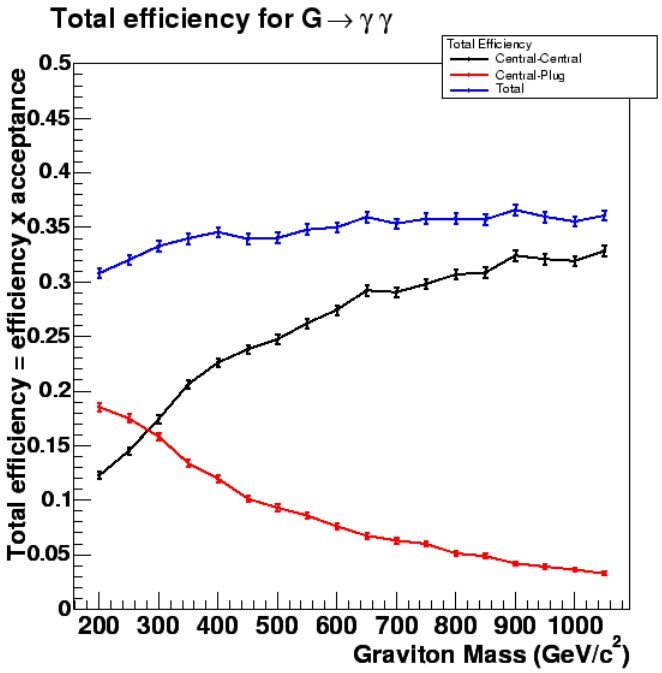

Figure 5.8: Total scaled efficiency (acceptance * efficiency) for the $G \rightarrow \gamma\gamma$ decay channel, measured using simulation, showing statistical errors only.

M_G(GeV/c^2)	Total Efficiency (CC)	Total Efficiency (CP)	Total Efficiency (CC + CP)
200	0.122 ± 0.003	0.185 ± 0.004	0.308 ± 0.005
250	0.145 ± 0.004	0.175 ± 0.004	0.320 ± 0.005
300	0.174 ± 0.004	0.158 ± 0.004	0.333 ± 0.005
350	0.206 ± 0.004	0.134 ± 0.003	0.340 ± 0.005
400	0.226 ± 0.004	0.120 ± 0.003	0.346 ± 0.005
450	0.238 ± 0.004	0.101 ± 0.003	0.339 ± 0.005
500	0.247 ± 0.004	0.093 ± 0.003	0.340 ± 0.005
550	0.262 ± 0.004	0.086 ± 0.003	0.348 ± 0.005
600	0.274 ± 0.004	0.076 ± 0.003	0.350 ± 0.005
650	0.292 ± 0.004	0.067 ± 0.003	0.359 ± 0.005
700	0.291 ± 0.004	0.063 ± 0.002	0.353 ± 0.005
750	0.298 ± 0.004	0.060 ± 0.002	0.358 ± 0.005
800	0.307 ± 0.004	0.051 ± 0.002	0.358 ± 0.005
850	0.309 ± 0.004	0.049 ± 0.002	0.357 ± 0.005
900	0.324 ± 0.004	0.042 ± 0.002	0.366 ± 0.005
950	0.321 ± 0.005	0.039 ± 0.002	0.360 ± 0.005
1000	0.319 ± 0.005	0.036 ± 0.002	0.355 ± 0.005
1050	0.328 ± 0.005	0.033 ± 0.002	0.361 ± 0.005

Table 5.11: Total efficiency (acceptance * efficiency) for the $G \rightarrow \gamma\gamma$ decay channel, measured using simulation, showing statistical errors only.

mass is required to be in the mass window of 76 GeV/c^2 < M_{ee} < 106 GeV/c^2, and within 81 GeV/c^2 < M_{ee} < 101 GeV/c^2 for central-plug candidates. The efficiencies are calculated using the second, probe electron, as described previously. The (N-1) efficiencies for central and plug selection criteria are shown below in Figures 5.9 and 5.10, respectively.

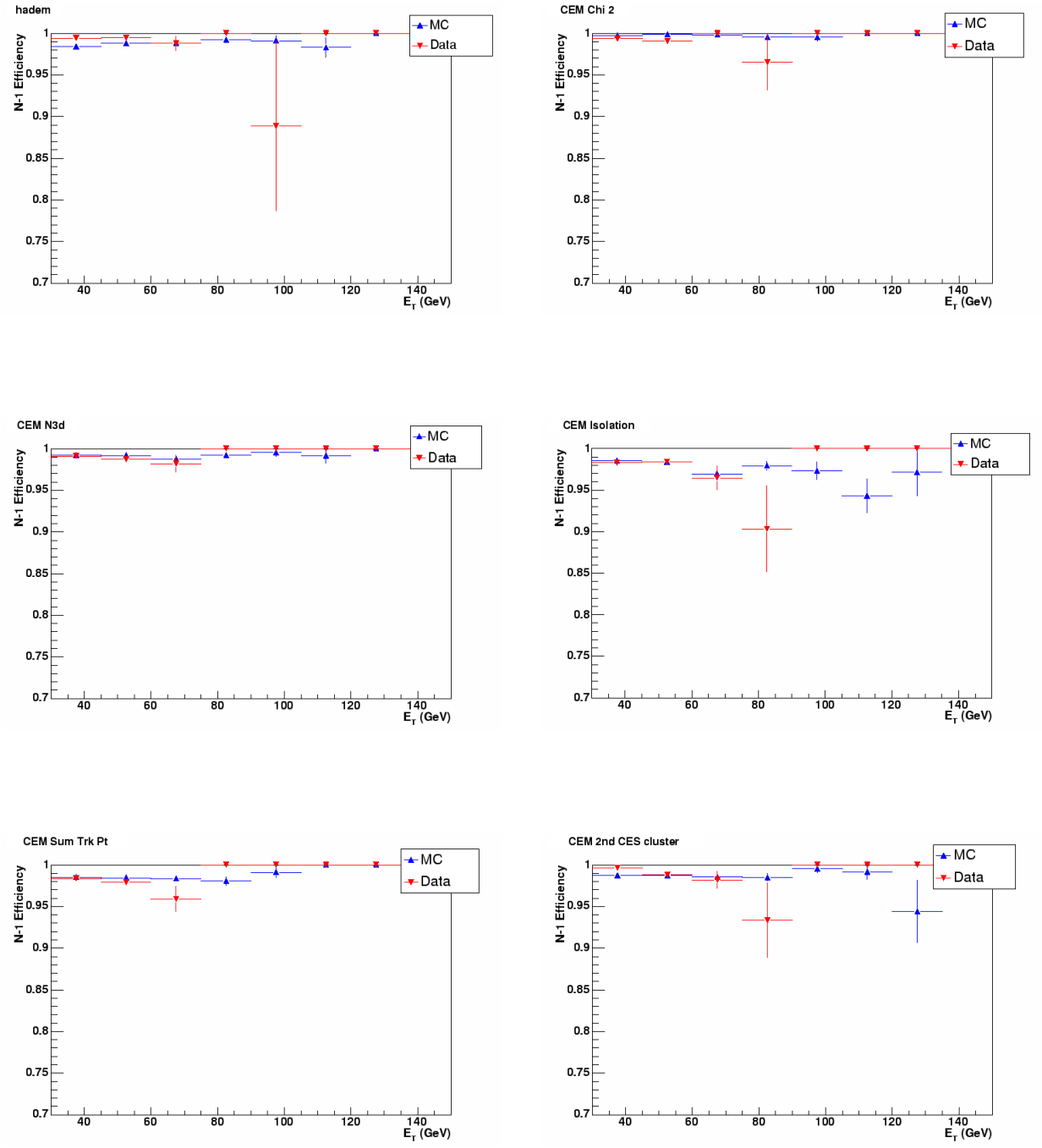

Figure 5.9: (N-1) efficiencies for central photon identification selection cuts as a function of E_T.

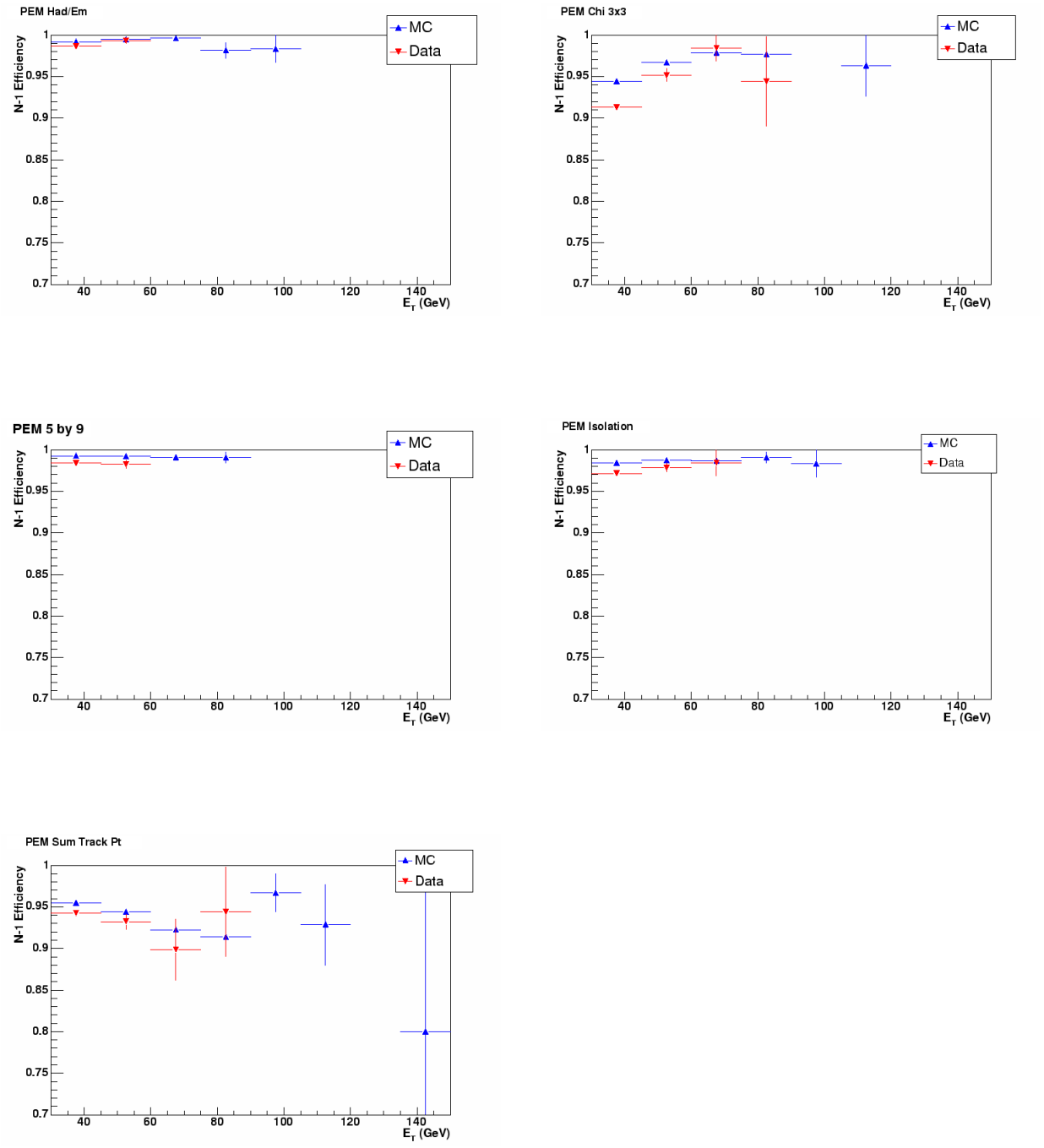

Figure 5.10: (N-1) efficiencies for plug photon identification selection cuts as a function of E_T.

5.7 Z Vertex Efficiency

The global event selection requires that the z vertex falls within ± 60 cm of the centre of the detector. The efficiency for this selection criterion has two components.

The first is to account for the fraction of events in which the interaction takes place within the ± 60 cm. The luminosity, as reported by the Cherenkov Luminosity Counter (CLC), applies to the full luminous region of the $p\bar{p}$ interactions. The fraction of events produced within 60 cm must therefore be measured. This is measured in data, as it is not well modelled in simulation. The method is described in detail in Reference [58], and uses minimum-bias data to measure the z_{vtx} distributions. It is then fitted to the $p\bar{p}$ beam luminosity function:

$$\frac{d\mathcal{L}(z)}{dz} = N_p N_{\bar{p}} \frac{1}{\sqrt{2\pi\sigma_z}} \frac{\exp(-z^2/2\sigma_z^2)}{4\pi\sigma_x(z)\sigma_y(z)} \tag{5.9}$$

where z is the z_{vtx}, $N_{p,\bar{p}}$ are the p, $\bar{p}$ fluxes and

$$\sigma_x^2(z) \simeq \frac{1}{6\pi\gamma}\beta_x(z)\epsilon_x \tag{5.10}$$

$$\sigma_y^2(z) = \frac{1}{6\pi\gamma}\beta_y(z)\epsilon_y \tag{5.11}$$

$$\beta(z) = \beta^*[1 + (\frac{z - {z_0}^2}{\beta^*})] \tag{5.12}$$

are the transverse beam widths, where β sets the scale for how the stored beam responds to a perturbation and β^* is the β-function value at the interaction point. The efficiency is found to be 96% ± 0.2% (syst) ± 0.04% (stat). To account for differences between data and simulation, the ± 60 cm requirement is removed in simulation at 500 GeV/c^2 and 800 GeV/c^2. Out of 10825 diphoton events, 10553 remain with the full z vertex selection cut

reapplied at 500 GeV/c^2, and similarly, out of 10829 events, 10557 remain at 800 GeV/c^2. This results in a 97% efficiency for the z vertex position requirement in simulation. A correction factor of (0.96/0.97) is then applied to the vertexing efficiency to take into account the difference between data and simulation. The systematic error of 0.2% is taken as the systematic uncertainty on the vertexing efficiency.

Secondly, the efficiency of the vertex reconstruction must be considered. This is measured in simulation, by removing the z vertex requirement. No additional events are selected without this additional positional information, giving a vertex reconstruction efficiency of 100%.

5.8 Photon Conversions

Photons have an approximately 10% probablility of converting in the detector, the amount of material in which is known to an accuracy of better than 10%. The uncertainty on a photon converting is therefore 1% per photon leg. As two photons, passing selection cuts, are required if the event is to be accepted, the uncertainty becomes 2%.

Chapter 6

'A Priori' Display Background

Background contamination to the $G \rightarrow \gamma\gamma$ signal arises from both Standard Model diphoton production and QCD background. The latter consists of events in which one or two of the photons in an event are 'fake', originating from a quark or gluon jet which mimicks a photon signature in the calorimeter. A small contribution also arises from e^+e^- production, where the electron tracks are not fully reconstructed. These different known sources are used to develop an *a priori* display background, comparing the number of diphoton events observed with those predicted. The details of each background calculation are discussed below.

The *a priori* background is used as an illustrative display only. To set limits in the search for a mass peak, a technique based on fitting the final signal region mass distribution to a general shape based on exponentials is used, and is described in Chapter 7.

In developing both the display background and fit to the signal region used to set limits, it is necessary to break down the central-plug (CP) sample into three η regions, with the additional boundaries set at $\eta = 1.7$ and $\eta = 2.2$, allowing the ratio of the signal to background to vary as a function of η.

6.1 Standard Model Background

The Standard Model background is calculated using *DIPHOX* [59]; a Monte Carlo generating partonic type events. All contributing processes to diphoton hadroproduction are accounted for at next-to-leading order (NLO) accuracy and are shown below in Figures 6.1 to 6.6.

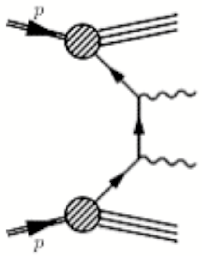

Figure 6.1: The leading order contribution to diphoton production, given by the Born level process $q\bar{q} \rightarrow \gamma\gamma$.

Figure 6.2: NLO calculations contribute $\mathcal{O}(\alpha_s)$ corrections, arising from the subprocesses $q\bar{q} \rightarrow \gamma\gamma g$, gq (or $\bar{q}$) $\rightarrow \gamma\gamma q$ (or $\bar{q}$) and corresponding virtual corrections.

One of the photons may come from the collinear fragmentation of a hard parton produced in the short distance subprocess, yielding the LO contribution of single fragmentation type (the 'Bremsstrahlung contribution'). This leads to

a final state quark-photon collinear singularity from the subprocess $gq \to \gamma\gamma q$. At higher order, final state multiple collinear singularities appear whenever a high-p_T quark or gluon undergoes a cascade of successive collinear splittings, ending up with a quark-photon splitting. These singularities are absorbed into quark and gluon fragmentation functions to a photon: $D\gamma/q$ or $g(z, M_f^2)$, as illustrated below in Figure 6.3.

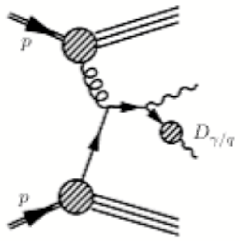

Figure 6.3: The 'Bremsstrahlung contribution', originating from the collinear fragmentation of a hard parton.

Figure 6.4: Examples of the $\mathcal{O}(\alpha_s)$ corrections to the gq (or $g\bar{q}$) initiated contributions, involving one photon from fragmentation, which are required to give a consistent treatment of NLO diphoton production.

The Standard Model NLO mass distributions for central-central and central-plug events are generated for events passing the E_T and fiducial acceptance

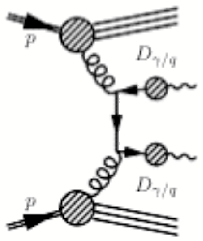

Figure 6.5: The corrections to the gq (or $g\bar{q}$) initiated contributions which yield, in their turn, the leading order contribution of the double fragmentation mechanism.

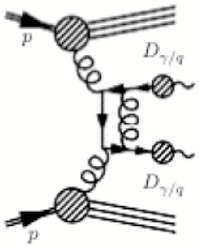

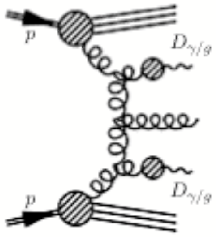

Figure 6.6: The NLO contributions from the double fragmentation contribution, where both photons result from the collinear fragmentation of a hard parton, which must be included for a full NLO calculation.

requirements. The diphoton cross-sections produced through *DIPHOX*, used to generate these distributions, are scaled by the luminosities of the central-central and central-plug datasets, respectively, and modified by a diphoton mass-dependent identification efficiency, to account for detector effects.
This mass-dependent total identification efficiency is measured using *PYTHIA* Standard Model diphoton Monte Carlo, and obtained through dividing the number of reconstructed events, which pass all selection criteria, by the number of events passing the E_T and fiducial cuts at generator level. This total efficiency is fitted to a linear function, shown in Figure 6.7, as low statistics prevent efficiency measurement at masses greater than ~ 500 GeV/c^2. This fit is then extrapolated to the high mass region and applied to the cross-section. The uncertainty from the fit translates to approximately $(0.0002 * \text{mass})$, and is shown in Figure 6.7 as the pale lines.

The central-central and central-plug mass distributions, shown in Figure 6.8, are then fitted to a general function, shown in Equation 6.1:

$$y = (x^{0.1} + \alpha_5 x^{\alpha_6})(e^{x/\alpha_0} + \alpha_1 e^{x/\alpha_2} + \alpha_3 e^{x/\alpha_4}) \tag{6.1}$$

where x is the mass minus the mass threshold cut of 30 GeV/c^2 and α_i (i = 0 to 6) are floating fit parameters. The three η channels are combined after fitting for the central-plug distribution. Figures 6.8 and 6.9, with Figure 6.9 normalized to allow for the combination of the three η regions, show these distributions, together with the fit.

6.2 QCD Background

Diphoton data events may contain one or two fake photons, originating from jets fragmenting to a hard leading π^0. These arise primarily from quark jets, carrying more energy than gluon jets, where the π^0 in the jet carries almost

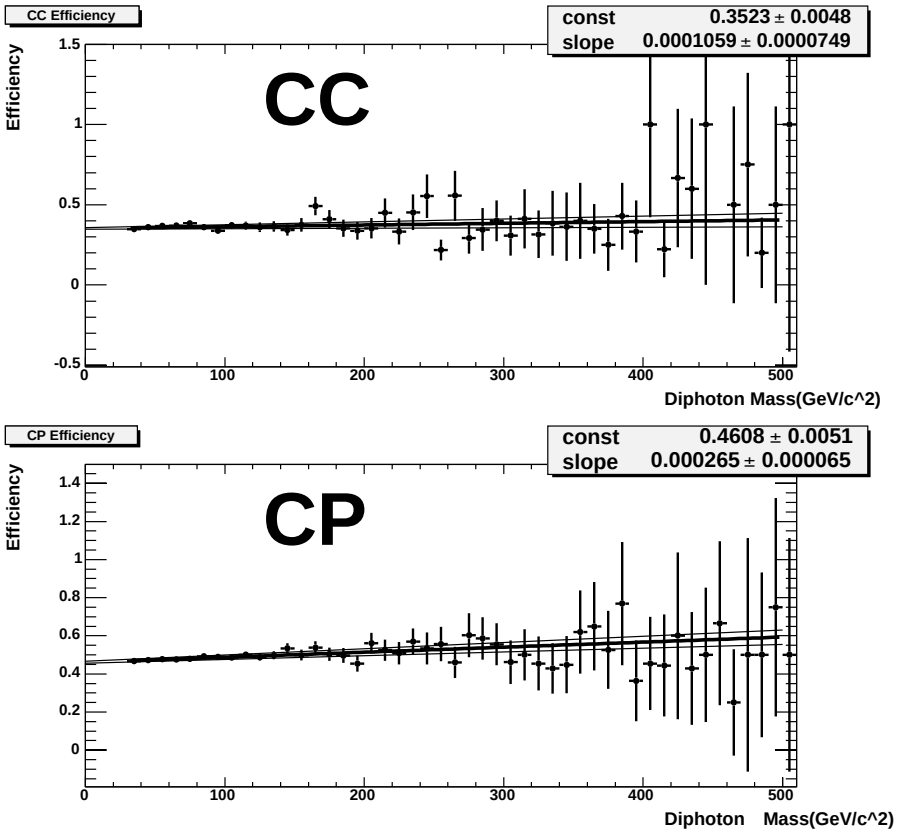

Figure 6.7: Total mass-dependent diphoton identification efficiency, measured in *PYTHIA*. A linear fit is shown (dark line), with its uncertainty (pale lines).

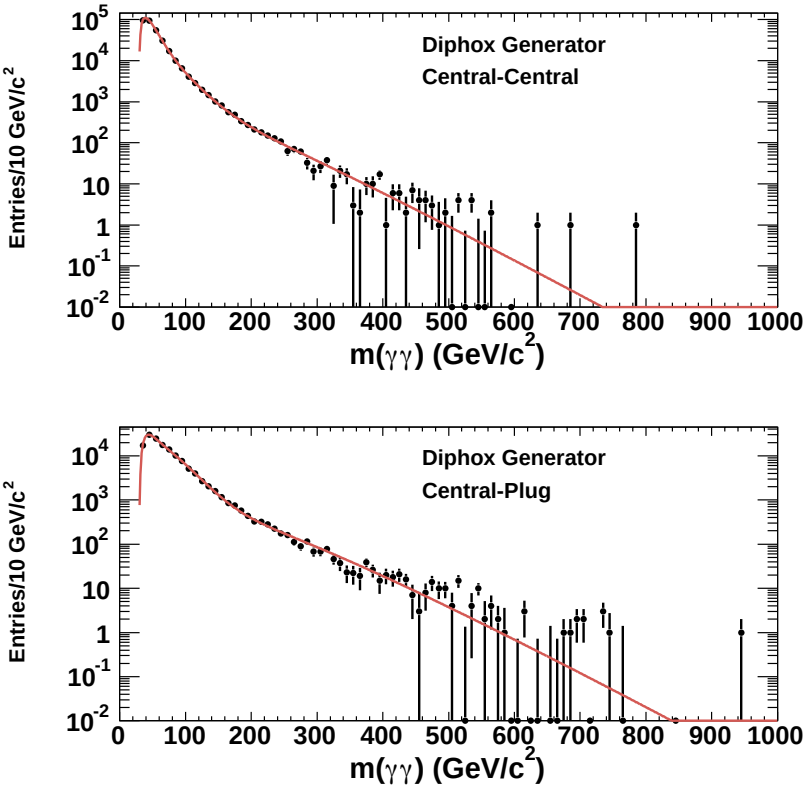

Figure 6.8: Invariant mass distribution for Standard Model diphoton production. Note that the central-plug distribution is taken from the sum of the three η regions.

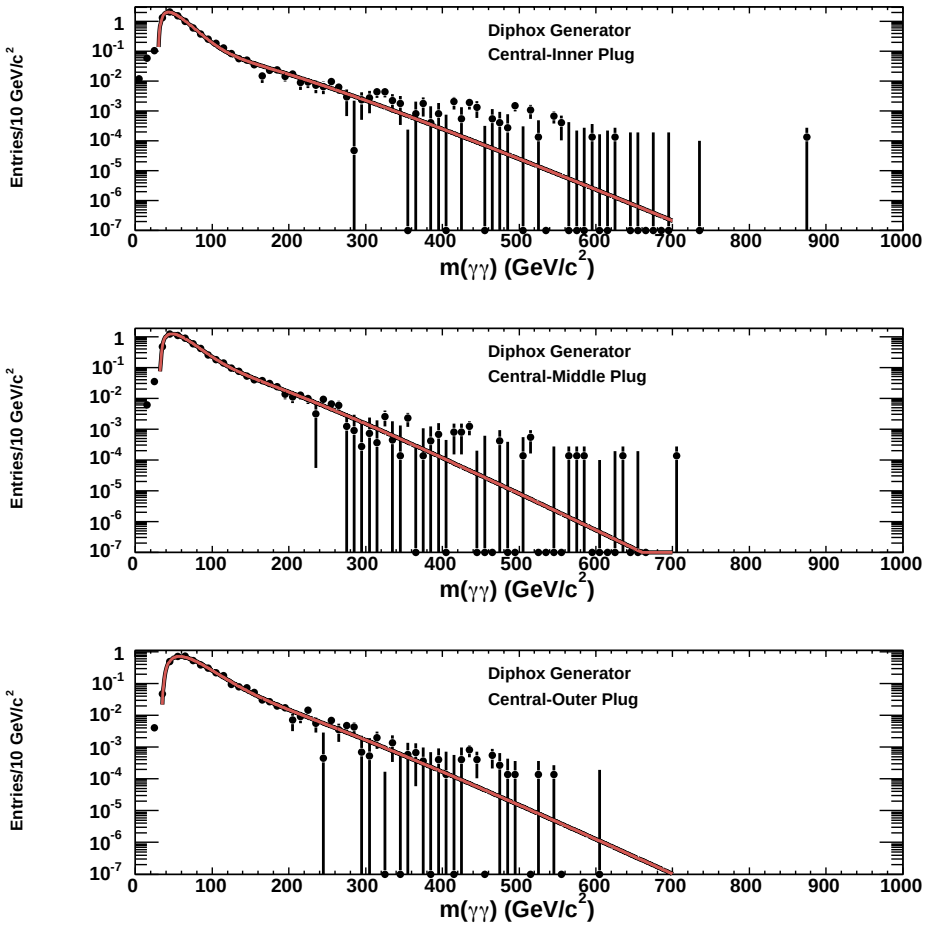

Figure 6.9: Normalized invariant mass distribution for Standard Model diphoton production for the the three central-plug η regions.

all of the jet energy. This can lead to a calorimeter signature indistinguishable from that of a single photon. To estimate the background contribution from objects faking photons, the central and plug diphoton selection criteria, as described in Tables 3.8 and 3.9 respectively, are loosened, as shown in Tables 6.1 and 6.2, and applied to the data sample. An invariant mass threshold cut of $M_{\gamma\gamma} > 30$ GeV/c^2 is also still applied.

Variable	Cut
Fiducial	Ces $\|x\| < 21$ cm, $9 <$ Ces $\|z\| < 230$ cm
E_T	> 15 GeV
E_{had}/E_{em}	< 0.125
Isolation E_T	$< 0.15 \cdot E_T$ GeV if $E_T < 20$
	$< 3.0 + 0.02 \cdot (E_T - 20.0)$ GeV if $E_T > 20$
Track p_T	$< 0.25 \cdot E_T$ GeV/c
Sum Track p_T	< 5.0 GeV/c

Table 6.1: Loose event selection for photons reconstructed in the CEM calorimeter.

Variable	Cut
Fiducial	$1.2 < \|\eta\| < 2.8$
E_T	> 15 GeV
E_{had}/E_{em}	< 0.125
Isolation E_T	$E_T < 20 :< 0.15 \cdot E_T$ GeV if $E_T < 20$
	$< 3.0 + 0.02 \cdot (E_T - 20.0)$ GeV/c if $E_T > 20$
Sum Track p_T	< 5.0 GeV/c

Table 6.2: Loose event selection for photons reconstructed in the PEM calorimeter.

Events containing two 'good' photons, which pass the original tighter selection, are then removed. The remaining events constitute what will be referred to as the 'sidebands' and provide the background estimate from QCD sources. A true diphoton event may, by chance, fail one of the signal region selection cuts, resulting in true diphoton events in the sidebands. To estimate the ratio of the number of diphoton events in the signal region to that in the sidebands, the *PYTHIA* Standard Model diphoton Monte Carlo is used. The predicted contribution to the sidebands from true diphoton events is then included using a fixed number of events from the *DIPHOX* NLO prediction for Standard Model production scaled by this ratio. To extrapolate to higher masses, the sideband distributions are fitted to the general function given in Equation 6.1, but with α_3 set to zero to improve the fit. The jet background shape is normalized to the data in the invariant mass region 30 GeV/c^2 to 100 GeV/c^2 after subtracting the estimate from Standard Model diphotons, such that:

$$\int_{30}^{100} N_{DATA} = \int_{30}^{100} N_{DIPHOX} + \int_{30}^{100} N_{SB} \tag{6.2}$$

where N_{DATA} is the number of diphoton events in the data sample, N_{DIPHOX} represents the Standard Model background and N_{SB} the QCD background. These fits are shown in Figure 6.10, for the central-central and central-plug events, with the three fits to the central-plug regions shown in Figure 6.11.

6.3 Background from e^+e^- Production

A small contribution to the background may arise from the production of e^+e^- events, where an electron fakes an isolated prompt photon in the calorimeter when it is not fully reconstructed. Electron tracks may be lost due to hard bremsstrahlung, as the electron passes through the detector material, or through failure to reconstruct a track at large η, where tracking efficiency is

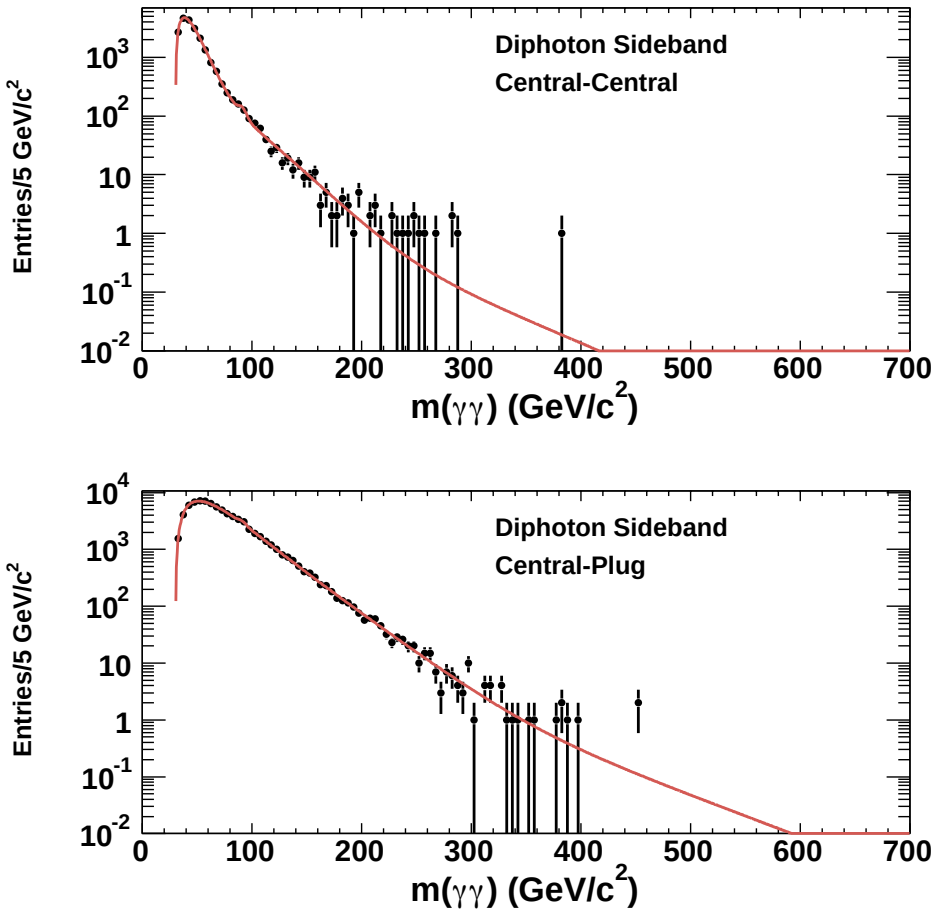

Figure 6.10: Invariant mass distribution of sideband events. The central-plug distribution is taken from the sum of the three η channels.

low. A study of the probability of a photon-like electron (an electron which passes the photon-like identification cuts as opposed to the standard tight electron cuts) to fake an isolated photon in the central calorimeter has been performed using inclusive $Z/\gamma^* \rightarrow e\gamma$ and $Z/\gamma^* \rightarrow e^+e^-$ events [60]. From this, a rate of track loss of 1% is taken. This must be applied twice to CC diphoton events, where both photons may be fakes with no reconstructed tracks, and once for CP. This gives a fake rate probability due to e^+e^- production of 0.001 for CC events and 0.01 for CP.

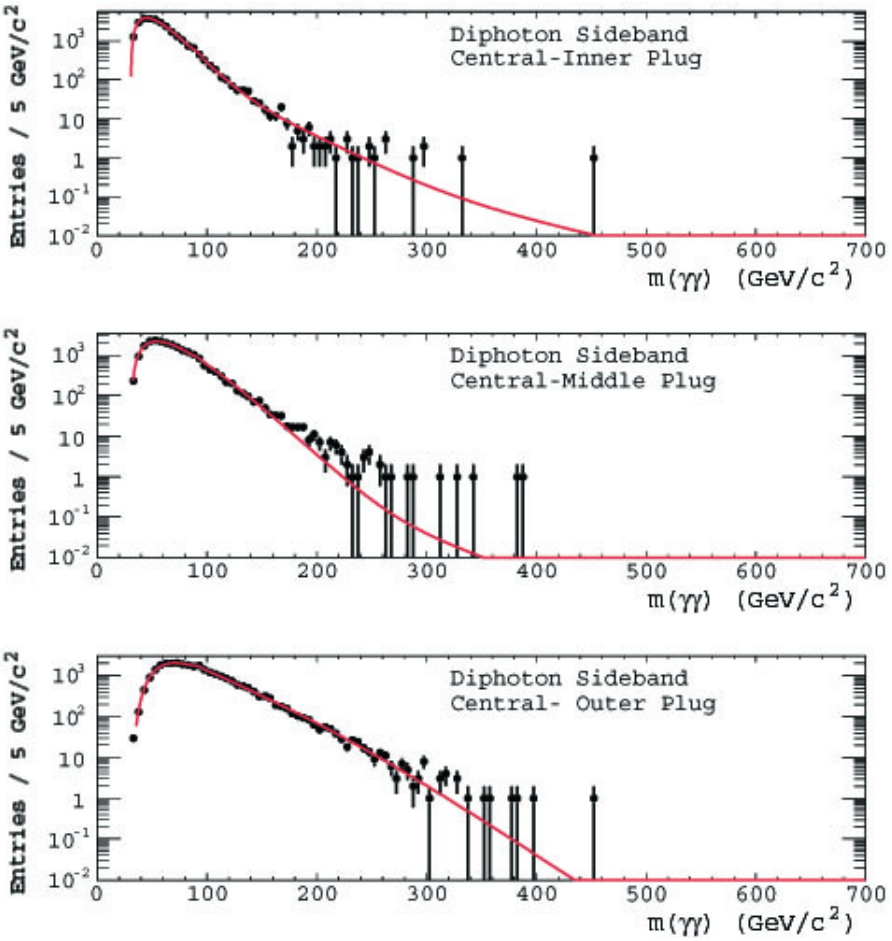

Figure 6.11: Invariant mass distribution of sideband events for the three central-plug η channels.

6.4 Background Systematic Uncertainties

These uncertainties pertain to the the display background only and are not used in setting limits.

The leading uncertainty on the *DIPHOX* prediction has three contributions. The first is from the arbitrariness in the choice of the renormalization scale. The second is from the initial state factorization scale (M), related to the parton distribution functions (PDFs) used. The third comes from the fragmentation scale (M_f), related to the quark and gluon fragmentation functions

when going to a photon, as shown in Figure 6.3 in Section 6.1, and denoted by $D_{\gamma/q}$ or $g(z, M_f^2)$. The splitting into 'direct', 'one-' and 'two fragmentation' is strongly related to the scales chosen, the two scales along the first diagonal being $M = M_f = Q/2$, where $Q = m_{\gamma\gamma}$; the invariant mass of the diphoton pair, and $M = M_f = Q * 2$. *DIPHOX* uses the MRST set of PDFs, discussed in Section 4.2.2 in Chapter 4, with the scales arbitrarily chosen to be $M = M_f = Q/2$. This choice of scale gives a 'one fragmentation' contribution that is $\sim 1/10$ the 'direct' contribution and a very small 'two fragmentation' [59]. The uncertainty on the prediction is obtained by varying the scales, using central-central diphoton events in 202 pb^{-1} of data [61]. Figure 6.12, below, shows the invariant mass distribution for Standard Model diphoton events predicted by *DIPHOX* using $M = M_f = Q/2$ and $M = M_f = Q * 2$.

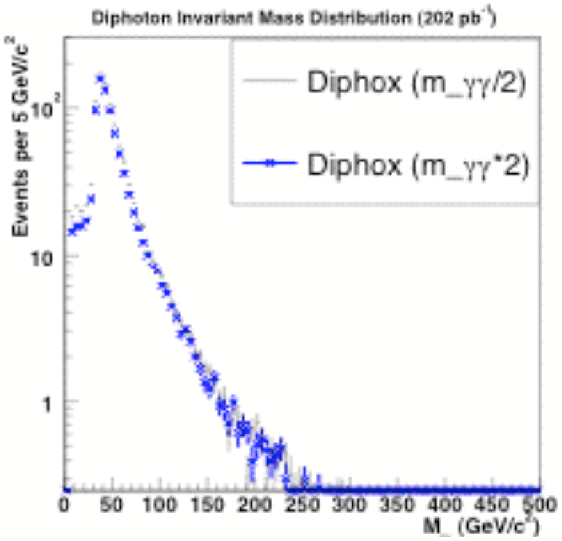

Figure 6.12: Invariant mass distribution for Standard Model diphoton events predicted by *DIPHOX* using $M = M_f = Q/2$ and $M = M_f = Q * 2$.

The systematic uncertainty is then taken as the average of the resulting percentage difference in the prediction, which is calculated at each mass point between 200 GeV/c^2 and 900 GeV/c^2 and shown, with statistical errors, in Table 6.3 [61]. An uncertainty of 20% in the prediction is taken.

M_G	Signal Window	Diphox Background		$0.5 * \Delta$Bkg/Bkg
(GeV/c^2)	(GeV/c^2)	$Q/2$	$Q * 2$	
200	184-218	3.8 ± 0.3	3.7 ± 0.3	-0.02
250	232-272	2.0 ± 0.2	1.4 ± 0.2	-0.16
300	278-328	1.6 ± 0.2	0.92 ± 0.2	-0.21
350	324-382	0.57 ± 0.2	0.35 ± 0.1	-0.19
400	370-434	0.35 ± 0.1	0.26 ± 0.1	-0.13
450	416-490	0.32 ± 0.1	0.18 ± 0.09	-0.22
500	460-544	0.20 ± 0.009	0.27 ± 0.08	0.16
550	506-598	0.16 ± 0.08	0.25 ± 0.07	0.28
600	552-652	0.14 ± 0.06	0.10 ± 0.06	-0.14
650	596-704	0.074 ± 0.05	0.03 ± 0.04	-0.30
700	642-758	0.007 ± 0.04	0.036 ± 0.03	2.00
750	684-812	0.019 ± 0.03	0.022 ± 0.03	0.07
800	732-864	0.015 ± 0.03	0.037 ± 0.02	0.74
850	776-916	0.023 ± 0.02	0.0036 ± 0.02	-0.42
900	820-968	0.02 ± 0.02	0.0029 ± 0.02	-0.43

Table 6.3: Fractional variation in *DIPHOX* prediction for central-central events using $M = M_f = Q/2$ and $M = M_f = Q * 2$.

The statistical uncertainty from the efficiency fits in Section 6.1 is also included and translates to approximately $0.0002 * \text{mass}$. The systematic uncertainties on the efficiency measurements, given in Section 5.5 in Chapter 5, are considered negligible compared to the above contributions and are therefore not included.

The uncertainties on the sideband shapes are estimated by varying the sideband cuts. The sideband is formed by loosening the signal region cuts so, for each cut, one at a time, the signal region cut is reapplied. This defines the

set of variations. A variation is also allowed where the calorimeter isolation is looser than the sideband cut:

$$\text{If } E_T < 20 \text{ then Isolation } E_T < 0.2 \cdot E_T \tag{6.3}$$

$$\text{If } E_T > 20 \text{ then Isolation } E_T < 3.5 + 0.02 \cdot (E_T - 20.0) \tag{6.4}$$

These variations are shown in Figures 6.13 and 6.14. The relative difference between the variations and the standard sideband is shown in Figure 6.15. Note that statistics are very low around 150 GeV/c^2 for central-central events and 200 GeV/c^2 for central-plug events. Events below 100 GeV/c^2 are therefore used to obtain a conservative estimate of the systematic uncertainty, which is taken as 20%, as the ratio of the sideband variations predominantly lie between ± 0.2.

6.5 Total *'A Priori'* Display Background

The total display background is shown in Figure 6.16, where the central-plug result is the combination of the three separate η channels, with the low mass region shown in greater detail in Figure 6.17.

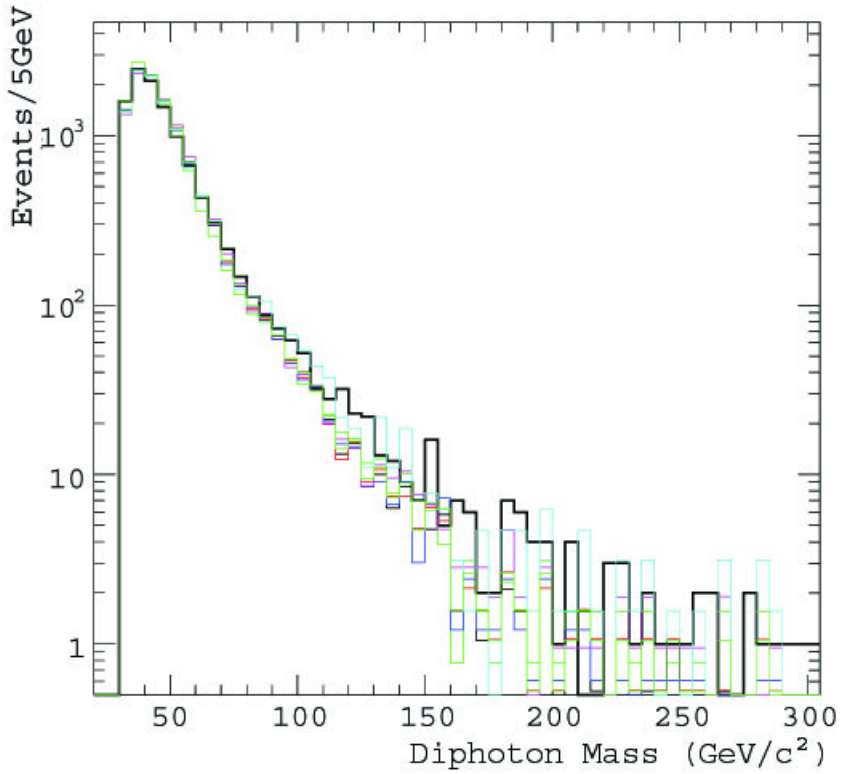

Figure 6.13: The variations of the central-central sideband mass distributions as compared to the standard sideband distribution (denoted by the thick black line).

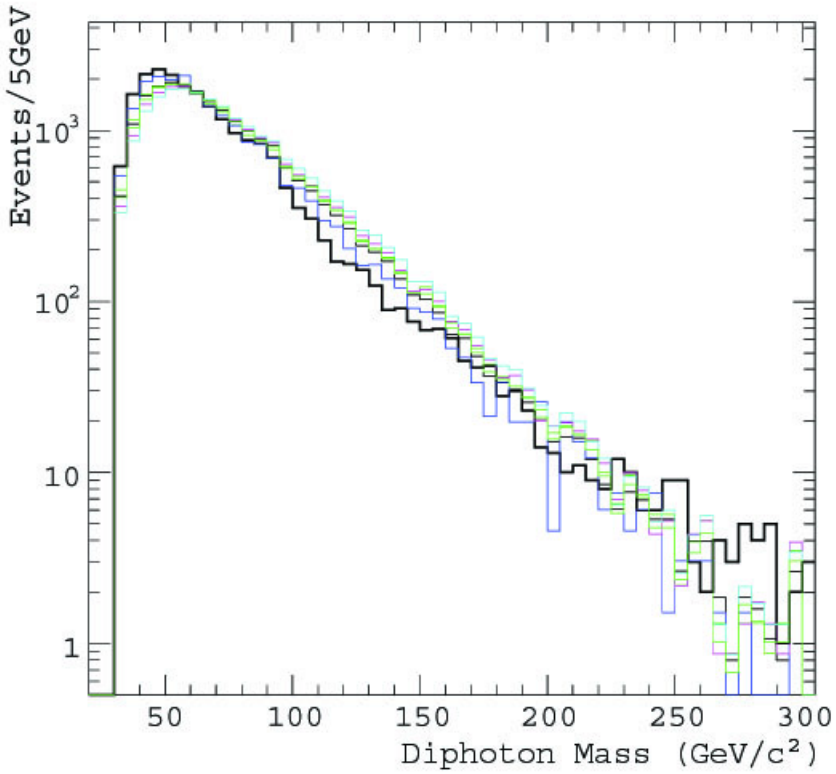

Figure 6.14: The variations of the central-plug sideband mass distributions as compared to the standard sideband distribution (denoted by the thick black line).

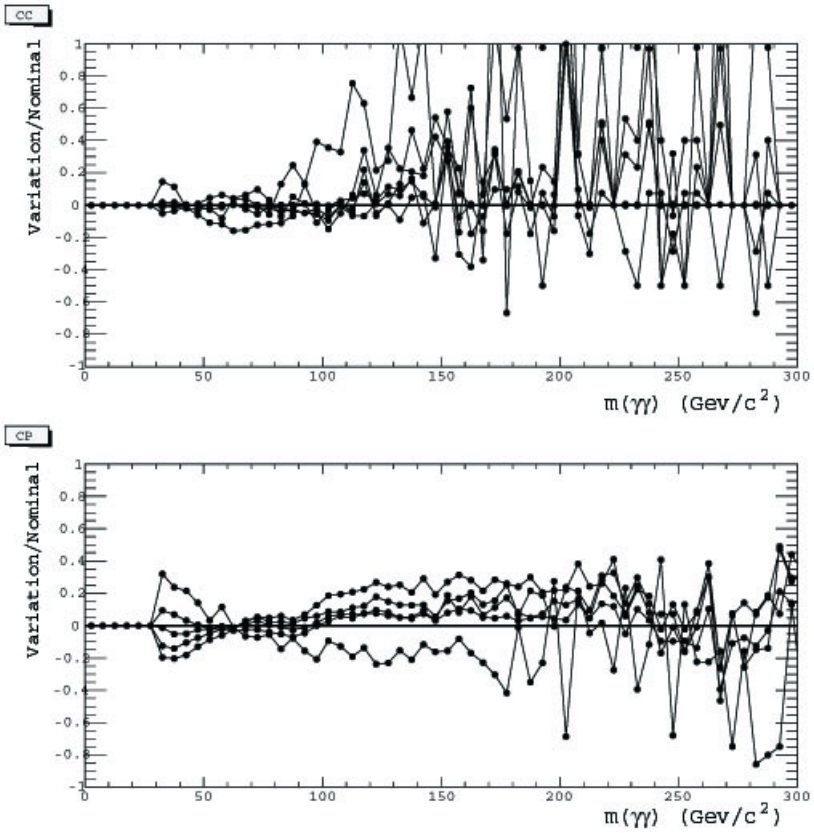

Figure 6.15: The ratio of each sideband variation to the standard sideband as a function of diphoton mass. Due to low statistics at above100 GeV/c^2, only events below this invariant mass are used to obtain the systematic uncertainty, which is taken as 20% as the ratio of the sideband variations predominantly lie between ± 0.2.

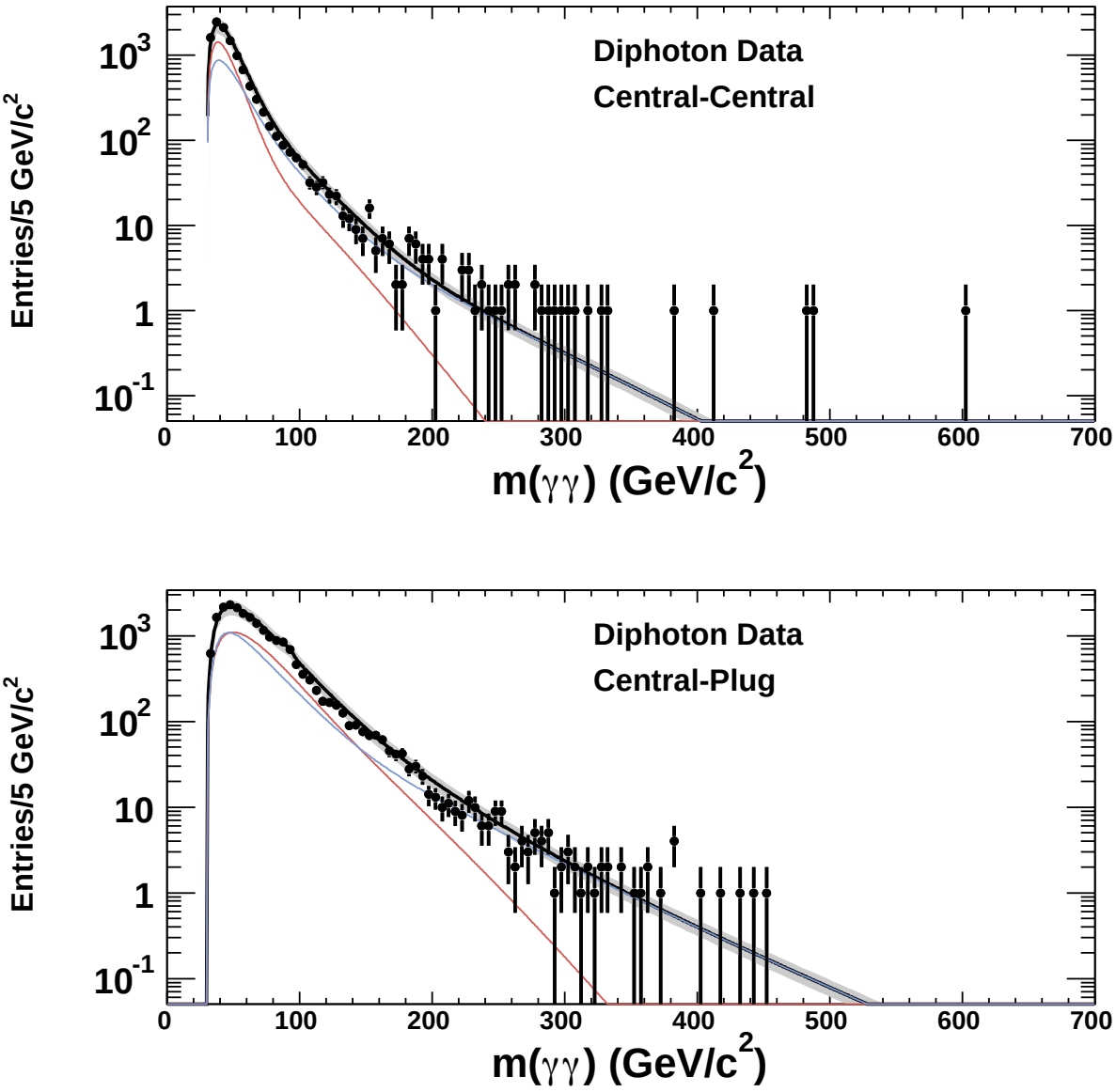

Figure 6.16: The central-central and central-plug signal region mass distributions with the *a priori* background overlayed. This background is not used in setting limits. The blue line is the *DIPHOX* true diphoton events, and the red line is the fake photons as predicted from the the sidebands.

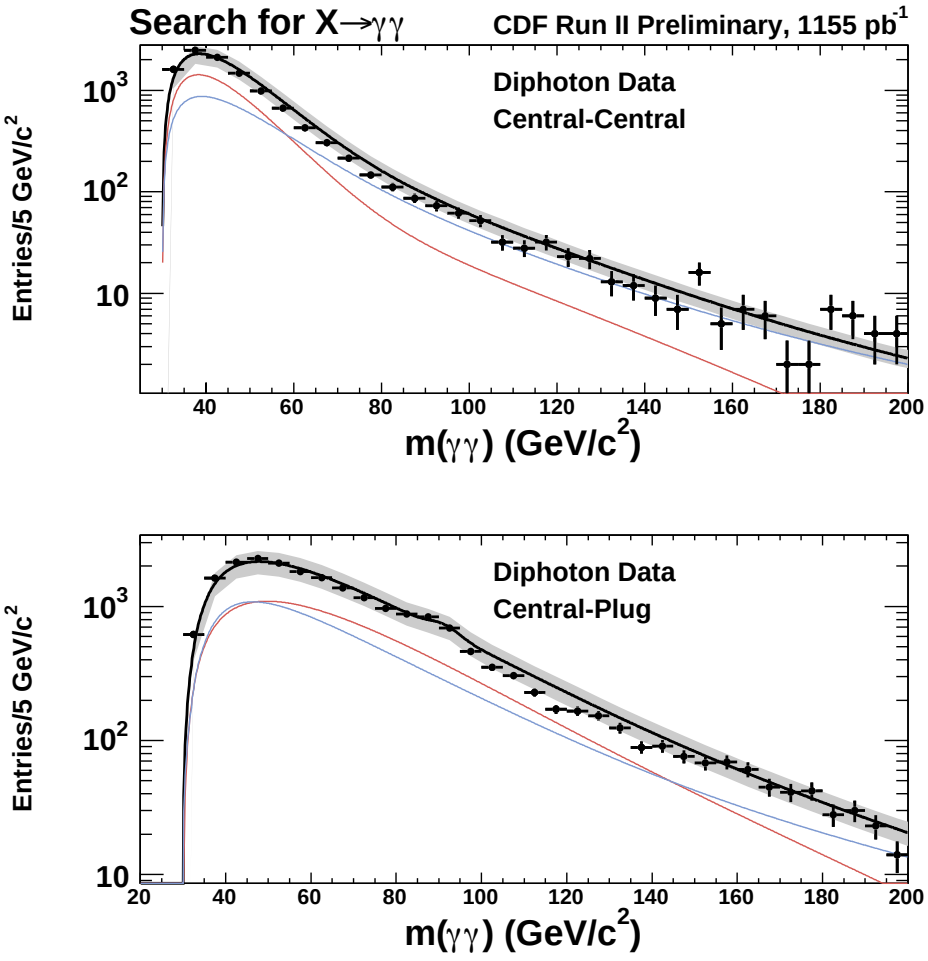

Figure 6.17: The low mass central-central and central-plug signal region mass distributions with the *a priori* background overlayed. This background is not used in setting limits. The blue line is the *DIPHOX* true diphoton events, and the red line is the fake photons as predicted from the sidebands.

Chapter 7

RS Graviton Cross-Section Limits

Through the selection of diphoton events with $M_{\gamma\gamma} > 30$ GeV/c^2, as detailed in Section 3.4, we compare the shape derived for the background with the simulated signal shape, to set upper limits on the cross-section for $\sigma \cdot BR(G \rightarrow \gamma\gamma)$, as a function of invariant mass, at a 95% confidence level (C.L.), and determine the graviton lower mass limits.

7.1 Binned Likelihood Method

The upper limits on the cross-section at the 95% C.L. (σ_{95}), as a function of invariant mass, are obtained using a binned likelihood method. This is related to the number of expected signal events (N_{95}) through:

$$\sigma_{95} \cdot BR(G \rightarrow \gamma\gamma) = \frac{N_{95}}{A \cdot \epsilon^{corr}_{trigger \times id} \int \mathcal{L} \cdot dt} \tag{7.1}$$

where A is the total signal acceptance, $\epsilon^{corr}_{trigger \times id}$ the signal efficiency and $\int \mathcal{L} \cdot dt$ is the total integrated luminosity of the data sample.

7.1.1 Likelihood Without Systematic Errors

The likelihood function is used to determine the probability of an unknown theory or hypothesis, based on known outcomes, and is formalised in Bayes' theorem [62]:

$$Pr(A|B) = \frac{Pr(B|A) \cdot Pr(A)}{Pr(B)} \tag{7.2}$$

which states that the probability of A occuring, given B, is equal to the probability of B, given A, multiplied by the probablity of A, divided by the probability of B. Here $Pr(A)$ is the *prior* or *marginal* probability, which doesn't take into account any information about B, and $Pr(B)$ is determined by the law of total probability, which is defined such that $Pr(B) = \sum_i Pr(B|A_i)P(A_i)$, where A_i are mutually exclusive and $\sum Pr(A_i) = 1$. This formula may be derived as follows: if $Pr(AB)$ is the probability that both A and B occur, then $Pr(AB) = Pr(A) \cdot Pr(B|A)$. Similarly, the probability that both B and A will occur is given by $Pr(BA) = Pr(B) \cdot Pr(A|B)$. The probability of A, given that B has occured, is thus:

$$Pr(A|B) = Pr(AB)/Pr(B) = \frac{Pr(B|A) \cdot Pr(A)}{\sum_i Pr(B|A_i)Pr(A_i)} = \frac{Pr(B|A) \cdot Pr(A)}{Pr(B)} \tag{7.3}$$

and $Pr(B|A) \cdot Pr(A)/Pr(B) \propto L(A|B)Pr(A)$, where $L(A|B)$ is the likelihood of A given fixed B. $Pr(A|B)$ is the *posterior* probability density function, as A depends upon the specified value of B. Using Equation 7.3, the *posterior* probability density function for some given theory, Φ, given the data $\mathbf{x}$, may be written as:

$$Pr(\Phi|\mathbf{x}, \nu) = \frac{L(\mathbf{x}|\Phi, \nu) \cdot Pr(\Phi)}{\int_{-\infty}^{\infty} L(\mathbf{x}|\Phi, \nu) \cdot Pr(\Phi) d\Phi} \tag{7.4}$$

with the choice of $Pr(\Phi)$ affecting the resulting value of $Pr(\Phi|\mathbf{x})$. This is taken as flat in all physically allowed regions, according to the CDF convention in the setting of limits.

We now set the theory parameter as the number of expected signal events (N^s), ν, a model dependent nuisance parameter, as the background (N^b) and $\mathbf{x}$ as the diphoton data (N^d). A Poisson probability is assigned to the data, background and signal events, as this describes the behaviour of a large number of independent experiments of which only a very small fraction is expected to yield events of a given type. The probability of there being exactly k occurrences of an event in a given time interval is given by:

$$f(k;\lambda) = \frac{e^{-\lambda}\lambda^k}{k!} \tag{7.5}$$

where λ is a positive real number, equal to the expected number of occurrences during the given interval. Letting the expected number λ be the expected number of background and signal events ($N^s + N^b$) and the number of occurences k be the number of data events (N^d), gives:

$$L(\mathbf{x}|\Phi,\nu) = L(N^d|N^s+N^b) = \frac{(N^s+N^b)^{N^d}e^{-(N^s+N^b)}}{N^d!} \tag{7.6}$$

Defining μ_i, the total predicted yield for the ith bin from both signal in the ith bin and background in the ith bin, as:

$$\mu_i = N_i^s + N_i^b \tag{7.7}$$

which may be re-written, as a function of cross-section:

$$\mu_i(\sigma) = ((A\epsilon\mathcal{L}\sigma N_i^s)/(N_{tot}^s)) + N_i^b \tag{7.8}$$

where A is the acceptance, ϵ the efficiency, $\mathcal{L}$ the luminosity and N_{tot}^s is the

total number of signal events passing selection requirements, the likelihood, as a function of cross-section, is then defined as the product of the individual probabilities for each bin,

$$L(\sigma) = \prod_{i=1}^{N} P_i(N_i^d, \mu_i) = \prod_{i=1}^{N} \frac{\mu_i^{N_i^d} e^{-\mu_i}}{N_i^d!} \tag{7.9}$$

where N is the total number of bins. The likelihood function is calculated separately for the central-central (L_{CC}) and central-plug (L_{CP}) channels. The total likelihood is then defined as:

$$L_{CC+CP} = L_{CC} \times L_{CP} \tag{7.10}$$

The upper limits on the cross-section for $\sigma \cdot BR(G \rightarrow \gamma\gamma)$ are quoted at the 95% confidence level (C.L.). This implies that the area under the $Pr(N^s|N^d, N^b)$ curve contains 95% of the total area. The upper limit is then obtained by satisfying the following relation:

$$\int_{-\infty}^{\sigma_{95}} P(N^s|N^d, N^b) = \frac{\int_{-\infty}^{\sigma_{95}} L(N^d|N^s + N^b)P(N^s)dN^s}{\int_{-\infty}^{\infty} L(N^d|N^s + N^b)P(N^s)dN^s} = \frac{\int_0^{\sigma_{95}} L(\sigma)d\sigma}{\int_0^{\infty} L(\sigma)d\sigma} = 0.95 \tag{7.11}$$

7.1.2 Likelihood Incorporating Systematic Errors

The method for incorporating the systematic uncertainties, discussed in the previous chapters and summarized below, is detailed in this section.

Summary of Systematic Uncertainties

- Luminosity (Section 2.2.5)
- Z vertex (Section 5.7)

- Energy scale (Section 4.2.1)
- Efficiency correction factors (Section 5.2.1)
- Parton distribution function (Section 4.2.2)
- Initial and final state radiation (Section 4.2.3)
- Photon conversions (Section 5.8)
- Background fit (Sections 6.4 and 7.2)

Systematic errors are included through smearing the likelihood as a function of the cross-section. Each of the above systematic uncertainties is assumed to take a Gaussian form and is treated as resulting in an uncertainty in the estimation on the actual cross-section. A one standard deviation systematic variation is then turned into a corresponding shift in the estimate of the cross-section; $\Delta\sigma$. Pure cross-section errors translate directly to an uncertainty on the cross-section. For example, a 6% uncertainty on the luminosity translates to a 6% uncertainty in the estimate of the cross-section. Integrating over all possible cross-sections, weighted by the Gaussian with a mean and standard deviation equal to the given cross-section and the error on that cross-section, then gives:

$$L^{smear}(\sigma) = \int_0^\infty L(\sigma') \frac{e^{-\frac{(\sigma'-\sigma)^2}{2\Delta\sigma^2}}}{\sqrt{2\pi\Delta\sigma^2}} d\sigma' \tag{7.12}$$

The ratio of cross-section and shift should then, in this case, be a constant that is equal to the relative error $(\frac{\Delta\sigma}{\sigma})$ = constant. Uncertainties affecting the background, however, will not simply translate to an error on the cross-section but will result in an absolute error ($\Delta\sigma$ = constant). These may also affect the signal and distribution of the data. In this case the smearing required is determined using simulation. Each error is varied by $\pm$ one standard

deviation, giving two new background and signal histograms. These are used as templates for generating 1000 pseudo-experiments for each mass point, with a signal normalisation corresponding to a cross-section of 1 pb. Each of these is then fitted using the likelihood defined in Equation 7.9. This gives the most likely value of the cross-section using the fluctuated signal and background histograms as templates. This is then repeated with the nominal signal and background histograms and the difference between the averages of the two cross-sections is taken as the error on the cross-section. The uncertainty on this error is obtained by repeating the process with the signal normalisations for cross-sections of 2, 3, 4 and 5 pb and then fitting the distribution with a linear function, which is used to obtain $\Delta\sigma$.

7.2 Background

The background prediction, used to set the limits, is obtained through fitting the central-central and central-plug mass spectra to a polynomial multiplied by a sum of two exponentials, as used for the *a priori* background and given in Equation 6.1, with α_3 set to zero and floating the shape from the *DIPHOX* contribution. The resulting fit is shown in Figure 7.1. Figure 7.2 shows the integral of the limit fit, showing the integral of the data from point m($\gamma\gamma$) to infinity, compared to the integral of the background fit.

As a general function is applied to the data to describe the background distribution, a 5 event graviton signal is subsequently inserted, as a test, with an invariant mass of 600 GeV/c^2, to ensure that any excess due to a signal will not perceptibly change the background fit, thereby potentially masking a signal. Figure 7.3 shows the effect on the background distribution in the central-central and central-plug channels, refitted with the signal events included, showing that the excess remains clearly visible above the background.

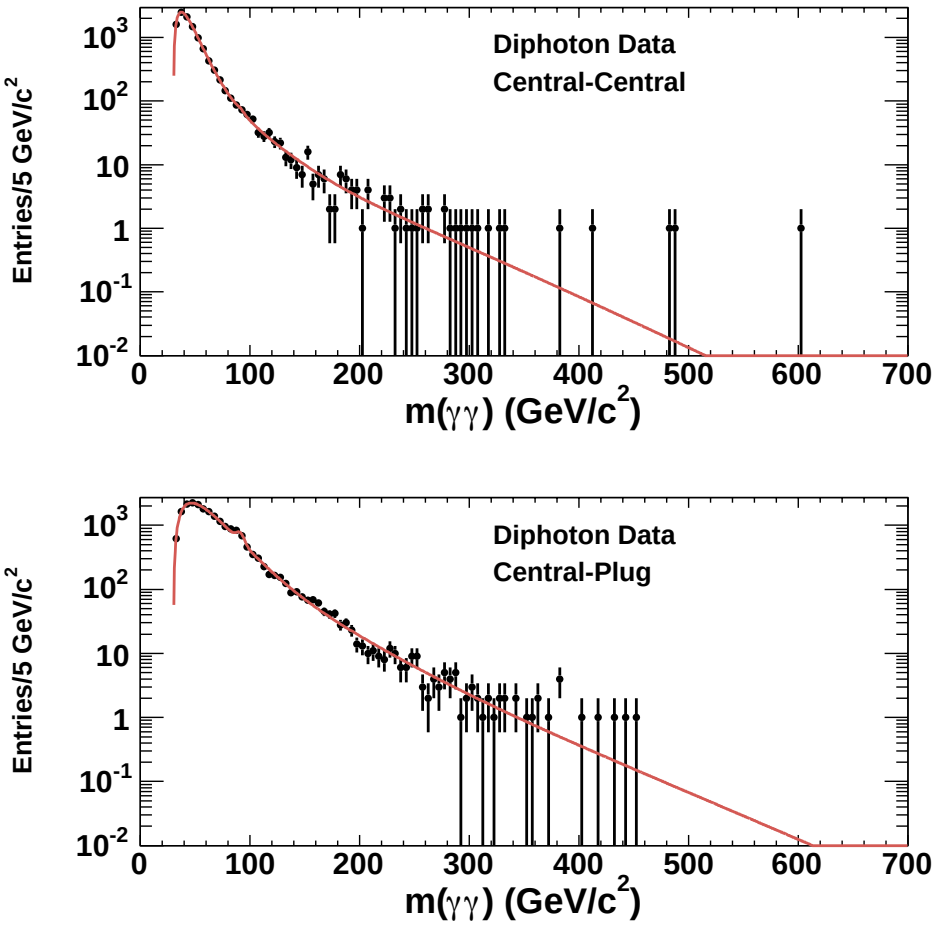

Figure 7.1: The central-central and central-plug signal region mass distributions with the background fit overlayed.

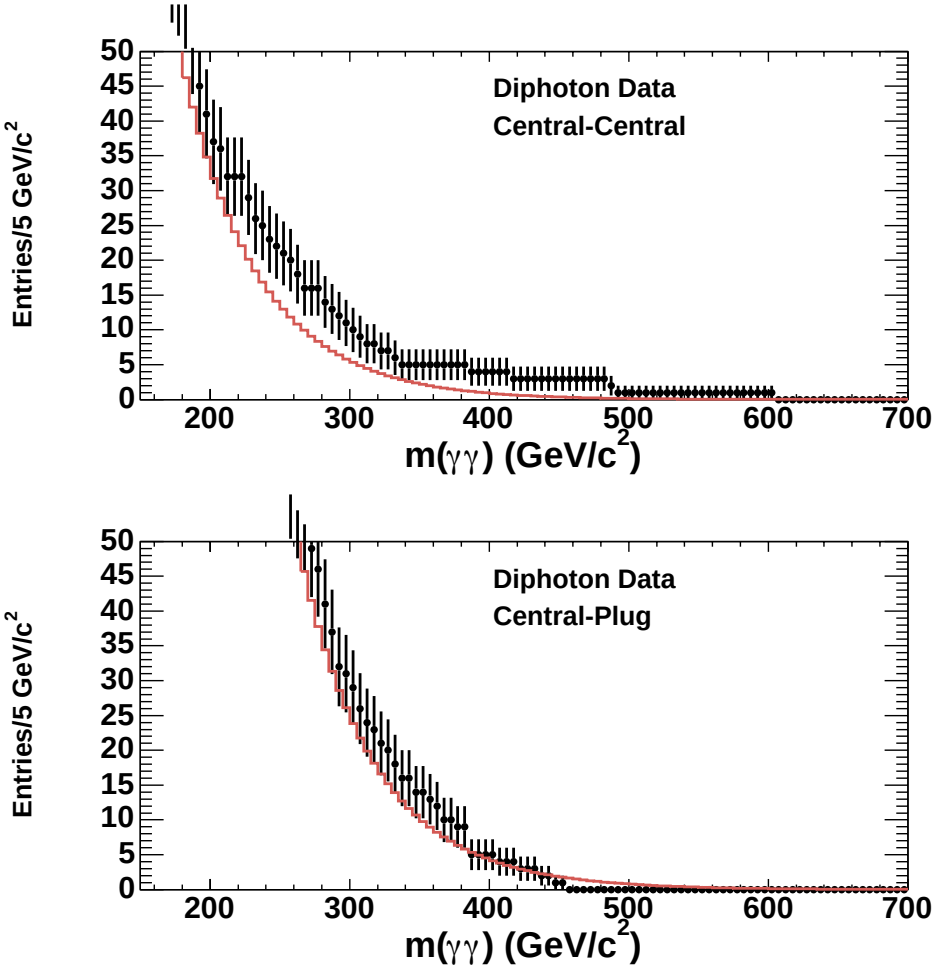

Figure 7.2: The central-central and central-plug signal region mass distributions with the integral of the background from the limit fit overlayed.

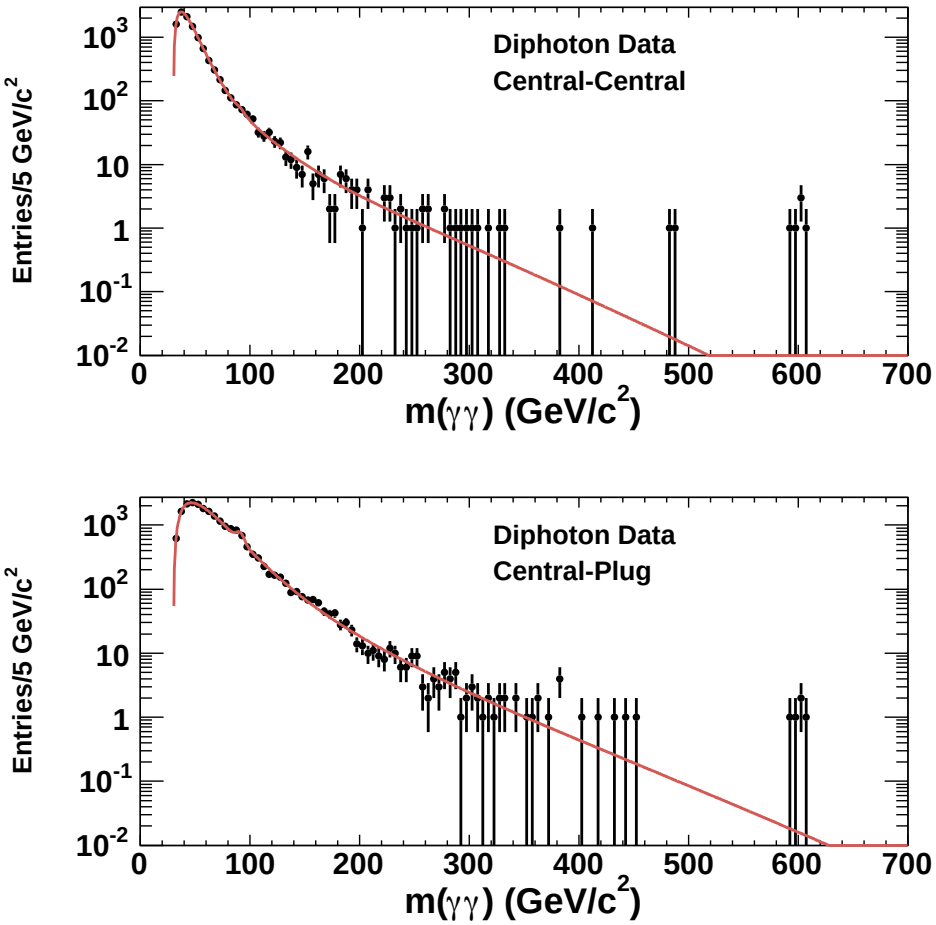

Figure 7.3: The central-central and central-plug invariant mass distributions, showing the background fit with 5 signal events inserted at 600 GeV/c^2. The excess remains clearly visible above the background.

7.3 Theoretical Cross-Section

The leading order theoretical cross-section, with $k/\overline{M}_{Pl} = 0.1$, is generated using *HERWIG* Monte Carlo, with graviton masses in the range 200 GeV/c^2 to 1050 GeV/c^2, as discussed in Chapter 4. The theoretical cross-sections with widths 0.07, 0.05, 0.025 and 0.01 are then obtained by scaling that for $k/\overline{M}_{Pl} = 0.1$. All cross-sections are corrected by a flat multiplicative K-factor; K_f, described below.

7.3.1 K-Factor

HERWIG calculates the LO cross-sections for RS graviton production. A higher order QCD correction, predominantly arising from initial state radiation, must then be applied. For the Tevatron, the K-factor for graviton-induced processes does not substantially deviate from the Standard Model value, with its inclusion being necessary to make the cross-section stable with respect to scale variations, giving a correction factor of $K_f = 1.3$ [63].

7.4 Limits

The upper limits are presented here for the central-central and central-plug channels, with likelihoods calculated separately. These are then multiplied together to give a combined likelihood. This is then integrated up to 95% of the total integrated likelihood to obtain the 95% CL limit. All values with theoretical cross-section greater than the upper limit on the experimental cross-section are then excluded.

7.4.1 Cross-Section Limits without Systematic Errors

Figure 7.4 shows the 95% CL upper limits, without systematic errors, for $\sigma \cdot BR(G \rightarrow \gamma\gamma)$, for the separate central-central and central-plug channels. Figure 7.5 shows the limit for both channels combined. As described in Section 7.1.2, 1000 pseudo-experiments are performed to enable the limits to be compared to the expected values if there were only background present. These are generated for each graviton mass, taking the median of the limits obtained at each mass point as the expected limit for that graviton mass. The observed limit is shown together with the expected limit for each plot. The 1, 2 and 3σ bands are also shown and indicate the upper and lower limits on the expected limit such that 68.3%, 95.4% and 99.7% respectively of the pseudo-experiments give limits that are within this range.

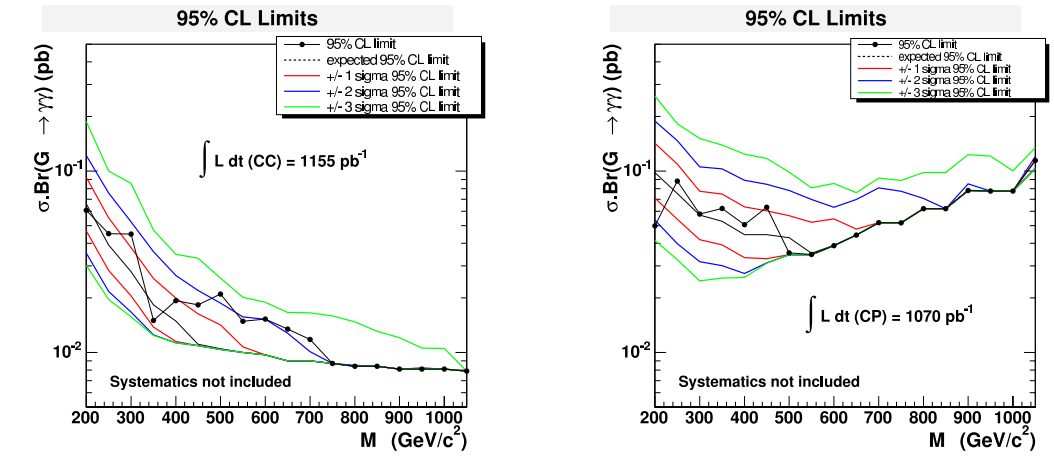

Figure 7.4: The 95% CL upper limit for $\sigma \cdot BR(G \rightarrow \gamma\gamma)$, as a function of graviton mass, for data in the central-central channel, shown on the left, and the central-plug, shown on the right, together with the expected limits from the pseudo-experiments. No systematic errors are included.

7.4.2 Cross-Section Limits with Systematic Errors

Figure 7.6 shows the 95% CL upper limits, with full systematic errors included, for $\sigma \cdot BR(G \rightarrow \gamma\gamma)$, for the separate central-central and central-plug channels.

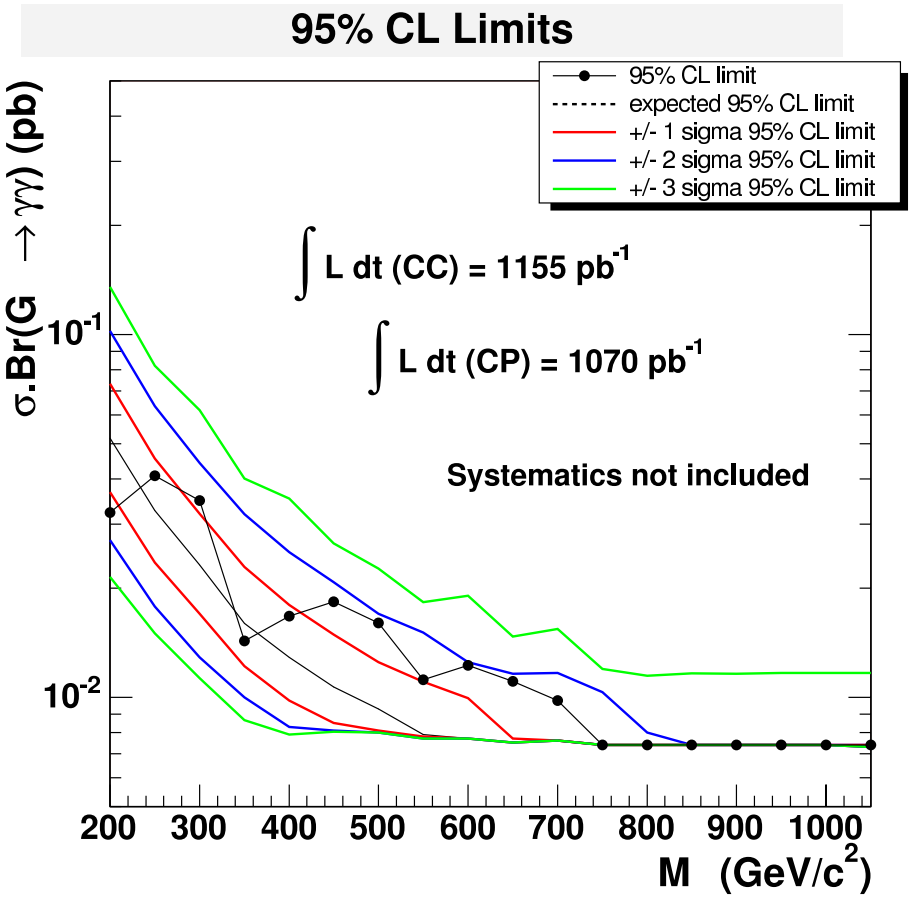

Figure 7.5: The 95% CL upper limit for $\sigma \cdot BR(G \rightarrow \gamma\gamma)$, as a function of graviton mass, for data in the central-central and central-plug channels combined, together with the expected limits from the pseudo-experiments. No systematic errors are included.

Figure 7.7 shows the limit for both channels combined. The limits without systematic errors are included for comparison.

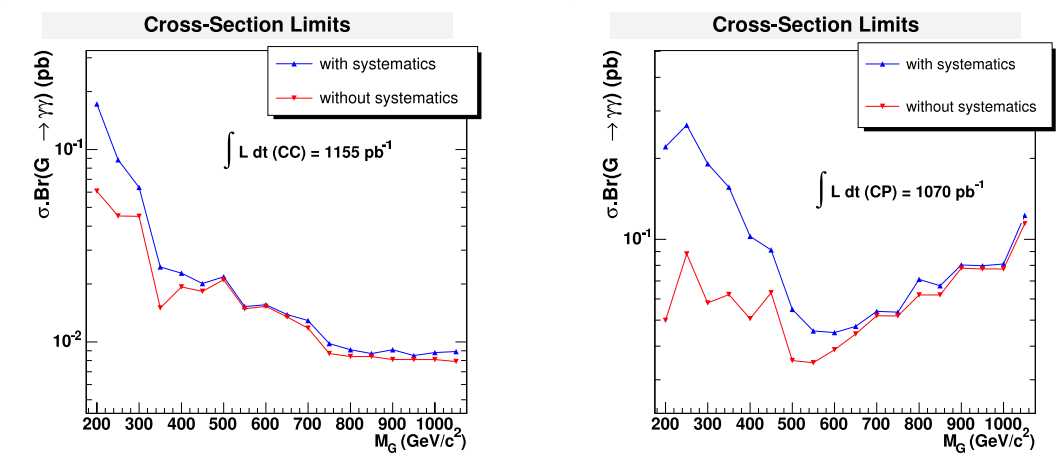

Figure 7.6: The 95% CL upper limit for $\sigma \cdot BR(G \rightarrow \gamma\gamma)$, as a function of graviton mass, for data in the central-central channel, shown on the left, and the central-plug, shown on the right. Full systematic errors are applied. The limit without systematics is also shown for comparison.

7.4.3 Lower Mass Limits and 2-Dimensional Exclusion Domain

The 95% CL upper limit (σ_{95}) on the experimental cross-section for $\sigma \cdot BR(G \rightarrow \gamma\gamma)$, as a function of graviton mass, is shown in Figure 7.8, together with the theoretical cross-sections for values of $k/\overline{M}_{Pl}$ of 0.01, 0.025, 0.05, 0.07 and 0.1.

The 95% CL lower limits on the mass on the RS graviton are determined by the position of the intersection of the theoretical cross-sections, for their respective production, and the limit on the cross-section times branching ratio, as shown in Figure 7.8. These are shown in Table 7.1 for values of $k/\overline{M}_{Pl}$ of 0.1, 0.07, 0.05, 0.025 and 0.01.

The 95% CL exclusion domain, in the plane of $k/\overline{M}_{Pl}$ versus graviton mass, is shown in Figure 7.9 for values of $k/\overline{M}_{Pl}$ in the range $0.01 < k/\overline{M}_{Pl} < 0.1$.

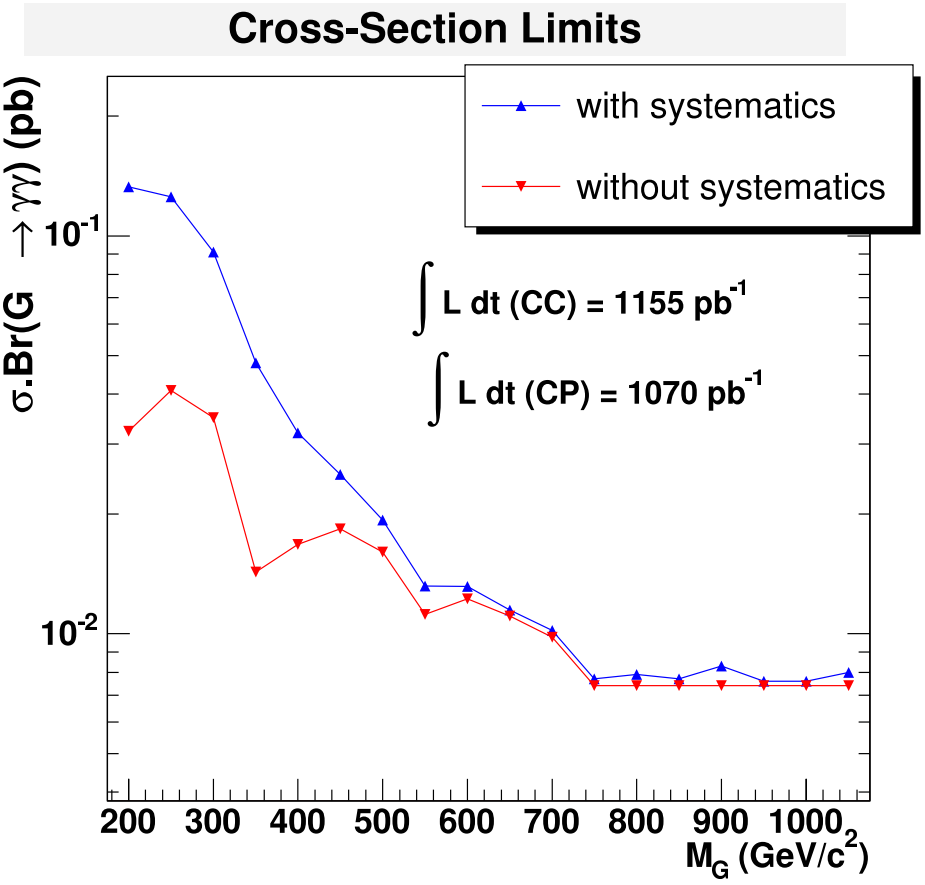

Figure 7.7: The 95% CL upper limit for $\sigma \cdot BR(G \rightarrow \gamma\gamma)$, as a function of graviton mass, for the central-central and central-plug channels combined. Full systematic errors are applied. The limit without systematics is also shown for comparison.

These results have been further improved through combining with the di-electron channel, as detailed in Appendix C, to give the current most exclusive limits on the Randall-Sundrum model.

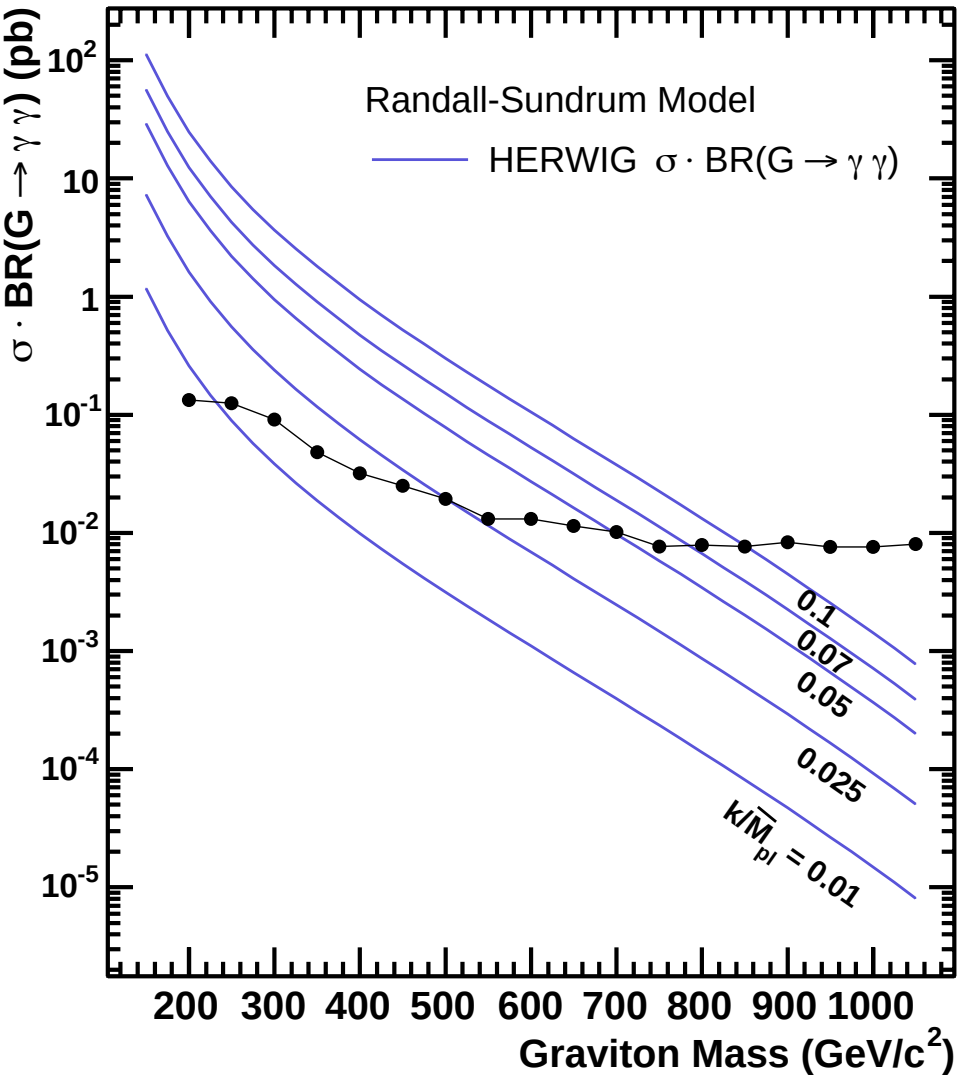

Figure 7.8: 95% CL upper limit on the production cross-section times branching fraction of an RS graviton decaying to two photons ($\sigma \cdot BR(G \rightarrow \gamma\gamma)$), as a function of graviton mass, with full systematic errors applied. The predicted ($\sigma \cdot BR$) curves for $k/\overline{M}_{Pl} = 0.01$, 0.025, 0.05, 0.07 and 0.1 are also shown.

$k/\overline{M}_{Pl}$	Lower Mass Limit (GeV/c^2)
0.1	850
0.07	784
0.05	694
0.025	500
0.01	230

Table 7.1: The 95% CL lower limits on the mass on the RS graviton for $0.01 < k/\overline{M}_{Pl} < 0.1$.

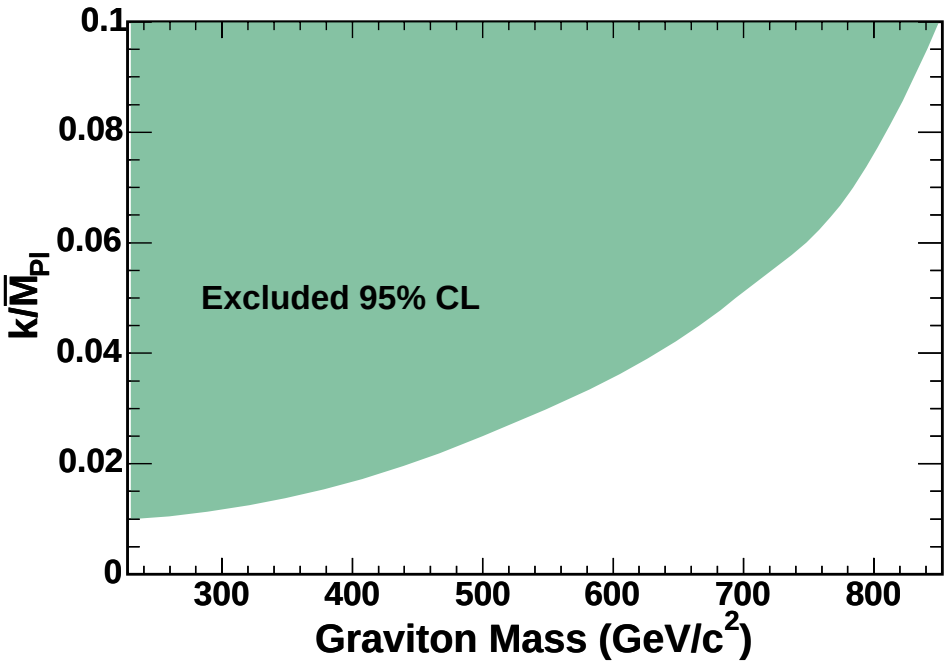

Figure 7.9: 95% CL exclusion domain in the plane of $k/\overline{M}_{Pl}$ versus graviton mass, for an integrated luminosity of 1155 pb^{-1} for central-central decays and 1070 pb^{-1} for central-plug decays.

Chapter 8

Summary

A search for Randall-Sundrum gravitons in the diphoton decay channel is performed using 1.2 fb^{-1} of data, collected by the Collider Detector at Fermilab between February 2002 and February 2006.

The Randall-Sundrum model proposes a solution to the Hierarchy problem through the modification of gravity, with the geometry of an extra spatial dimension being responsible for the apparent weakness of gravity in relation to the other fundamental forces in nature. It is detectable in colliders through the process of virtual graviton exchange, its signature being a series of narrow heavy graviton resonances, visible as an excess of events leading to an overall modification of the cross-section and angular distribution at high invariant mass. In this analysis, only the invariant mass spectrum is studied, due to the low statistics at high invariant mass. It improves on previous diphoton channel searches through the inclusion of CDF's two plug calorimeters, resulting in greater angular coverage, in addition to the availability of a larger integrated luminosity.

To predict the expected number of signal events, the acceptance and efficiency are measured. The acceptance takes geometric and kinematic effects into account and is measured using simulated data. The efficiency comes from the

probability that an event containing two photon candidates will pass the online trigger, measured using data, and that the photon candidates will subsequently pass the identification cuts. This identification efficiency is also measured in simulation, and is corrected for variations between data and detector simulation using $Z \rightarrow ee$ events. The predicted number of events, given by the cross-section times the integrated luminosity, is then scaled by the product of the acceptance and efficiency.

Background to the $G \rightarrow \gamma\gamma$ signal arises from both Standard Model diphoton production and QCD background, where a quark or gluon jet mimicks a photon signature. A small contribution also arises from e^+e^- production, where the electron tracks are not fully reconstructed. These different known sources are used to develop and fit an *a priori* display background, comparing the number of diphoton events observed with those predicted. As the diphoton mass spectrum shows no excess of events that would indicate a graviton resonance, a shape is derived for the background through a fit to the diphoton mass spectrum based on that from the *a priori* background, and is compared with the simulated signal shape. A Bayesian binned likelihood method is then used to set upper limits on the cross-section for $\sigma \cdot BR(G \rightarrow \gamma\gamma)$, as a function of invariant mass, at a 95% confidence level, as shown in Figure 8.1, together with the predicted cross-sections for $k/\overline{M}_{Pl} = 0.01$, 0.025, 0.05, 0.07 and 0.1.

The exclusion region in the parameter space of graviton mass and coupling parameter $k/\overline{M}_{Pl}$ is then derived, for values in the range $0.01 < k/\overline{M}_{Pl} < 0.1$, with lower mass limits of 230 GeV/c^2 and 850 GeV/c^2 obtained for $k/\overline{M}_{Pl} =$ 0.01 and 0.1, respectively, as shown in Figure 8.2.

In addition to further analyses at the Tevatron collider, the Large Hadron Collider at CERN, due to start data taking in 2008, will add sensitivity to the search through its higher centre-of-mass energy of 14 TeV . At these energies, the gravitational effects will become comparable to electroweak effects,

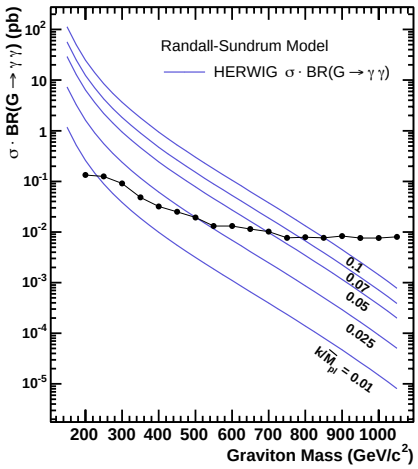

Figure 8.1: 95% CL upper limit on the production cross-section times branching fraction of an RS graviton decaying to two photons ($\sigma \cdot BR(G \rightarrow \gamma\gamma)$), as a function of graviton mass, with full systematic errors applied. The predicted ($\sigma \cdot BR$) curves for $k/\overline{M}_{Pl} = 0.01$, 0.025, 0.05, 0.07 and 0.1 are also shown.

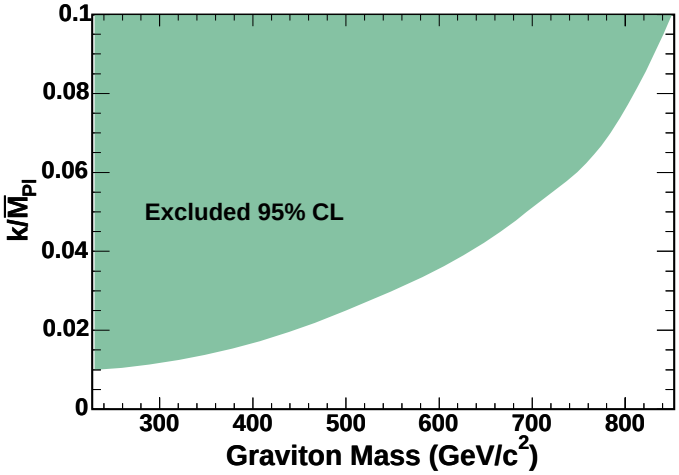

Figure 8.2: 95% CL exclusion domain in the plane of $k/\overline{M}_{Pl}$ versus graviton mass, for an integrated luminosity of 1.2 fb^{-1}.

allowing gravitons to be produced as copiously as photons.

Appendix A

Plug Electron Rejection and Plug Tracking Efficiencies

A.1 Electron Rejection Factors

The electron rejection factor is defined as the number of electrons passing selection criteria with no tracking requirement, divided by the number passing with all ID criteria applied. It is calculated using both the Phoenix and Silicon Standalone tracking in the plug, using simulated $Z \rightarrow ee$ events, for photon selection optimisation.

Plug electrons are selected using central-plug events around the Z pole, with an invariant mass in the range 81 GeV/c^2 < M_{ee} < 101 GeV/c^2. The emulated central photon selection cuts, described in Section 5.2.1, are placed on the central electron. The plug electron is then required to pass emulated plug cuts with the tracking requirement removed. The number of events passing are then divided by the number of events passing with the tracking cut (either Phoenix or Standalone) applied to the plug electron. The electron rejection factors are shown in Table A.1.

Plug electron rejection optimisation is also studied in data, using a second

Tracking Requirement	Number of Events Passing	Rejection Factor
No Tracking	175276	-
Phoenix Cut	45341	3.87
Silicon Standalone Cut	83386	2.10
Combined	42387	4.14

Table A.1: Plug electron rejection factors calculated using simulated $Z \rightarrow ee$ events.

method, to complement the simulation study. The photon selection criteria, with no plug tracking requirement, are applied to select plug-plug diphoton events in data, from which the invariant mass spectrum is obtained. A Gaussian distribution is then fitted to the integral around the Z pole (81 GeV/c^2 $< M_{\gamma\gamma} <$ 101 GeV/c^2), as shown in Figure A.1. Plug tracking is then applied, using Phoenix and Silicon Standalone in turn, and the integral recalculated. The integral values are then used to calculate the electron rejection factors, shown in Table A.2.

Tracking requirement	Integral around Z pole	Rejection factor
no tracking	33057.40	
Phoenix (nHit < 3)	4393.09	7.52
standalone (SumPt4 $< 2 + 0.005 *$ Etc)	9057.34	3.65

Table A.2: Plug electron rejection factors calculated in data.

The higher electron rejection factor is obtained through the Phoenix tracking, with the combination of both tracking algorithms providing optimum rejection.

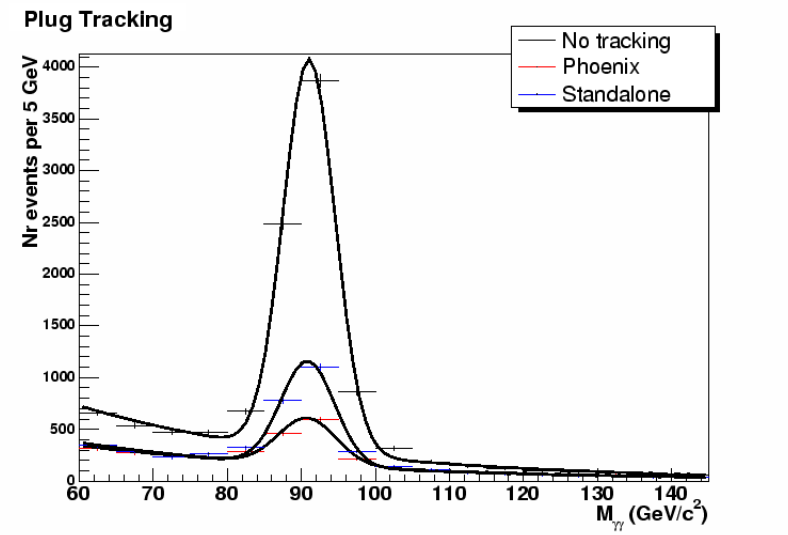

Figure A.1: Diphoton invariant mass

A.2 Phoenix and Silicon Standalone Tracking Efficiencies

The Phoenix and Standalone tracking efficiencies cannot currently be measured for photons using this framework, as a Phoenix track is required for this measurement. For completeness, the (N-1) efficiencies of the two tracking algorithms are shown for electrons as a function of η, in Figures A.2 and A.3 respectively.

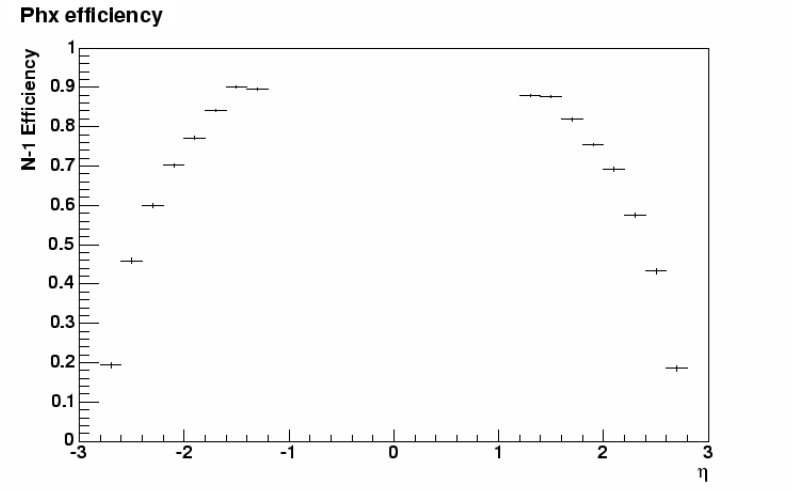

Figure A.2: Phoenix plug tracking efficiency as a function of η, where $1.2 < |\eta| < 2.8$

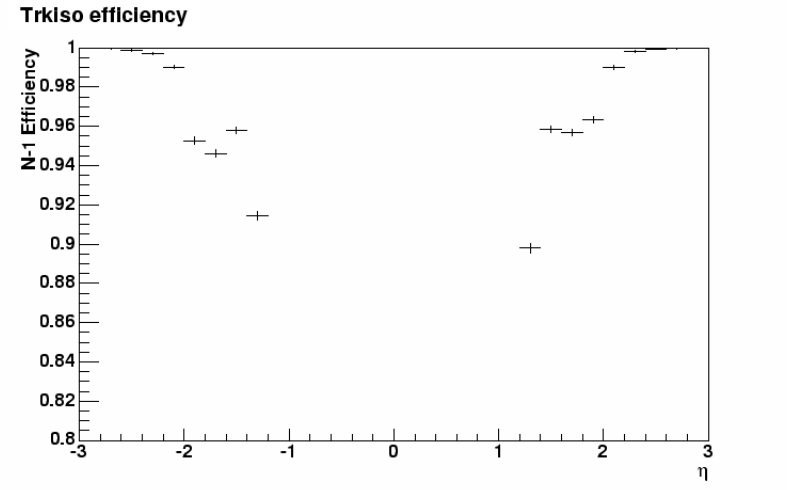

Figure A.3: Standalone plug tracking efficiency as a function of η, where $1.2 < |\eta| < 2.8$

Appendix B

Efficiency Calculation for Central-Central Lepton Events

To calculate the efficiency of central events, using leptons from Z boson decays, one electron is required to pass all ID selection cuts (the 'tight' leg), while the second has basic ID requirements imposed only (the 'probe' leg). The tight cuts may then be applied sequentially to the probe leg to calculate the efficiencies (ϵ_T). The number of events passing the different selection requirements are defined as follows [64]:

- Number of events with both electrons passing tight cuts: N_{TT}.
- Number of events with one electron passing tight cuts and one passing loose cuts but failing tight cuts: N_{TL}.
- Number of events with both electrons passing only loose cuts: N_{LL}.

The total number of events is the given by:

$$N = N_{TT} + N_{TL} + N_{LL} \tag{B.1}$$

allowing the above terms to be expressed as:

$$N_{TT} = \epsilon_T^2 \times N \tag{B.2}$$

$$N_{TL} = 2 \times \epsilon_T \times (1 - \epsilon_T) \times N \tag{B.3}$$

$$N_{LL} = (1 - \epsilon_T)^2 \times N \tag{B.4}$$

If only one lepton passes tight cuts, the other leg is assigned as the probe leg. If both legs pass tight cuts, one of the leptons is randomly assigned to be the tight leg and the other to be the probe. This removes a factor of 2 in N_{TL}, as one lepton must pass the tight cuts. Then:

$$\epsilon_{probe} = \frac{N_{TT}}{N_{TT} + N_{TL}/2} = \frac{2N_{TT}}{2N_{TT} + N_{TL}} = \frac{\epsilon_T}{\epsilon_T + (1 - \epsilon_T)} = \epsilon_T \tag{B.5}$$

and

$$\epsilon_i = \frac{N_{Ti} + N_{TT}}{2N_{TT} + N_{TL}} \tag{B.6}$$

The uncertainties are evaluated through a re-expression of the three terms given in Equations B.3 to B.4. Additionally, the variable N_{TC} is used, which is defined as $N_{TC} = N_{TL} + N_{TT}$, it is the number of events where at least one electron passes the tight cuts and the other one can pass either the loose or tight cuts, giving: $x_1 = N_{TL} - N_{TT}$, $x_2 = N_{TT}$ and $x_3 = N_{TC} - N_{TL}$. These are then computed through the expression:

$$\delta(\epsilon) = \sqrt{\sum_{j=1}^{3} \left(\frac{\partial \epsilon}{\partial x_j} \delta(x_j) \right)^2} \tag{B.7}$$

Appendix C

Combined Diphoton and Dielectron Limits on Randall-Sundrum Graviton Production

The likelihood function, used to calculate the diphoton limits, is also used to combine the diphoton and dielectron [65] analyses, to obtain the current most exclusive limits on the Randall-Sundrum model [66]. As each channel (central-central, central-plug) is calculated separately, there is no difference between combining the central-central e^+e^- with the central-plug e^+e^- and combining the central-central e^+e^- with the central-plug $\gamma\gamma$, once the different luminosities and branching ratios are taken into account. This is made possible by the tracking requirements used in these analyses; the dielectron analysis requires that each central leg has an associated track while the diphoton analysis requires no associated track. This ensures there are no overlapping events. As described in Section 1.2.3, the branching ratio to photons is twice that to electrons. The luminosities are 820 pb^{-1} for the dielectron and 1070-1155 pb^{-1}

for the diphoton.

Figure C.1 shows the $k/\overline{M}_{Pl}$ model lines, overlayed with the dielectron, diphoton and combined limits with full systematic errors included. From this, the 95% CL exclusion domain in the plane of $k/\overline{M}_{Pl}$ versus graviton mass, shown in Figure C.2, is obtained.

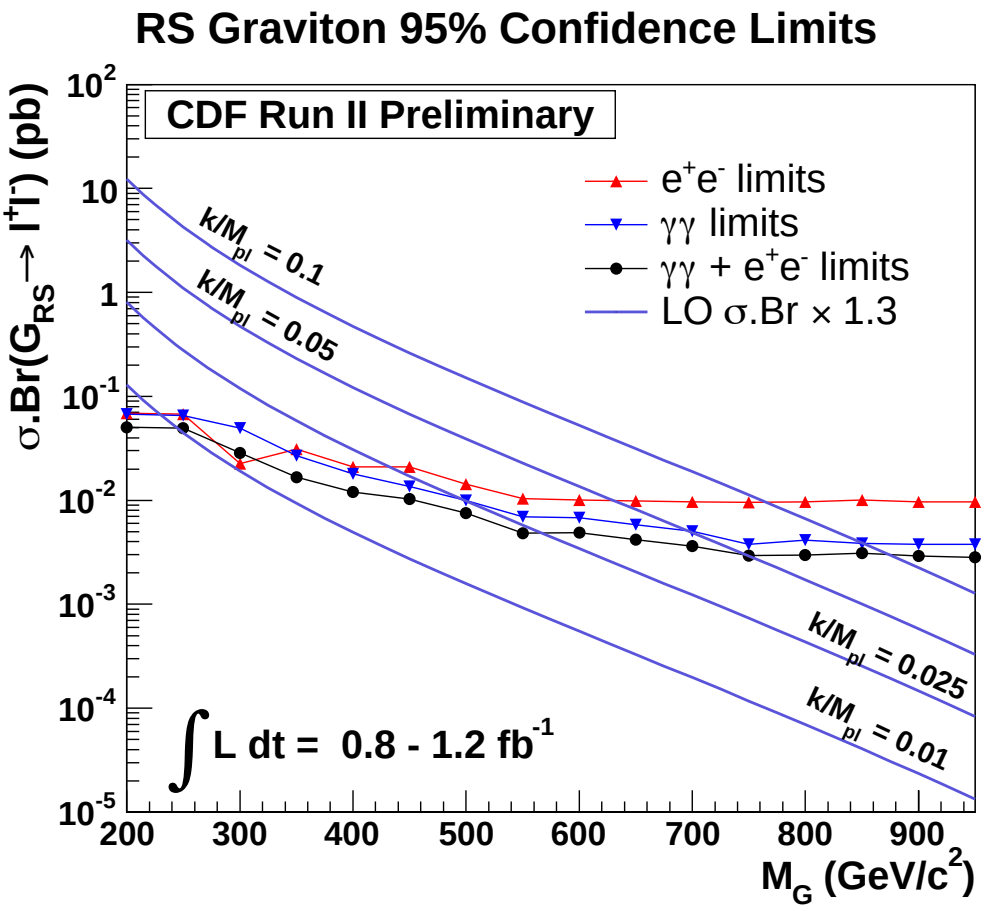

Figure C.1: The 95% C.L. limits on RS graviton production for the dielectron, diphoton and combined limits, with the $k/\overline{M}_{Pl}$ model lines overlayed.

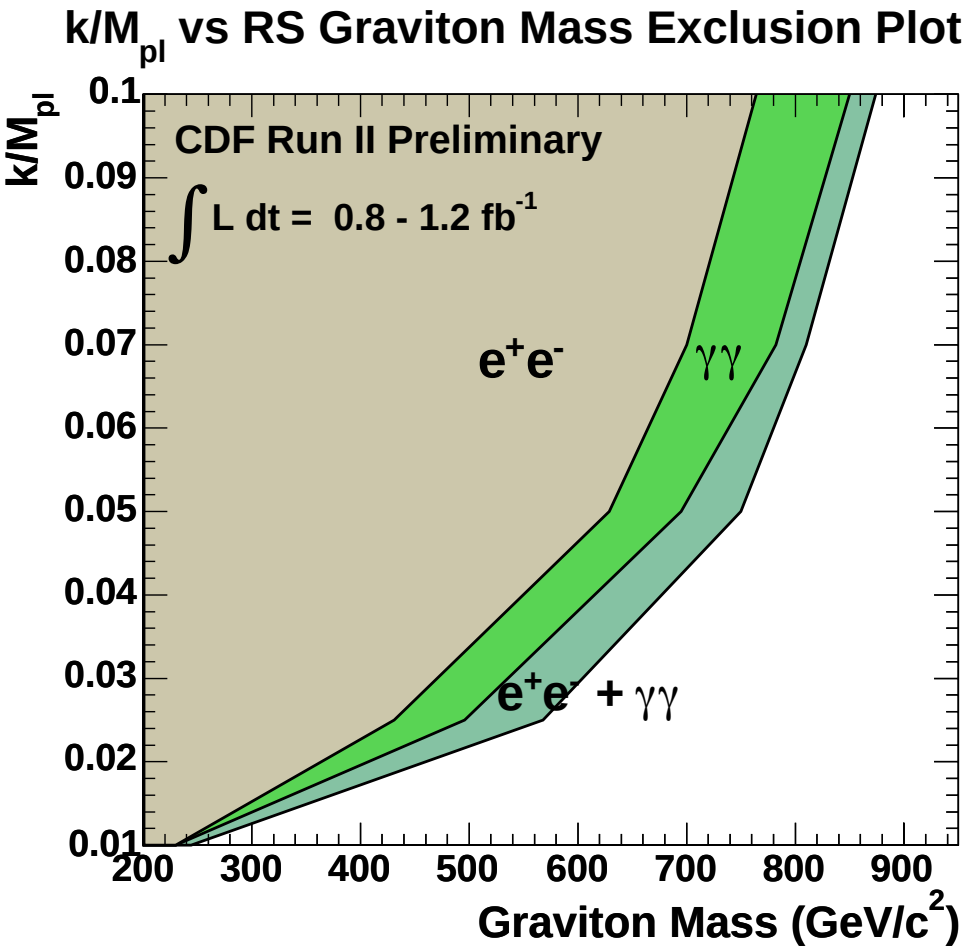

Figure C.2: 95% CL exclusion domain in the plane of $k/\overline{M}_{Pl}$ versus graviton mass, for the combined dielectron and diphoton channels.

References

[1] S. Eidelman et al., Physics Letters **B592**, 1 (2004)

[2] W.-M. Yao et al., *The Review of Particle Physics*, J. Phys. **G 33**, 1 (2006)

[3] S. Carroll, *Spacetime and Geometry: An Introduction to General Relativity*, Addison-Wesley (2003)

[4] G. Gabrielse, D. Hanneke, T. Kinoshita, M. Nio and B. Odom, *New Determination of the Fine Structure Constant from the Electron g Value and QED*, Phys. Rev. Lett. **97** (2006)

[5] S.L. Glashow, *Partial Symmetries of Weak Interactions*, Nucl. Phys. **22**, 579 (1961)

[6] P.W. Higgs, *Broken Symmetries and the Masses of Gauge Bosons*, Phys. Lett. **13** (1964) 508-509

[7] K. Grotz and H.V. Klapdor, *The Weak Interaction in Nuclear, Particle and Astrophysics*, Adam Hilger, Bristol (1990)

[8] Y.Fukuda et al., *Evidence for Oscillation of Atmospheric Neutrinos*, Phys. Rev. Lett. **81** (1998) 1562-1567

[9] B. Kayser, *Neutrino Mass: Where Do We Stand, and Where Are We Going?*, arXiv:hep-ph/9810513 (1998)

[10] J. Pumplin et al., *New Generation of Parton Distributions with Uncertainties from Global QCD Analysis*, JHEP **0207**, 012 (2002), arXiv:hep-ph/0201195

[11] H. Georgi and S.L. Glashow, *Unity of All Elementary-Particle Forces*, Phys. Rev. Lett. **32** (1974) 438-441

[12] L. Randall, *Warped Passages: Unravelling the Mysteries of the Universe's Hidden Dimensions*, Ecco (2005)

[13] A. Taffard, *Search for the Tau Slepton at Delphi and Muon Identification and Z Production at CDF*, Thesis (2002)

[14] J. Weiss and B. Zumino, *Supergauge Invariant Extension of Quantum Electrodynamics*, Nucl. Phys. B, **78** (1974) 1-13

[15] S. Charanjit et al., *The Minimal Supersymmetric Grand Unified Theory*, Phys.Lett. B , **588** (2004) 196-202

[16] F. Sannino, *Dynamical Breaking of the Electroweak Theory*, arXiv:hep-ph/0606128 (2006)

[17] W.A. Bardeen, C.T. Hill and M. Lindner, *Minimal Dynamical Symmetry Breaking of the Standard Model*, Phys. Rev. D, **41**, (1990) 1647 - 1660

[18] N. Arkani-Hamed, S. Dimopoulos and G. Dvali, *The Hierarchy Problem and New Dimensions at a Millimeter*, Phys. Lett. B, **429** (1998) 263

[19] P. Beauchemin on behalf of the CDF Collaboration, *Search for large Extra Dimensions in CDF*, SUSY 06, June 12–17 (2006)

[20] L. Randall and R. Sundrum, *Large Mass Hierarchy from a Small Extra Dimension*, Phys. Rev. Lett., **83**, (1999) 3370 - 3373

[21] Th. Kaluza, Sitzungsber, Preuss. Akad. Wiss. Berlin (Math.Phys) (1921) 966. 9, O. Klein, Z. Phys. **37** (1926) 895

[22] B.C. Allanach et al., *Exploring Small Extra Dimensions at the Large Hadron Collider*, arXiv:hep-ph/0211205 (2002)

[23] H. Davoudiasl, J.L. Hewett and T.G. Rizzo, *Phenomenology of the Randall-Sundrum Gauge Hierarchy Model*, Phys. Rev. Lett., **84**, (2000) 2080

[24] H. Davoudiasl, J.L. Hewett and T.G. Rizzo, *Experimental Probes of Localized Gravity: On and Off the Wall* arXiv:hep-ph/0006041 (2000)

[25] R. Culbertson and T. Pratt, *Search for Randall-Sundrum Gravitons in High Mass Diphotons*, CdfNote 6560 (2003)

[26] V. M. Abazov et al., *Search for Randall-Sundrum Gravitons in Dilepton and Diphoton Final States*, Phys. Rev. Lett., **95**, (2005)

[27] H. Gerberich, *Searches for BSM (non-SUSY) physics at the Tevatron*, arXiv:hep-ex/0511011 (2005)

[28] Fermilab's Chain of Accelerators, Accelerator Details: the Proton Source, **http://www-bd.fnal.gov/public/proton.html**

[29] Fermilab Main Injector Technical Design handbook, **http://www-fmi.fnal/fmiinternal/MI_Technical_Design/index.html**

[30] Fermilab's Chain of Accelerators, Accelerator Details: the Antiproton Source, **http://www-ad.fnal.gov/public/antiproton.html**

[31] CDF Collaboration *CDF II Detector Technical Design Report*, FERMILAB-PUB-96/390-E

[32] L. Miller, *Status of the CDF Silicon Detector*, Nucl. Inst. Meth. A **518** (2004) 281-285

[33] T.K. Nelson, *The CDF-II Silicon Tracking System*, Nucl. Inst. Meth. A **485** (2002) 1-5

[34] T. Affolder et al., *CDF Central Outer Tracker*, Nucl. Inst. Meth. A **526** (2001) 249-299

[35] C. Paus et al. *Design and Performance Tests of the CDF Time-of-Flight System*, Nucl. Inst. Meth. A **461** (2001) 579-581

[36] L. Balka et al. *The CDF Central Electromagnetic Calorimeter*, Nucl. Inst. Meth. A **267** (1988) 272-279

[37] S. Bertolucci et al. *The CDF Central and Endwall Hadron Calorimeter*, Nucl. Inst. Meth. A **267** (1988) 301-314

[38] A. Alborw et al. *The CDF Plug Upgrade Electromagnetic Calorimeter: Test Beam Results*, Nucl. Inst. Meth. A **480** (2002) 524-546

[39] A. Solodsky, CDF Collaboration, *The Shower-Maximum Detector for CDF II*, FERMILAB-CONF-98/085-E (1990)

[40] CDF Run II Muon Chambers, **http://www-cdfonline.fnal.gov/cdf_muon/chambers.html**

[41] T. Dorigo, *The Muon System Upgrade for the CDF II Experiment*, Nucl. Inst. Meth. A **461** (2001) 560-562

[42] D. Acosta et al. *The CDF Cherenkov Luminosity Monitor*, Nucl. Inst. Meth. A **461** (2001) 540-544

[43] S. Klimenko et al. *Averaging of the Inelastic Cross-Sections Measured by the CDF and the E811 Experiments*, FERMILAB-FN-0741 (2003)

[44] GEANT 3 *Detector Description and Simulation Tool*, CERN Program Library Long Writeup **W5013** (1993)

[45] The Trigger and Datasets Working Group, *The CDF Run II Trigger Table and Datasets Plan*, CdfNote 4718 (1998)

[46] R. Wagner, *Electron Identification for Run II: Algorithms*, CdfNote 5456 (2003)

[47] C. Hays, P. Tamburello, A. Kotwal, P. Wittich and R. Snider, *The COT Pattern Recognition Algorithm and Offline Code*, CdfNote 6992 (2004)

[48] T. Nelson, *Silicon Tracking for Plug Electrons*, CdfNote 5970 (2002)

[49] T. Nelson, *Forward Electron Tracking with PhoenixMods Package*, CdfNote 6278 (2003)

[50] K. Yasuoka et al., *Response Maps of the CDF Central Electromagnetic Calorimeter with Electrons*, Nucl. Inst. Meth. A **267** (1988) 315-329

[51] W.K. Sakumoto, H.S. Budd, *Run II PEM Tower Transverse Response Maps*, CdfNote 6181 (2003)

[52] A. Robson, G. Manca, P. Renton, G. Veramendi, Y-K. Kim, *A Measurement of* $\sigma \times BR(Z \rightarrow ee)$ *using Run II Central and Plug Electrons in* 72 pb^{-1}, CdfNote 6642 (2004)

[53] M.Kirby, *Measurement of* $W + \gamma$ *Production in Proton-Antiproton Collisions at* $\sqrt{s} = 1.96\ TeV$, Thesis (2004)

[54] P. Wilson, *Calorimeter Isolation and Lateral Shower Leakage for Electrons and Photons*, CdfNote 4170 (1997)

[55] C. Issever, C. Mills, A. Robson and B. Wagner, *Plug Electron Baseline Cuts Defined in Summer 2003 and Cut Efficiencies*, CdfNote 6789 (2004)

[56] S. Harper, J. Goldstein and P. Renton, *The Search for New Physics in Di-Electron Events*, CdfNote 7784 (2005)

[57] M. Goncharov, V. Krutelyov, D. Toback, P. Wagner, R. Culbertson and A. Pronko, *Discrimination of Beam Halo and Cosmic Rays as a Source of Photon Candidates*, CdfNote 8409 (2006)

[58] W. Sakumoto, *Event $|Zvtx| < 60$ Cut Acceptance for Run II (to Feb 06)*, CdfNote 8318 (2006)

[59] T. Binoth, J.P. Guillet, E. Pilon and M. Werlen, *A Full Next to Leading Order Study of Direct Photon Pair Production in Hadronic Collisions*, arXiv:hep-ph/9911340 v3 (2000)

[60] R. Culbertson, A. Pronko, S-S E. Yu, *The Probability of an Electron Faking an Isolated Prompt Photon in the CEM*, CdfNote 8220 (2006)

[61] R. Culbertson, T. Pratt, *Search for Randall Sundrum Gravitons in 202 pb^{-1} of Run II High Mass Diphoton Data*, CdfNote 7024 (2004)

[62] T. Bayes, *An Essay Towards Solving a Problem in the Doctrine of Chances* (1763)

[63] P. Mathews, V. Ravindran, K.Sridhar and W.L. van Neerven, *Next-to-Leading Order QCD Corrections to the Drell-Yan Cross Section in Models of TeV-Scale Gravity*, arXiv:hep-ph/0411018 v2 (2004)

[64] B. Heinemann and G. Manca, *How to Calculate Lepton Efficiencies from Jpsi, Upsilon and Z Samples*

[65] J. Goldstein, S. Harper and P. Renton, *The Search for New Physics in Di-Electron Events in 820 pb^{-1} of Run II Data*, CdfNote 8062 (2006)

[66] T. Berry, R. Culbertson, J. Goldstein, S. Harper, P. Renton and S-M Wynne, *The Combination of Di-Photon and Di-Electron Limits on Randall-Sundrum Graviton Production*, CdfNote 8385 (2007)